SURFACE TEXTURING STUDY WITH ALUMINUM INDUCED TEXTURING
METHOD ON SODA-LIME GLASS SUBSTRATES FOR THIN FILM SOLAR
CELLS

A THESIS SUBMITTED TO
THE GRADUATE SCHOOL OF NATURAL AND APPLIED SCIENCES
OF
MIDDLE EAST TECHNICAL UNIVERSITY

BY

MUSTAFA ÜNAL

IN PARTIAL FULFILLMENT OF THE REQUIREMENTS
FOR
THE DEGREE OF MASTER OF SCIENCE
IN
MICRO AND NANOTECHNOLOGY DEPARTMENT

JULY 2017

Approval of the Thesis:

SURFACE TEXTURING STUDY WITH ALUMINUM INDUCED TEXTURING METHOD ON SODA-LIME GLASS SUBSTRATES FOR THIN FILM SOLAR CELLS

Submitted by **MUSTAFA ÜNAL** in partial fulfillment of the requirements for the degree of **Master of Science in Micro and Nanotechnology Department, Middle East Technical University** by,

Prof. Dr. Gülbin Dural Ünver
Dean, Graduate School of **Natural and Applied Sciences**   _____

Assoc. Prof. Dr. Burcu Akata Kurç
Head of Department, **Micro and Nanotechnology**   _____

Prof. Dr. Raşit Turan
Supervisor, **Physics Dept., METU**   _____

Assoc. Prof. Dr. Emrah Ünalan
Co-Supervisor, **Metallurgical and Materials Engineering Dept., METU** _____

Examining Committee Members:

Prof. Dr. Mehmet Parlak
Physics Dept., METU   _____

Prof. Dr. Raşit Turan
Physics Dept., METU   _____

Prof. Dr. Macit Özenbaş
Metallurgical and Materials Engineering Dept., METU   _____

Prof. Dr. Hüseyin Sarı
Physics Engineering Dept., Ankara University   _____

Assoc. Prof. Dr. Alpan Bek
Physics Dept., METU   _____

Date: *20.07.2017*

I hereby declare that all information in this document has been obtained and presented in accordance with academic rules and ethical conduct. I also declare that, as required by these rules and conduct, I have fully cited and referenced all material and results that are not original to this work.

Name, Last Name: Mustafa Ünal

Signature   :

ABSTRACT

SURFACE TEXTURING STUDY WITH ALUMINUM INDUCED TEXTURING METHOD ON SODA-LIME GLASS SUBSTRATES FOR THIN FILM SOLAR CELLS

ÜNAL, Mustafa

MS, Micro and Nanotechnology Department

Supervisor: Prof. Dr. Raşit Turan

Co-Supervisor: Assoc. Prof. Dr. Emrah Ünalan

July 2017, 164 pages

It is essential to employ an effective light trapping scheme to decrease the cost of produced solar electricity further in thin film solar cell technologies. There are several methods that can be used for light trapping and aluminum induced texturing (AIT) is one of them. The aim of this thesis study is to obtain highly effective light trapping interface via texturing of glass surface by AIT process. The resultant texture is affected by several parameters such as Al thickness, annealing time and temperature, etching conditions like etchant type, duration etc. In order to obtain high scattering interfaces, different parameters were optimized and studies focusing on understanding of the texturing mechanism has been conducted. In this thesis, it is observed that 50% of the transmitted light can be scattered through textured surface that formed by conventional AIT process. The scattering value can be increased nearly 80% for 400 nm wavelength with newly developed solution that is based on NaOH. In addition, an attempt has been made to model the reaction mechanism during the optimization of the annealing process. The composition of the glass predominantly affecting the resultant texture is also observed. Additionally, results indicate that combination of

AIT textures with macro surface structures can result with enhancement in the scattering of transmitted light by nearly 90% for 400 nm wavelength. Following the optimization studies of AIT, the effect of the texturing on the performance of thin film solar cells has been tested by deposition for a-Si:H thin films and a-Si:H solar cells.

Key Words: *Aluminum Induced Texturing, Light Trapping, Thin Film Solar Cells, Annealing Optimization, HF-free Processing*

ÖZ

İNCE FİLM GÜNEŞ GÖZELERİ İÇİN SODA-KİREÇ CAM ALTLIKLARIN ALÜMİNYUM İLE YÜZEYİNİN DESENLEMESİ

ÜNAL, Mustafa

Yüksek Lisans, Mikro ve Nanoteknoloji Bölümü

Tez Yöneticisi: Prof. Dr. Raşit Turan

Ortak Tez Yöneticisi: Assoc. Prof. Dr. Emrah Ünalan

Temmuz 2017, 164 sayfa

İnce film güneş gözesi teknolojileri ile üretilen elektriğin maliyetinin azaltılması için etkili bir ışık hapsetme senaryosunun uygulanması önemlidir. Işık hapsetme için kullanılabilecek birçok yöntem bulunmaktadır ve alüminyum ile desenleme (AIT) yöntemi bunlardan biridir. Bu tez çalışmasının amacı cam yüzeyinin AIT işlemi ile desenlemesiyle oldukça etkili ışığı hapsedici ara yüzey elde edilmesidir. Oluşan desen Al kalınlığı, tavlama sıcaklığı ve süresi, aşındırıcılar, süre gibi aşındırma koşullarına bağlı olarak değişmektedir. Işığı yüksek oranda saçıcı ara yüzeylerin elde edilmesi için birçok farklı parametre optimize edilmiştir ve desenleme mekanizmasının anlaşılması için çalışmalar yapılmıştır. Bu tez çalışmasında, 400 nm dalga boyuna sahip ışıkta, camdan geçen ışığın %50'sinin bilinen AIT yöntemi ile desenlemiş yüzeyden saçtırılabildiği gözlemlenmiştir. Bu değer, NaOH içeren yeni solüsyon ile yapılan AIT işlemiyle %80'e yaklaşmıştır. Ayrıca tavlama sürecinin modellemesi ile ilgili çalışmalar yürütülmüştür. Bunula birlikte, camın içeriğinin oluşan deseni büyük oranda etkilediği de gözlemlenmiştir. İlaveten, AIT ile oluşturulan desenlerin makro boyutlu yüzey yapıları ile birleştirilmesi ile 400 nm dalga boyunda camdan geçen ışığın yaklaşın %90'ının saçtırılabilmiştir. AIT metodunun

optimizasyonuna ek olarak, desenin ince film güneş gözelerinin performansı üzerine etkisi, a-Si:H ince film ve a-Si:H güneş gözesi üretimi ile test edilmiştir.

Anahtar Kelimeler: *Alüminyum ile Desenleme, Işık Yönetimi, İnce Film Güneş Hücreleri, Tavlama Optimizasyonu, HF'siz İşlem*

To my family and my dearest wife, Hande Ünal…

x

ACKNOWLEDGEMENTS

TABLE OF CONTENTS

LIST OF TABLES

LIST OF FIGURES

FIGURES

xxx

CHAPTER I

INTRODUCTION

The use of alternative energy sources becomes crucial due to increasing energy demand in the world and dependence on limited energy sources like oil and coal, which are also harmful to the environment. Solar energy becomes more and more popular over the years among other renewable energy sources like wind, biofuel, wave, geothermal, etc. due to the availability of energy source in any part of the world with almost infinite amount. Solar energy owes its popularity to the possibility of applications on roofs, farms and as big power plants along with the increase in efficiencies and decrease in the price of solar electricity. With 75 GW annual installation, which is 48% notable growth rate in 2016, and nearly 300 GW total installed capacity, photovoltaics has started to turn into a traditional source of energy [1], [2]. Today, c-Si wafer based solar cells are leading the market with efficiencies reaching to 25.3% for non-concentrated incident light [3]. In addition, thin film based solar energy technologies like a-Si:H, CdTe, CIGS, etc. following crystalline Si with only 8% market share [4].

Thin film solar cells offer easy production methods with lesser material usage, which naturally causes the decrease in the cost of produced solar electricity. However, due to having low efficiencies like maximum 14.0% for a-Si:H [5] or usage of toxic or rare materials like Cd, Te, Ge, etc., the market share of thin film stays lower even though this technology has become cost-competitive against Si wafer based technologies [6].

Further decrease in the cost of produced solar electricity or increase in the efficiency of thin film solar modules could be achieved by a successful light management scheme. By increasing the optical path length inside the thin absorber layer, the absorption can be enhanced and the efficiency could be increased or the thickness can be decreased so that the material usage also decreases, especially for the case of CdTe and CIGS. Adding textured, rough interfaces to the device leads to scattering of the light by this interface. Scattered light travels inside the absorber layer with a longer path, which increases the absorption probability. As a result, absorber layer can be made thinner without any decrease in the efficiency or the efficiency can even be boosted up.

1.1.   History of PV Technology

Series observation of photon induced electrical current in 19th century [7], explanation of photoelectric effect by A. Einstein in 1905 [8] and the discovery of single crystalline Si production method by Jan Czochralski in 1918 [9] has formed the foundation of the PV technology. The first p-n junction solar cell was described by Russel Ohl from Bell Laboratories, which was based on slowly solidified silicon melt on crystalline silicon substrate [10]. Then, Chapin, Fuller and Pearson of Bell Laboratories reported 6% efficiency for p-n junction solar cell in 1954. Within the next 20 years, solar cells have met the energy demand of space missions [11].

1980's was the era of commercialization of solar cell technology. Studies were made to decrease the production cost and to increase the efficiency, which resulted with efficiencies over 20% for non-concentrator silicon solar cells [12]. Due to the rising interest on photovoltaics, and the awareness about the pollution effect of fossil fuels, in the late 1990's, the PV production increased about 20%, resulting in a reduction in the production costs. Different solar cell technologies were studied in that time, such as gallium arsenide (GaAs), cadmium telluride (CdTe), dye sensitized and organic solar cells as an alternative to Si wafer based solar cells. The progress of the photovoltaic technology can be seen in the Figure 1.

Today, annually 75 GW was installed worldwide in 2016, in which only China made 34 GW installation, and total installed capacity reached to 300 GW. Following China, top five contributors are USA with 13 GW installation, Japan with 8.6 GW, Europe with 6.5 GW and India with 5 GW [1]. The annual installed capacity share of Turkey in the 75 GW is only 571 MW as reported by Turkey Energy Institute. By this addition, the cumulative installation of Turkey has passed 800 MW and the total share of solar energy in the energy production has become 1% [13], [14].

Si wafer based solar panels produce 93% of total solar electricity [4]. This is because of the maturity of the Si technology as a semiconductor material [15]. In addition, different approaches can be used to produce solar electricity.
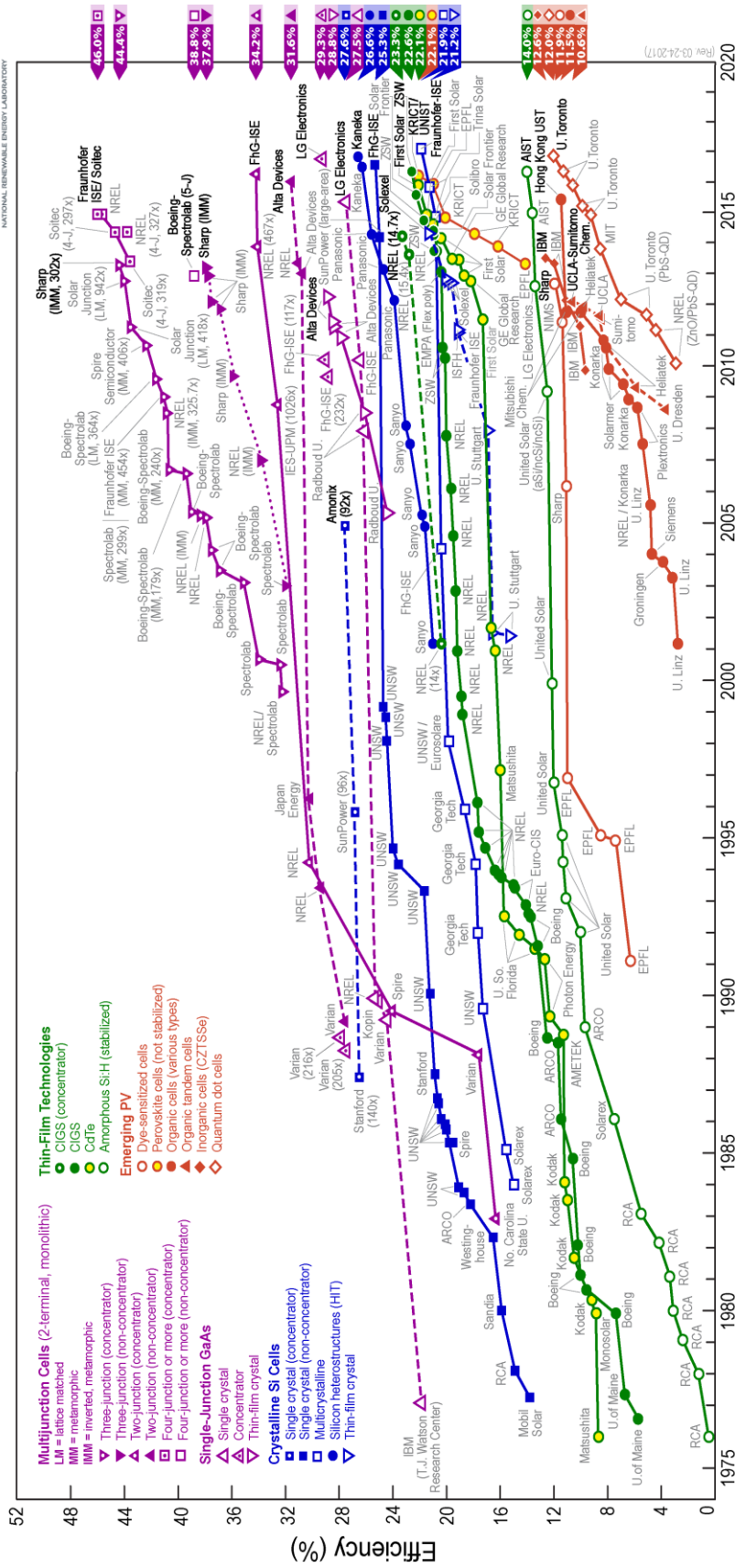
Figure 1. The efficiency development for different solar cell technologies [36]

1.2. Basics of PV Technology

1.2.1. Solar Irradiation

Sun is a major energy source sustaining the life on the earth. The emission spectra of sun, i.e. solar radiation spectrum has maximum intensity in the visible region. At the sea level, some of this intensity is lost due to the absorption by particles and molecules in the atmosphere like O_2, CO_2, H_2O etc., which results in a spectrum given in the Figure 2(a).
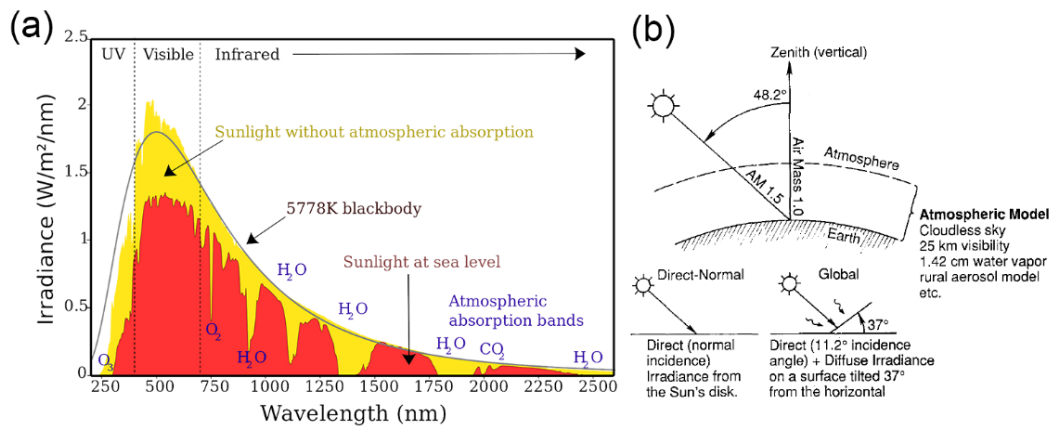
Figure 2. (a) Solar irradiance spectrum on Earth and [16] **and (b) Schematic representation of AM 1.0 and AM1.5 with direct and global radiation** [17]**.**

Different locations on the earth causes a change in the optical path of the sunlight. The change in the optical path length alters the solar spectrum because the interaction of light with air will not be the same. As a result, solar cell efficiencies will differ for various locations, which makes efficiency measurements unrealistic. To overcome this difficulty, air mass (AM) concept is used as described and shown in Figure 2(b). For space applications, for example, "AM 0" is used, in which there is no atmospheric interaction. However, "AM 1" and "AM 1.5" defines solar spectrum on the surface of the earth for sun position in the vertical direction and with and angle

48.2°, which is also called as "zenith angle" [17]. In addition, sunlight coming to the surface has two component: direct radiation and diffuse radiation. Diffuse radiation is formed due to scattering of the light by particles in the atmosphere and it should be considered during the measurements to obtain realistic test conditions. For this reason, direct and global radiation should be specified. For example, AM 1.5D refers only direct radiation while AM 1.5G refers global radiation which is formed by diffuse and direct component of the sun radiation.

Standard test conditions for solar cells and modules are defined as irradiance intensity 1 KW/m^2 with standard AM 1.5 spectrum and 25 °C cell or module temperature [18].

1.2.2. Light – Matter Interaction

Semiconductors have the ability to absorb the light and convert it into electrical energy due to the existing forbidden energy regions, which are called as band-gap (Eg). Insulators also have forbidden energy regions but it is too large to absorb visible and infrared region while metals have no forbidden energy states where electrons are floating free. The electron energy diagram of metals, semiconductors and insulators are illustrated in Figure 3.
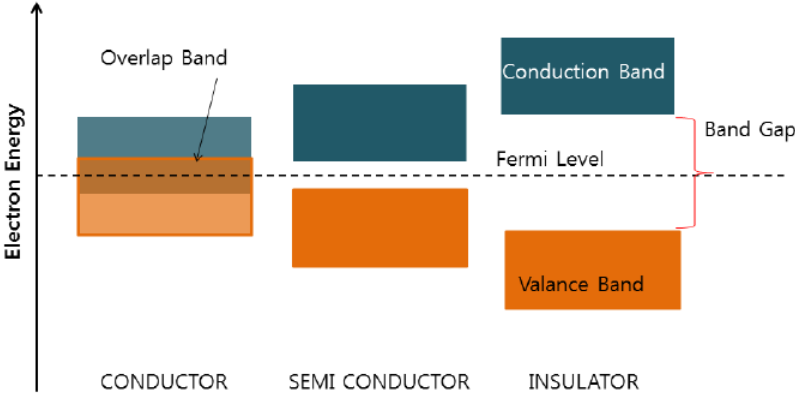
Figure 3. Electron energy states in conductors, semiconductors and insulators [19]**.**

In semiconductors, states filled by electrons at absolute zero are called as valance band while empty states are called as conduction band due to the fact that conduction happens in semiconductors due to the existing electron in conduction band. When light interact with a semiconductor, if it has an energy equal or greater than the band gap of the semiconductor, an electron from valance band is exited to the conduction band. There is an empty state in the valance band, which is called as hole. By the proper device structure, this electron and hole pair can be extracted from the semiconductor and current can be obtained [20].

The electrical properties of semiconductors can be manipulated by adding foreign atoms to the material. In the Si case, addition of boron to the crystal system makes Si p-type where some of the energy states in the valance band are empty. On the other hand, phosphorus addition increases the number of electrons in the conduction band and makes Si n-type. This change in electronic structure make harvesting energy from semiconductors possible by forming a junction with p-type and n-type semiconductors [20].

In Figure 4, electronic properties of the p-n junction are given. By the formation of p-n junction, holes and electron cancel each other at the interface, negative and positive ions that lost their electrons and holes during recombination are exposed. The region where electron and holes cancels each other is called as depletion region and these exposed ions form an internal electric field [20].

When a photon falls onto the junction, if it has an enough energy, which is equal or more than the band-gap of the semiconductor, an electron-hole pair is created. By the build-in electric field, electron is drifted to the n-type region while hole is drifted to the p-type region. In addition, electron-hole pairs are created near to the depletion region can be separated by diffusion. The distance where electron-hole pairs can be separated by diffusion is called as diffusion length [20].
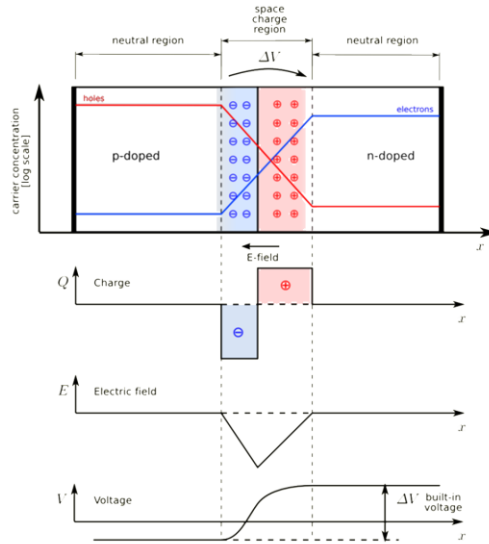
Figure 4. Charge distribution, electric field strength and built-in voltage across the p-n junction [21]**.**

If the energy of the photon is higher than the band-gap, the excess energy is converted into phonon by relaxation to the band edges. In addition, some of the excited electrons could recombine with holes or be trapped in defects of the material, creating material specific conversion efficiency limits as given in Figure 5.
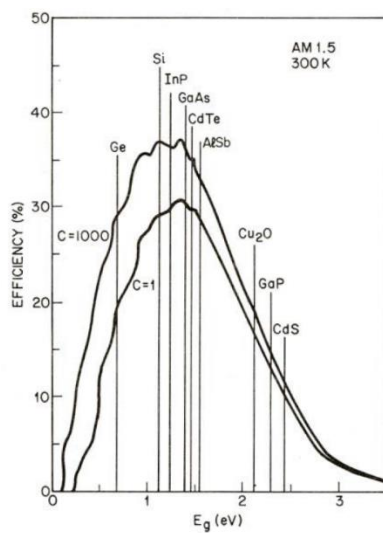
Figure 5. Shockley–Queisser limit of solar spectrum for 1 sun and 1000 sun illumination alongside with band-gap of semiconductors [22]**.**

1.2.3. Solar Cell Parameters

A solar cell is basically a diode, which reacts with the illumination. The electronic structure of solar cell is given Figure 6(a). Therefore, for characterization, I-V measurement is done. Without an illumination, there is *reverse saturation current*, which appears due to thermal excitation of electrons on the structure. The current on dark condition is described by the equation given below.

$$I = I_0(e^{\frac{qV}{kT}} - 1) \qquad \text{(Eq. 1)}^{[23]}$$

where I is the net current, I_0 is reverse saturation current, q is the charge of the electron, V is the bias voltage, T is the temperature of the cell in K and k is the Boltzman constant.

I-V curve of the solar cell without illumination is given in Figure 6(b). After the illumination, reverse current is formed and I-V curve shifts to the negative side of the current axis [Figure 6(b)] and the current can be expressed as in Eq. 2 where I_L is *light induced current*.

$$I = I_0\left(e^{\frac{qV}{kT}} - 1\right) - I_L \qquad \text{(Eq. 2)}^{[23]}$$
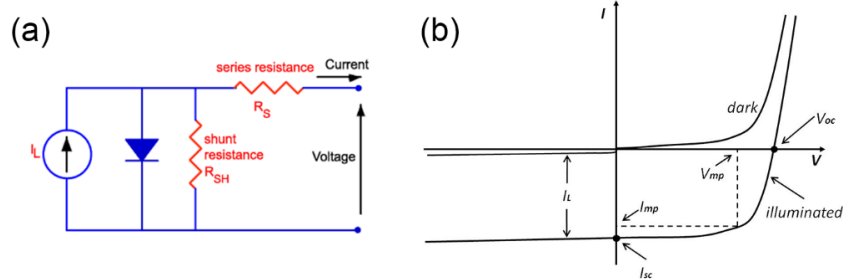
Figure 6. (a) Electronic configuration and (b) I-V curve of a solar cell [24]**.**

For the characterization of a solar cell, 4th quadrant of I-V curve is used and for simplicity, it is folded into 1st quadrant.

Due to several loss mechanisms such as reflection, recombination and thermalization, not all of the given energy can be converted into electrical energy as mentioned before. To calculate the conversion efficiency, the power generated is divided by the power falls onto the solar cell. The power of given light is known thanks to the standard test conditions. The output power, however, can be obtained from I-V curve of the cell. Current and corresponding voltage value gives the power. By multiplication of each value, maximum power can be found. Then, *the efficiency* (η) can be calculated by Eq. 3.

$$Cell\ Efficiency\ (\eta) = \frac{P_{out}}{P_{in}} = \frac{P_{mpp}}{P_{light}} = \frac{V_{mpp} \times I_{mpp}}{P_{light}} \qquad \text{(Eq. 3)}^{[25]}$$

where P_{in} is the power given to the cell, P_{out} is the power taken from the cell, P_{mpp} is the maximum power point can be obtained from the cell, P_{light} is the power of the given light, V_{mpp} is the voltage at maximum power point and I_{mpp} is the current obtained at maximum power point.

Under illumination, the population of charges are increased on each side of p-n junction if the device is not shorted. This situation results with a potential difference, which is called *open circuit voltage (V_{oc})*. V_{oc} can be extracted from the I-V curve of the device. It is the voltage where I-V curve cuts the voltage axis as given in Figure 6(b). V_{oc} can be expressed and calculated by the equation:

$$V_{oc} = \frac{kT}{q} ln\left(\frac{I_L}{I_0} + 1\right) \qquad \text{(Eq. 4)}^{[25]}$$

The current measured when the device is shorted is called as *short circuit current (I_{sc})*. I_{sc} can be found from I-V curve, from where this curve cuts through current axis as shown in Figure 6(b).

The I-V curve gives important electronic information about the cell. One of these is the Fill Factor (FF). FF is the measure of the "squarenes" of I-V curve, which gives the ratio of maximum obtainable power and maximum power in the case of perfect square. FF can be calculated by given formula below.

$$FF = \frac{V_{mpp} \times I_{mpp}}{V_{oc} \times I_{sc}} \qquad \text{(Eq. 5)}^{[26]}$$

by extracting V_{mpp} x I_{mpp} from Eq. 5, the efficiency equation given in Eq. 3 can be rewritten as:

$$\eta = \frac{FF \times V_{oc} \times I_{sc}}{P_{light}} \qquad \text{(Eq. 6)}^{[26]}$$

Maximum efficiency can be obtained by decreasing the series resistance (R_s) that is the resistivity between metal-semiconductor contacts and increasing the shunt resistance (R_{sh}) that is the resistivity between p and n type regions so that the diffusion of charge carrier is limited. Shunt and series resistance can be found in I-V curve by taking the first derivative. At $V=V_{oc}$, series resistance and at $V=0$, shunt resistance is obtained. Relative equations to obtain these resistances are given in Eq. 7 and Eq. 8 correspondingly.

$$Series\ Resistance\ (R_s) = \left(\frac{1}{\frac{dI}{dV}} \right) \Bigg|_{V=V_{oc}} \qquad \text{(Eq. 7)}^{[27]}$$

$$Shunt\ Resistance\ (R_{sh}) = \left(\frac{1}{\frac{dI}{dV}} \right) \Bigg|_{V=0} \qquad \text{(Eq. 8)}^{[27]}$$

The efficiency of a solar cell can also be found without I-V measurement. Quantum efficiency (Q.E.) defines the number of electrons produced by a single

photon, which is 1.0 in an ideal solar cell. Quantum efficiency measurements gives spectral response data of the solar cell. Considering the difference in the energy between produced electron and input photon, by integration over the spectrum, efficiency can be calculated. External quantum efficiency (EQE) gives the ratio of the number of electrons collected from a solar cell and input light. On the other hand, internal quantum efficiency (IQE) defines extracted electron from a solar cell divided by absorbed photon. In IQE, optical losses are also considered and that is the reason why it is higher than the EQE. By a simple conversion, IQE can be extracted from EQE as given in Eq. 9.

$$IQE = \frac{EQE}{1 - Reflection - Transmission}$$

(Eq. 9)[28]

1.3. Solar Cell Technologies

1.3.1. Si Wafer Based Solar Cells

First p-n junction solar cells made by melting doped Si on top of each other as shown in Figure 7 at 1941 [10]. Within a short time, efficiency of Si solar cells managed to reach to 10%. Today, Si wafer based solar cells still dominates the solar energy market with more than 90% market share [29]. Si wafers can be produced by different methods. Czochralski growth [30] results with pure and single crystal while directional solidification system (DSS) [31] produces cheaper wafers that are multi crystalline. In addition to these, for crystal production with higher purity, float-zone method [32] is usually preferred. Several modifications are made to decrease the cost of the wafer such as quasi-mono wafer production by DSS and continuous Czochralski growth.

12
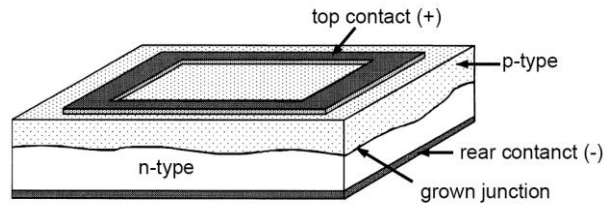
Figure 7. Silicon solar cell reported in 1941 formed by slowly solidified Si [10].

Most of the wafers used in solar cells are multi-crystalline Si wafers, which has market share of 60% in Si wafer based technology. However, it is expected that the mono crystalline Si wafers will increase its share in the upcoming years because of emerging solar cell concepts that make use of mono-crystalline wafers. In addition, float-zone (FZ) wafers will also gain popularity in efforts of making high performance solar cells [29]. Figure 8 shows the industrial multi and mono crystalline Si solar cells.
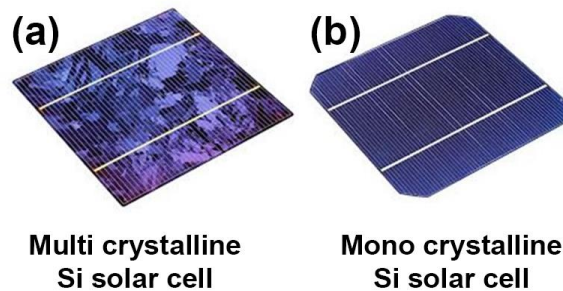
Figure 8. Full size (a) multi and (b) mono crystalline solar cells [33]

In the standard solar cells, metallization is done by Al coating on the backside of the wafer and Al creates back surface field (BSF) by diffusion into Si wafer and by doping it. The BSF helps the separation of electron-hole pairs [34] and this standard structure gives around 18-19% efficiency [35]. Improving the cell structure by decreasing the losses resulted with 26.6% record efficiency obtained by heterojunction of a-Si and crystalline wafer (HIT) [36]. In addition to HIT solar cells, there are

13

different alternatives to enhance the efficiency of Si wafer based solar cells. Taking the junction and contacts all to the back side of the wafer (interdigitated back contact solar cells – IBC [37]), improving passivation at the back side (passivated emitter and rear contact – PERC/PERL [35]), making contacts from the back side by physical holes on the wafer (emitter wrap through – EWT [38] and metal wrap through – MWT [39]) are some of these alternatives.

1.3.2. a-Si:H Thin Film Solar Cell

Si wafer based solar cells require 180-200 µm thickness due to handling issues and low absorption coefficient at near band-gap energies. It is found out that a-Si have higher absorption coefficient but the band-gap of a-Si is smaller than that of c-Si (1.5 eV for a-Si:H and 1.1 eV for c-Si). Apart from the band-gap, high density of defects also decreases the efficiency. As a result, a-Si is needed to be hydrogenated to passivate defect states. In a-Si:H thin film solar cells, only a fraction of a Si is used (1-2 µm) as an advantage to decrease the cost of solar electricity. In addition, the cells can be manufactured on different substrates like glass, Al foil, PET, etc. in module size. In Figure 9, an example of a-S:H solar module produced on flexible substrate can be seen.
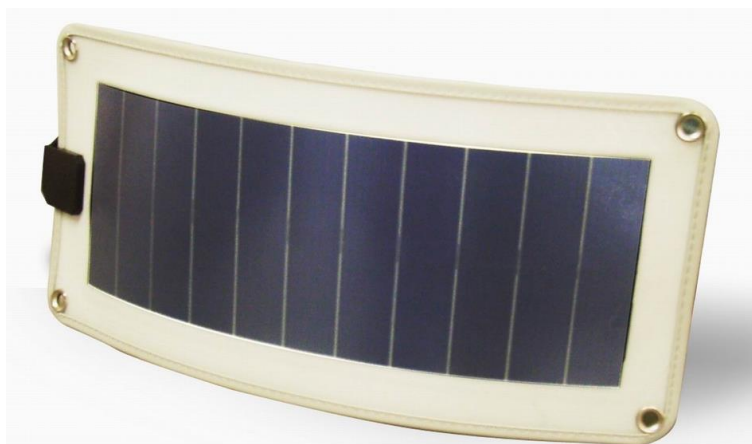
Figure 9. a-Si:H solar module on flexible substrate [40]

In a-Si:H solar cells, an intrinsic region is used in between p and n type regions. Doping of a-Si:H increases the recombination on a-Si:H solar cells. The doped regions are fabricated thin enough to minimize recombination and intrictic layer is added so that the internal electric field between p and n regions can be extended in amorphous Si. A schematic diagram of an a-Si:H solar cell is given in Figure 10. The contact from the p-type region is taken by depositing transparent conductive oxide (TCO) between glass and a-Si:H. Bottom contact is, however can be made by Al or Ag.
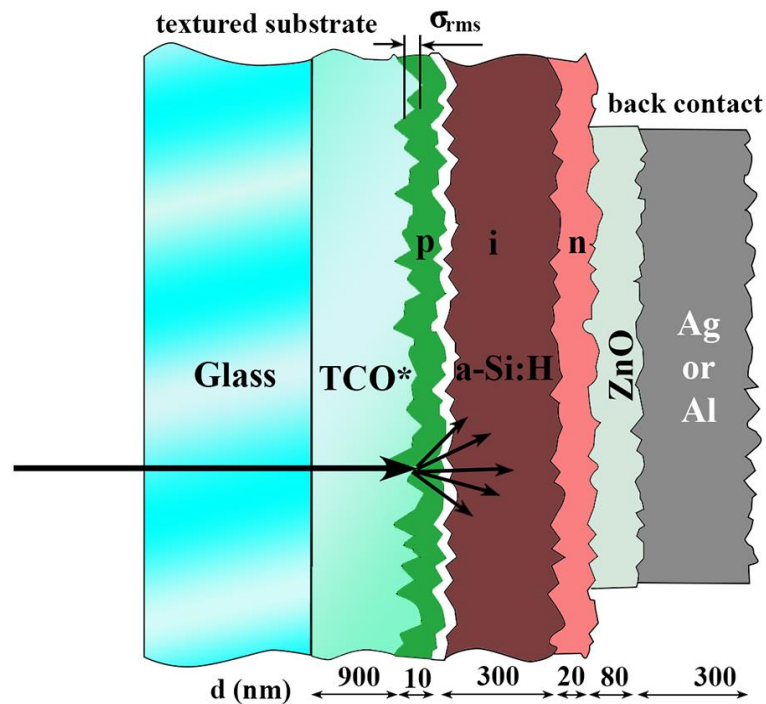
Figure 10. Schematic representation of a-Si:H solar cell [41]**.**

The first obtained efficiency value for a-Si:H was around 2.4% [42] for AM 1.0 and today, it is possible to obtain 14% efficiency by making triple junction a-Si:H solar cell [36]. a-Si:H solar cell have shown the possibility of obtaining remarkable efficiencies by using small amount of material and making large area productions.

15

1.3.3. CdTe and CIGS Solar Cells

Cadmium telluride (CdTe) thin film solar cell holds 60% share in the produced electricity from thin film solar cells [4]. CdTe solar cell concept was presented in 1972 with p-CdTe/n-CdS configuration as an alternative for n-CdTe/p-Cu$_2$Te because the latter have device instabilities like diffusion of Cu [43]. CdS was used as an window layer having around 2.5 eV band gap while CdTe have nearly 1.5 eV band gap [44] as shown in Figure 11. CdTe solar cells offer minimum energy payback time that is 1.0 year [45].
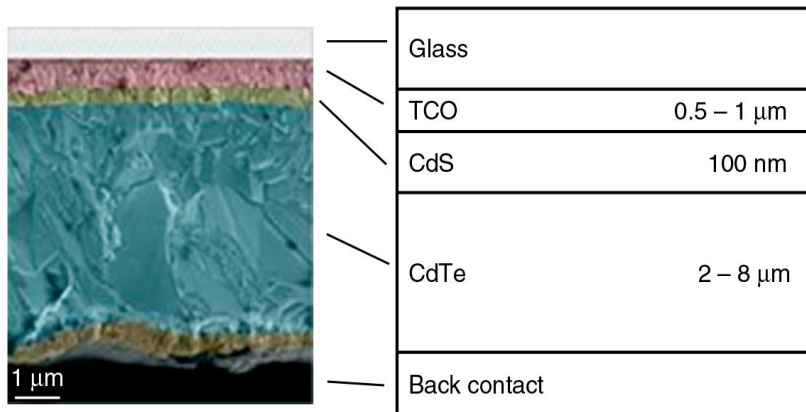
Figure 11. Cross-sectional SEM image of the CdTe solar cell alongside with the schematic representation [43]**.**

Another common type thin film solar cell, which produces around 26% of electricity provided by thin film technologies, is copper indium gallium diselenide (CIGS) solar cell structure [4]. CIGS solar cells have the structure given in the Figure 12. CIGS absorber layer is sandwiched in between Mo and a buffer layer that is commonly CdS. Copper indium diselenide is the initial structure for this technology which has a band-gap around 1.0 eV. Addition of Ga to the structure, changes the bandgap in between 1.1 eV to 1.4 eV [46].

16
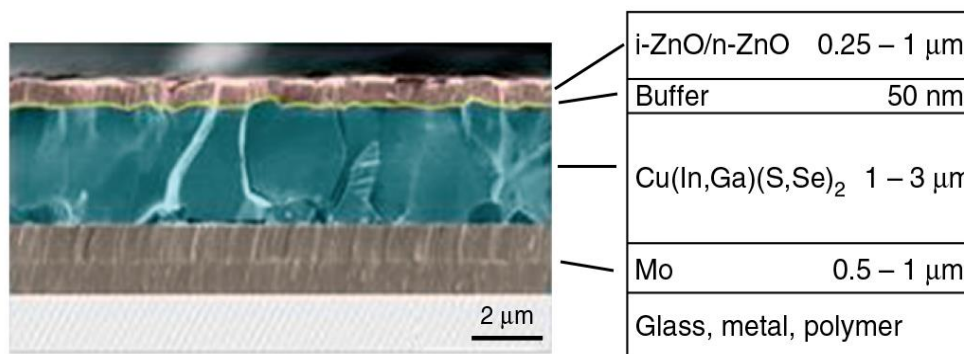
Figure 12. Cross-sectional SEM image of the CIGS solar cell alongside with the schematic representation [43]**.**

1.3.4. Dye Sensitized, Organic and Perovskite Solar Cells

It is also possible to obtain light induced current by organic structures or the combination of organic and inorganic structures. These type of solar cells can be produced in ambient atmosphere and by spin coating, which makes these type of solar cells cheap and attractive for researchers.

The recreation of excited chlrophyll molecule in ZnO electrode at 1972 by Helmut Tributsch showed that it is possible to inject exited electron to a wide band gap semiconductor [47]. ZnO was a single crystalline layer in this structure. Employment of nanoporous TiO_2 for dye sensitized solar cells (DSSCs), which is also called as Grätzel cell, has increased the efficiency of this technology up to 7% in 1991 [48]. Today, efficiencies of DSSCs can reach up to 11.9% [36].

The working principle and structure of DSSC is different from conventional p-n junction. Instead of having a valance and conduction band, there are LUMO and HUMO levels. The exited electron from HUMO to LUMO level is injected to the wide bandgap semiconductor that is in nanoporous scructure. The electron is transported within this material and then taken out from the device. The vacancy that is left behind is filled by an electron from electrolyte by $3I^-$ to I_3^- conversion [49]. The schematic diagram of DSSCs and working principle is summarized in Figure 13.
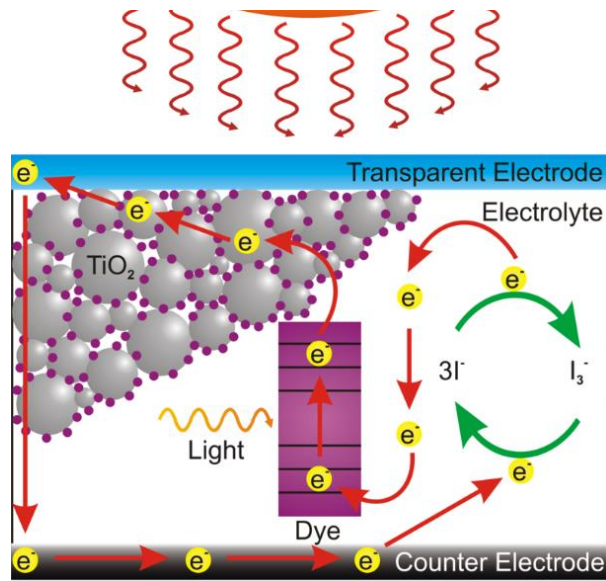
Figure 13. Operation principle and schematic representation of dye sensitized solar cells [50]**.**

Organic solar cells, on the other hand, have planar structure and the absorber organic molecule or polymer is sandwiched between two different electrodes. The separation of electron-hole pairs is done by electric field induced due to asymmetric ionization energy of electrodes as shown in Figure 14 [51].
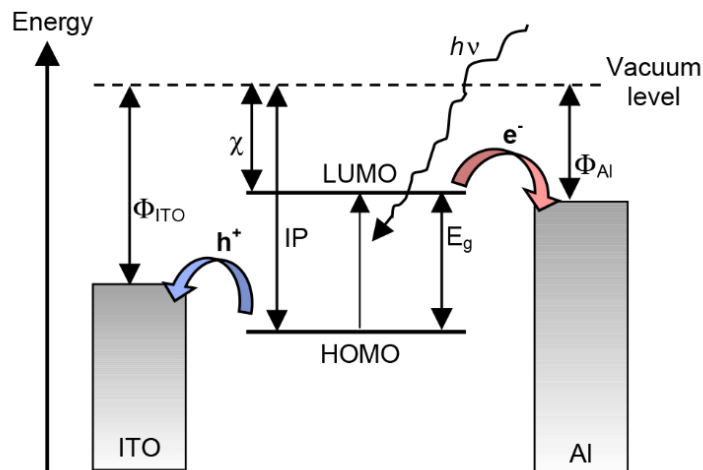
Figure 14. Working principle of organic solar cells [51]**.**

The efforts to increase the efficiency of DSSCs and organic solar cells lead to discovery of perovskite solar cells. Perovskite is a mineral having ABX_3 structure. Perovskites used for production of solar cells are hybrid materials having both organic and inorganic components. Perovskite solar cells are manufactured in planar form. First solar cell applications had 10.9% efficiency in 2012 [52]. Nowadays, the efficiency of perovskite solar cells has reached 22.1% [36]. However, there is still exists instability problem in this technology.

Thin film technologies, which are summarized above, can compete with the c-Si wafer based solar cells. However, it is essential to decrease the cost of produced solar electricity further to increase the market share of these technologies. This decrease in the cost of solar electricity is possible by employment of an effective light trapping scheme that enhances the efficiency. In the following chapters, different light trapping methods will be discussed. This thesis focuses on one of these light trapping schemes, which is aluminum induced texturing (AIT) method. AIT process was optimized and developed in order to increase the scattering behavior of the glass substrate and thus, to enhance the efficiency of thin film solar cell technologies.

CHAPTER II

LIGHT MANAGEMENT IN SOLAR CELLS

When light passes through an interface, some fraction of the light intensity is lost, which is proportional with the refractive index difference between 2 mediums. This lost is called as reflection. This radiation loss corresponds to approximately 40% for Si/air interface [53]. Moreover, the absorption property of a solar cell changes over the spectrum as given in Figure 15. Increasing the wavelength causes decrease in the absorption coefficient that can be described as in Eq. 10.

$$\alpha = \frac{4\pi k}{\lambda}$$

(Eq. 10)[53]

where α is the absorption coefficient, k is the extinction coefficient and λ is the wavelength of the incident light. The absorption coefficient of a semiconductor determines the optimal thickness of it according to Beer-Lambert law given below.

$$\Phi = \Phi_0 e^{-\alpha l}$$

(Eq. 11)

where Φ_0 is the initial intensity, Φ is the final intensity and l is the thickness of the absorber material. As shown in Figure 15, absorption coefficient decreases near the band-gap, which causes some portion of the light to be transmitted from the semiconductor, especially in semiconductors with indirect bandgap such as c-Si solar cells.
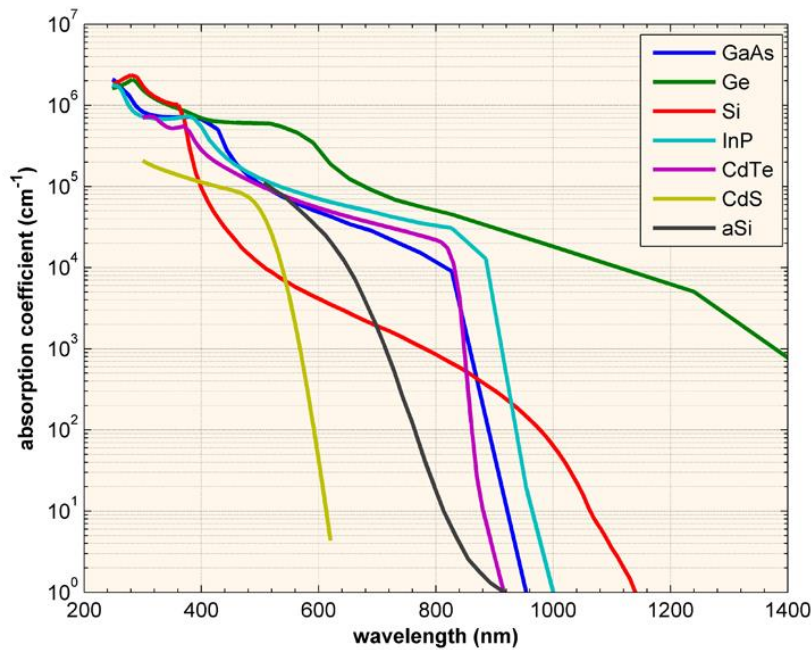
Figure 15. Absorption coefficient of different semiconductor materials used in solar cells at 300 K over solar spectrum [54]**.**

It is possible to decrease the optical losses by employing light trapping methods. An effective light trapping scheme can increase the optical path length in the absorber layer by the factor of $4n^2$, which is called as Yablonovitch limit [55]. For silicon, it means 74 reflections in the material before light escapes for the case of air/silicon interfaces. Several different approaches are employed to increase the optical path length. Anti-reflective coating (ARC), textured interfaces and nanoparticles are main techniques to be used as a light trapping method.

2.1. Anti-Reflective Coatings (ARC)

High differences in the reflective indexes of two medium results with high reflection. Anti-reflective coatings provide high transmittance by adding intermediate reflective index thin film materials between two mediums. For example, for c-Si

wafers, SiN_x is employed as ARC layer with n=2.2 [56] while refractive index of c-Si is 4.3. With this construction, reflection can be minimized as low as 0% for certain wavelengths as seen in Figure 16.
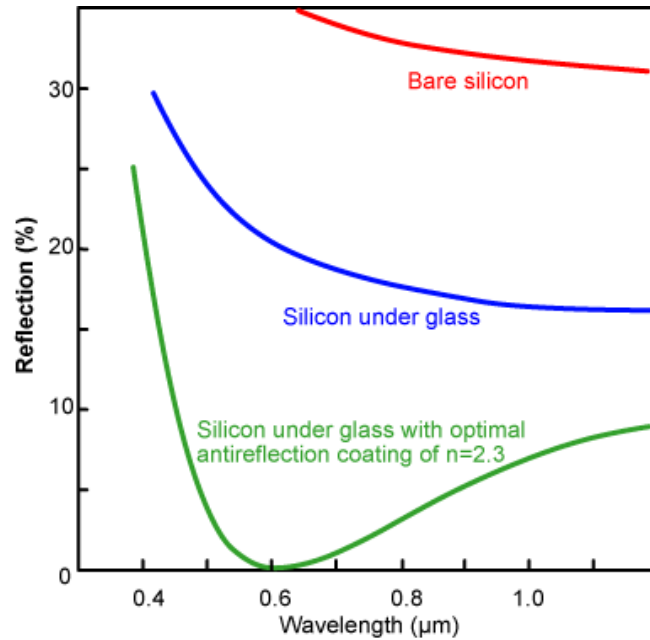
Figure 16. Comparison of reflections from c-Si solar cells for bare silicon, silicon under glass and silicon under glass with anti-reflective coating of n=2.3 [57]**.**

In addition to refractive index, the thickness is also important. If there is a phase difference between the reflection with odd multiples of $\lambda/4$ from the front and the back surface of ARC, two reflections cancels each other and no reflection occurs. In other words, the thickness should be an odd multiple of $\lambda/4$ to obtain zero reflection [58].

There exist several ways in addition to thin layer coating to obtain anti-reflection phenomenon. A homogenous film can be coated on the surface as in the case of SiN_x anti-reflective films or inhomogeneous films can be employed, which is a film having transition in the reflective index through the thickness of the film.

2.1.1. Homogenous Anti-Reflective Coating

Homogenous ARCs are formed with a thin film having the thickness with the requirement of $d=\lambda/4$ for the wavelength λ, where zero reflection is desired. In addition, reflective index of n_{arc} should be $\sqrt{n_s n}$, where n_s is the refractive index of the subjected medium and n is the refractive index of the surrounding. ARC can be a continuous, patterned or multiple films as presented in Figure 17 with refractive index profiles.
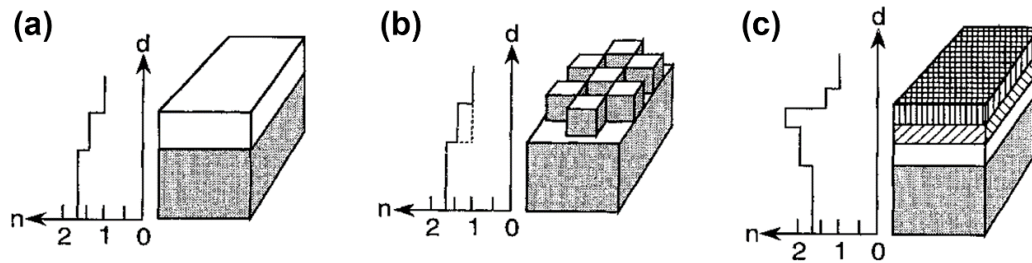
Figure 17. Schematic representation and refractive index profile of different type of homogeneous anti-reflective coatings. (a) continuous thin film, (b) patterned thin film and (c) multiple layer [59]**.**

Unlike the continuous thin film ARCs, patterned ARCs have refractive indicies that depend on the pattern. In addition, the film can also be the same material as the substrate. Throughout the thickness of the film, there are empty regions in nanometer scale. Due to the fact that the size of these regions are smaller than the wavelength, light acts like the film that is one continuous film. This film has a refractive index in between the substrate and the surrounding, air, directly related with the fraction of the air in the film [59].

The anti-reflection efficiency of ARC can be improved by using multiple layers. Each layer offers smooth transition from air to substrate. For example, it is possible to coat double SiN_x layer with different refractive indices. Another example

is the usage of SiN_x, SiO_2 layers in order to decrease the reflection more than the one-layer case. In this case, total reflectance can be lowered to 0.044 for SiN_x-SiO_2 double layer ($n_{nitrite}$=2.67, $d_{nitrite}$=49nm, n_{oxide}=1.55 and d_{oxide}=94nm) whereas total reflectance is 0.104 for single SiN_x layer for the case of n=1.95 and d=81 nm [60].

2.1.2. Inhomogeneous Anti-Reflective Coatings

Inhomogeneous anti-reflective coatings have the property that the refractive index changes throughout the thickness. The refractive index decreases gradually from sample to the air, which acts as infinite number of thin films with different refractive indices. The thickness of the film is not crucial due to the fact that refractive index profile of multiple homogenous anti-refractive layers are obtained in one single layer, which reduces the reflection from multiple interfaces [59].
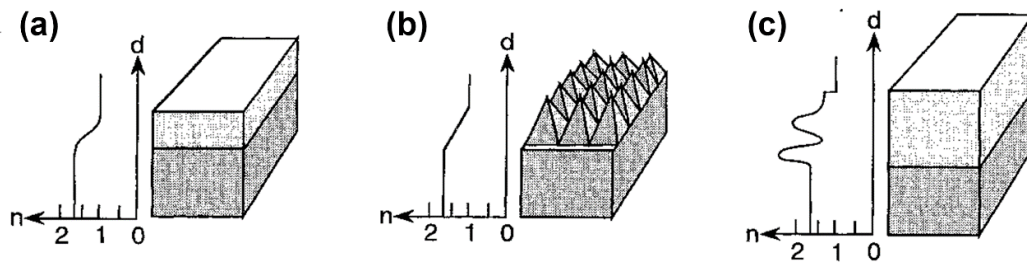
Figure 18. Schematic representation and refractive index profile of different type of inhomogeneous anti-reflective coatings. (a) continuous thin film, (b) structured thin film and (c) complex [59].

In-homogeneously patterned films have different air/material ratio along the thickness. As a result, a gradually decreasing refractive index is obtained. On the periodically pyramid structured surface [Figure 18(b)], the change in the refractive index have line profile. However, by using different patterns, it is possible to obtain parabolic, cubic and quantic index profiles [58]. Textured surfaces can act as

25

inhomogeneous patterned films if the dimensions of the structure are smaller than or comparable to the wavelength of the light.

2.1.3. Anti-Refractive Layer

The anti-refractive layer is formed from the base material through chemical etch processing. Due to not having a physical interface, these type of layers are more resistant to external corrosive factors like wind, rain, temperature, etc. The anti-refractive layer technique can be applicable to glasses due to having different composites. By selective etching, porous layer can be produced on the substrate and this layer has the same profile as inhomogeneous continuous thin film anti-refractive coating. There are two different reported methods to form anti-refractive layer on the glass.

Xiong et al. [61] suggest that KOH etching for couple hours at 95 °C followed by rinsing by DI water can form porous layer on the glass due to ion-exchange mechanism during KOH etching. In KOH etching, high concentration of OH^- replaces with glass modifier cations such as Na^+, K^+, Ca^{2+} etc. in the glass. This ion-exchange process open voids on the surface of the glass to enable water to penetrate into the glass. Thus, corrosion by water enlarges these voids and forms a porous layer as shown in Figure 19(a) and Figure 19(b). This porous layer can increase the transmittance of soda-lime glass from 90% to 97% [Figure 19(b)].
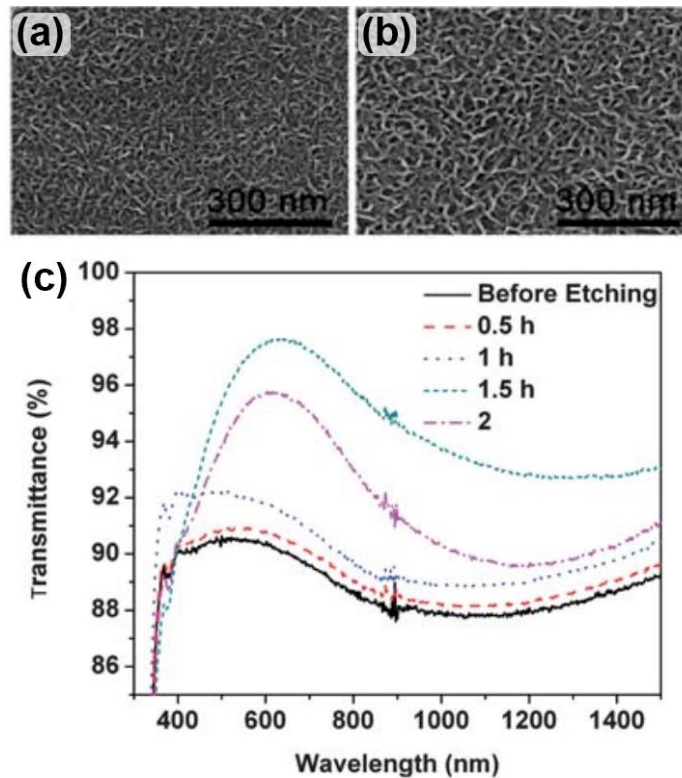
Figure 19. (a) and (b) Etched surface of soda-lime glass having different components for 12 hours and (b) change in the transmittance with the increase in the etching time [61]**.**

For an effective AR layer, the glass composition is also crucial as reported by Xiong et al. [61] because cations in the glass are the basis of this process.

It is also possible to obtain AR layer by HF etching. However, it requires to suppression of the reaction between HF and SiO_2. Etching glass with $HF:K_2SiF_6$ results with a porous layer formation. Si^{4+} cations in the solution suppresses the reaction with SiO_2 in the glass. As a result, other components are removed from the glass [62]. The resultant surface structure is given in Figure 20(a). This layer increases transmittance to 98.2% from 95.7% for the light having 598 nm wavelength as shown in Figure 20(b).
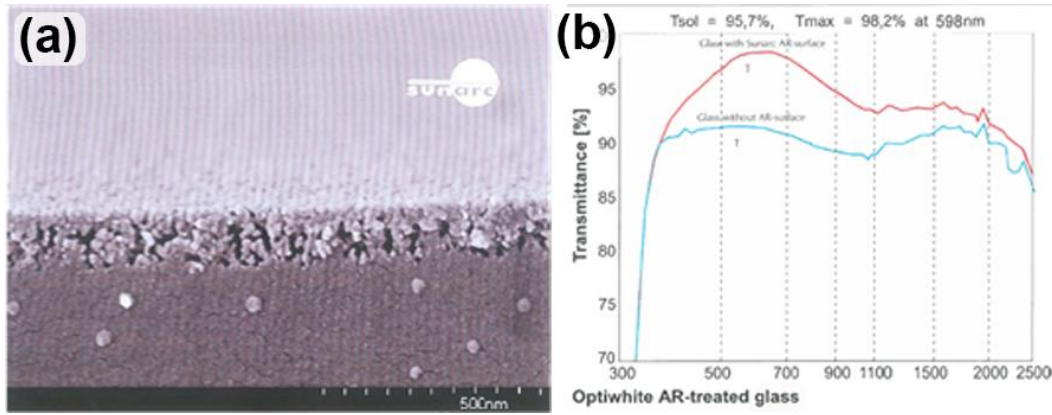
Figure 20. HF:K$_2$SiF$_6$ etching of the glass. (a) cross sectional SEM image of porous layer and (b) transmittance of processed glass compared with standard glass [63]**.**

These type of glasses having anti-refractive layer are compatible with c-Si wafer based technologies to be used as a module glass.

2.2. Back Reflectors

Back reflectors increase the optical path length by simple reflection process. For thin film solar cells, addition of transparent conductive oxide layer before metallization of back surface increases the reflection. The schematic presentation of a solar cell having back reflector is given in Figure 21. For thin film Si solar cells, ZnO:Al is coated in front and back surface of absorber layer. ZnO:Al has lower refractive index than Si ($n_{ZnO:Al} \approx 2.0$ [64] and $n_{SiO_2} \approx 3.5$ [65]), which results with higher reflection into the absorber layer. By this method, it is possible to obtain 10% enhancement in solar cell conversion efficiency [66].
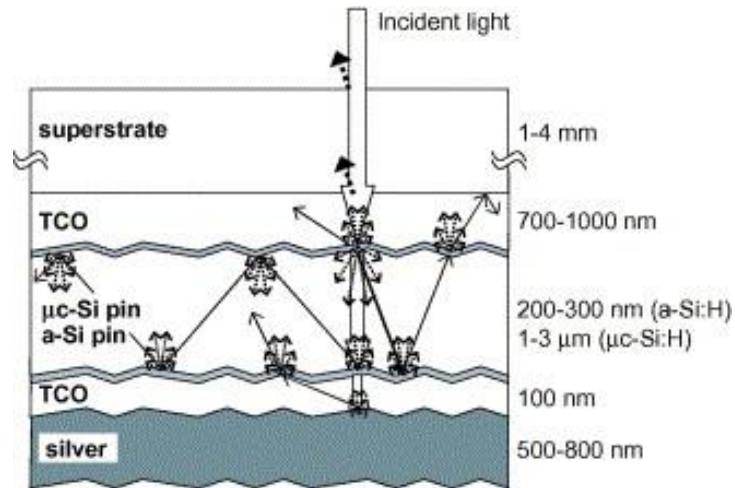
Figure 21. Scattering mechanism in thin film solar cell having TCO at the back surface as a back reflector[67]**.**

Furthermore, white paint can also be used as a back reflector. Pigmented white paint, coated by simple spray paint scatters and reflect the light as shown in Figure 22. With this simple method, J_{sc} can be enhanced up to 20% [68].
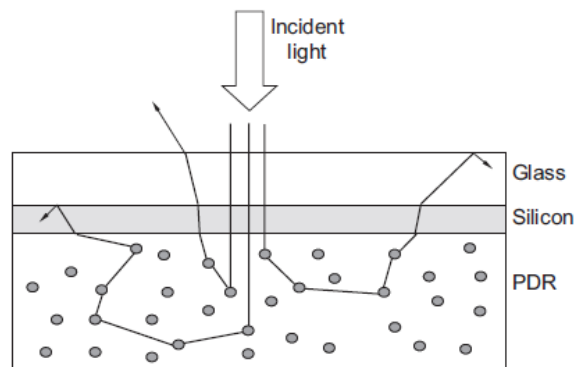
Figure 22. Schematic representation of the scattering effect of PDR [68]**.**

2.3. Plasmonic Metal Nanoparticles

Another approach for effective light trapping scheme is the implementation of plasmonic metal nanoparticles to manipulate the light with structures having sub-wavelength dimensions [69], [70]. Free electron in the metal can interact with E-field

of the light and polarization of the surface occurs [Figure 23(a)]. If this interaction occurs with metallic nanoparticles with dimensions smaller than wavelength of the light, plasmons are formed as shown in Figure 23(b) [69]–[71].
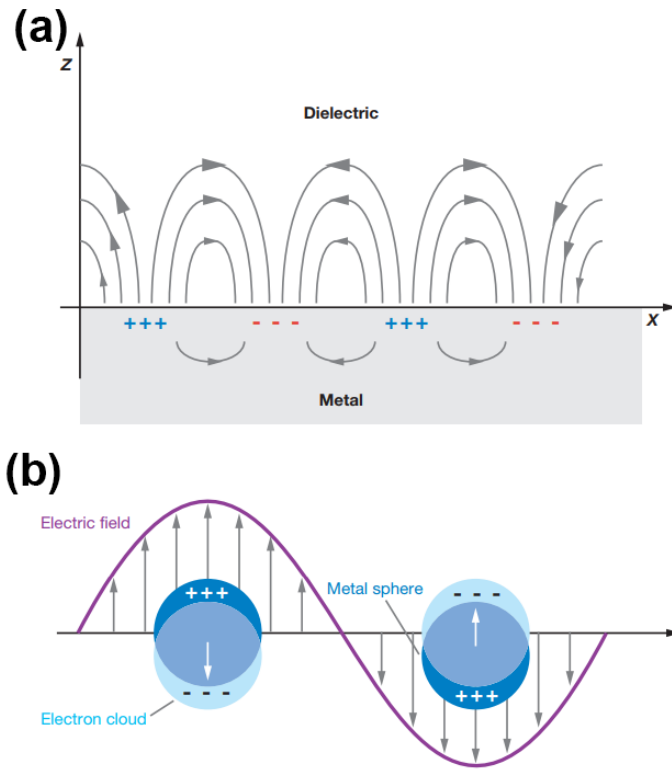
Figure 23. (a) propagating plasmon and (b) localized surface plasmon [71]**.**

Plasmonic nanoparticles can absorb light having specific wavelength values which is called as localized surface plasmon resonance (LSPR). LSPR depends on nanoparticle size as well as the wavelength of the light. Metallic nanoparticles can act as scattering structures even though they have sub-wavelength dimensions. Due to this effect, it can be used in the front surface as a scattering interface or as a back surface reflector. In addition to scattering behavior, due to the interaction with light, propagating E-field is formed around the metallic nanoparticles. Implementation of metallic nanoparticles into the junction, E-field can be enhanced and thus, the charge separation efficiency can be enhanced [70] [72]. Different usage of plasmonic metal nanoparticles are given in Figure 24.
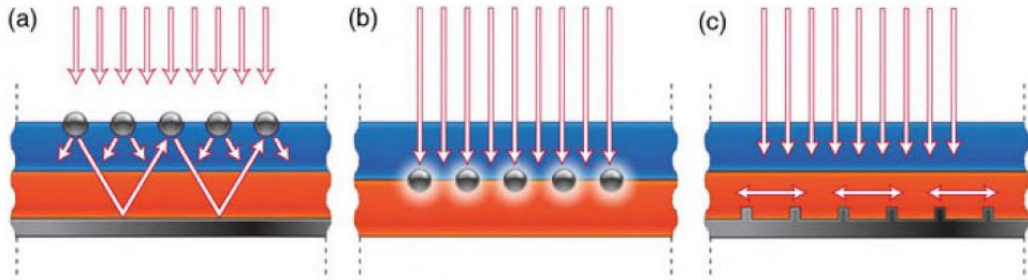
Figure 24. Plasmonic nanoparticles in solar cell structure. (a) nanoparticles on top of a solar cell, (b) embedded nanoparticles inside solar cell structure and (c) nanoparticles placed at back reflector side [70]**.**

Some examples are given in Figure 25(a) for Ag nanoparticles on glass, a-Si:H and SiN$_x$. It is reported that overall short circuit current of thin film solar cell increases from 13.1 mA/cm^2 for flat cell to 15.1 mA/cm^2 for plasmonic solar cell. The fill factor (FF) of this structure increase from 60.3% for flat cell to 64.5% for plasmonic solar cell. Increase in J$_{sc}$ and FF(%) is resulted from scattering effect of Ag nanoparticles. The EQE and transmission of this structure are given in Figure 25(b).
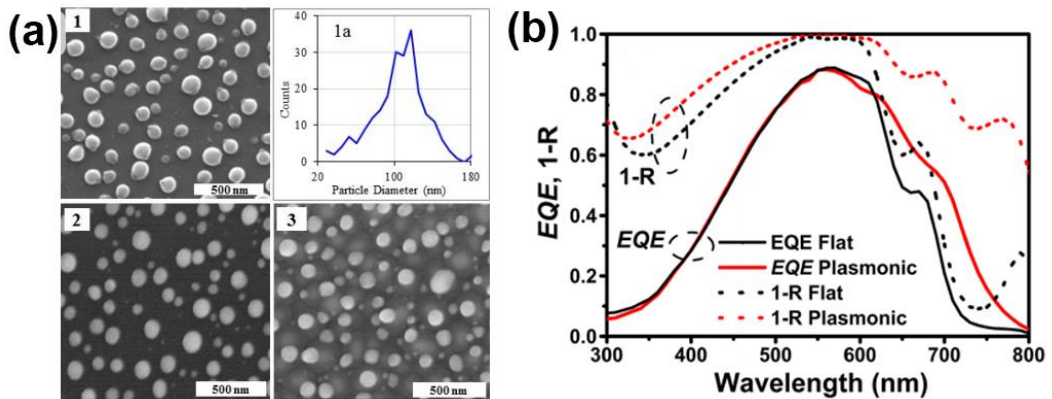
Figure 25. (a) Ag nanoparticles on different substrates. (1) glass, (2) a-Si:H and (3) SiNx. (1a) shows particle size distribution on glass substrate [72] **and (b) External quantum efficiency of plasmonic solar cell with a reference cell** [73]**.**

2.4. Surface Texturing

Textured interfaces induce secondary reflection on the surface that can increase the transmission. In Figure 26, a comparison between flat surface and triangular textured surface in 2D can be seen.
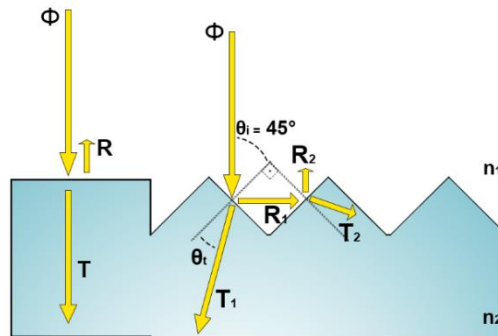
Figure 26. Reflection and transmission of light from flat and textured surface having 45° surface angle, where n_1= 1.5 which is c-Si and n_2=1.0 which is air for this specific example.

Variables used in Figure 26 are given in Table 1.

Table 1. Variables used in Figure 26.

Φ	Initial intensity
R	Reflected light intensity
T	Transmitted light intensity
n_1	Refractive index of the medium where light is coming and reflected (taken as 1.0, air)
n_2	Refractive index of the medium where light is transmitted (taken as 1.5, glass)
θ_i	Initial angle of the light to the normal of the surface
θ_r	Angle of the reflected light to the normal of the surface
θ_t	Angle of the transmitted light to the normal of the surface

According to Snell's law given in Eq. 12, the angle of transmitted light (θ_t) becomes 28.13°.

$$n_1 \sin \theta_1 = n_2 \sin \theta_t \qquad \text{(Eq. 12)}^{[74]}$$

In addition, light is reflected with the same angle to the normal of the surface. For this reason, angle of incidence and transmittance is equal, $\theta_i = \theta_t$.

Reflection of the light changes with the polarization. When light is reflected from the surface with an angle θ_r, the intensity changes according to s and p polarization of the light. Reflection for s-polarized light can be found according to Eq. 13 given below.

$$R_s = \left| \frac{n_1 \cos \theta_i - n_2 \cos \theta_t}{n_1 \cos \theta_i + n_2 \cos \theta_t} \right|^2 \qquad \text{(Eq. 13)}^{[74]}$$

for p-polarization, on the other hand, the equation becomes as given in Eq. 14;

$$R_p = \left| \frac{n_1 \cos \theta_t - n_2 \cos \theta_i}{n_1 \cos \theta_t + n_2 \cos \theta_i} \right|^2 \qquad \text{(Eq. 14)}^{[74]}$$

The total intensity of the reflection, R, can be found by;

$$R = \frac{1}{2} \left(R_s + R_p \right) \qquad \text{(Eq. 15)}^{[74]}$$

According to the example in Figure 26, The total reflection from flat surface is:

$$R_s = \left| \frac{1 \cos 0° - 1.5 \cos 0°}{1 \cos 0° + 1.5 \cos 0°} \right|^2 = 0.04 \qquad \text{(Eq. 16)}$$

$$R_p = \left| \frac{1 \cos 0° - 1.5 \cos 0°}{1 \cos 0° + 1.5 \cos 0°} \right|^2 = 0.04 \qquad \text{(Eq. 17)}$$

$$R = \frac{1}{2}(0.04 + 0.04) = \mathbf{0.04} \qquad \text{(Eq. 18)}$$

In planar surfaces, 4% of the initial intensity is lost due to the reflection from the front surface. On the other hand, textured surface provides lower reflection values. For this case, surface having triangles with 45° angle provides different intensities for different polarizations. The intensity of first reflection becomes:

$$R_{s1} = \left| \frac{1 \cos 45° - 1.5 \cos 28.13°}{1 \cos 45° + 1.5 \cos 28.13°} \right|^2 = 0.0920 \qquad \text{(Eq. 19)}$$

$$R_{p1} = \left| \frac{1 \cos 28.13° - 1.5 \cos 45°}{1 \cos 28.13° + 1.5 \cos 45°} \right|^2 = 0.0085 \qquad \text{(Eq. 20)}$$

$$R_1 = \frac{1}{2}(0.0920 + 0.0085) = \mathbf{0.05} \qquad \text{(Eq. 21)}$$

The first reflection carries 5% of the initial light intensity. Then the reflected light falls on the another triangle with 45° angle normal to the surface. The light splits into two components, R_2 and T_2. T_2 is transmitted with an angle of 28.13° and R_2 is reflected with an angle of 45°. The resulting intensity of R_2 is 0.05 of the incoming light that is R_1. In total, 0.25% of the light is reflected and 99.75% of the light can be transmitted.

In addition to front surface texture, on the back textured surface, high amount of the light intensity is reflected due to passing from high reflective index medium to

low reflective index medium. In this way, light can make multiple passes in the medium before escaping.

In addition to increase in the transmittance, according to Snell's law given in Eq. 11, light falling on a surface with an angle scattered from the surface. The amount of the scattered light is defined by haze given in the equation below. Haze is defined as the ratio of scattered light to total light intensity in the transmission or reflection.

$$Haze\ (\%) = \frac{Scattered\ light\ intensity}{Total\ light\ intensity}\ x100 \qquad \text{(Eq. 22)}^{[75]}$$

Different surface texturing methods are employed for various solar cell technologies. The surface texture could be formed by either random structures or periodic structures.

2.4.1. Texturing for c-Si Solar Cells

There exists many techniques for surface texturing. KOH (potassium hydroxide) or TMAH (tetra methyl ammonium hydroxide) texturing is generally used in commercial products. KOH and TMAH have anisotropic etching behavior, in which the rate of material removal reduces significantly in (111) plane. As a result, random pyramids are formed on the surface as presented in Figure 27(a). In addition, by employment of simple lithography techniques, periodic inverted pyramid texturing can be obtained [76] [Figure 27(b)]. The reflection can be minimized by forming nanowires [77] [Figure 27(c)], micro holes/rods [Figure 27(d)] formed by metal assisted etching that is conducted by partially coating the surface with gold or silver on the surface and etching by $HF:H_2O_2$ [78]. Micro holes also can be formed by reactive ion etching technique [79], which offers high aspect ratio. Additionally, wet chemical texturing by $HF:HNO_3$ [80] is employed for the random texturing of multicrystalline Si wafers because each grain offers different orientation, which

prevents pyramid formation on each plane and results with different etching rates on different grains. HF:HNO$_3$ forms rounded features as presented in Figure 27(e).
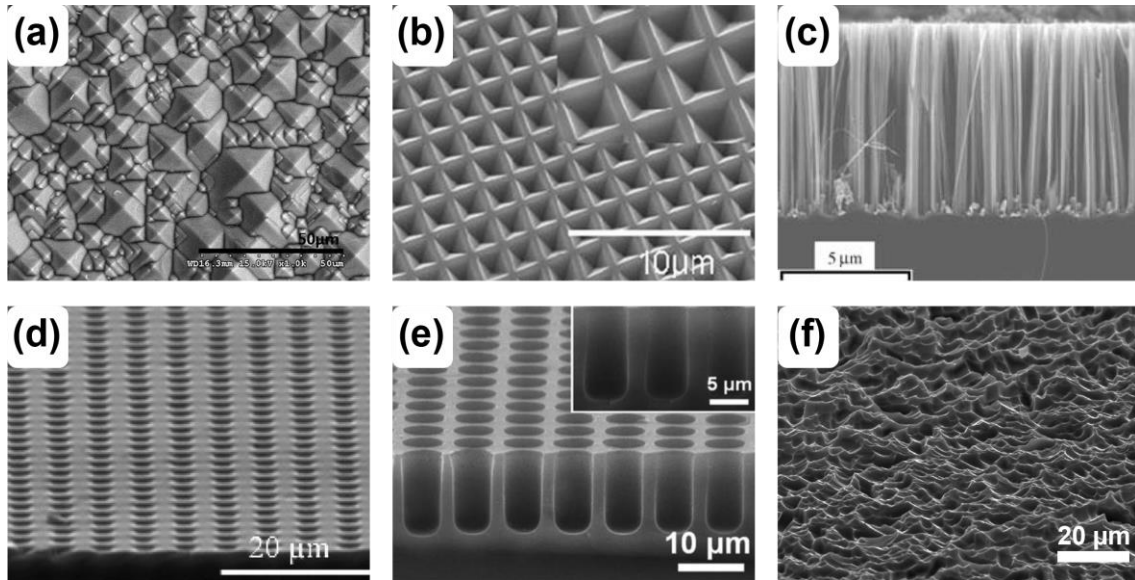
Figure 27. Different surface textures for c-Si solar cells; (a)KOH texturing [81]**, (b) inverted pyramid texturing** [82]**, (c) Nanowires formed by MAE** [83]**, (d) micro holes/rods formed by MAE** [84]**, (e) micro holes obtained by RIE** [79] **and (f) texturing of multicrystalline Si solar cells by HF:HNO$_3$** [80]**.**

2.4.2. Texturing for Thin Film Solar Cells

The light trapping by textured surfaces in thin film solar cells can be applied to transparent conductive oxide (TCO) and the substrate (glass or thin foil). Especially for a-Si:H solar cells, various approaches exist. The state of the art in the texturing is the periodic hexagonal, honeycomb substrate texturing which is done on SiO$_2$ thermally grown in Si wafer. Today, by making triple junction µc-Si:H solar cell on this honeycomb structure 14.04% stabilized efficiency can be obtained [5]. However, using Si wafers as substrate is considered as an expensive method. There are alternative texturing techniques employed to reduce production cost of solar electricity from thin film solar cells.
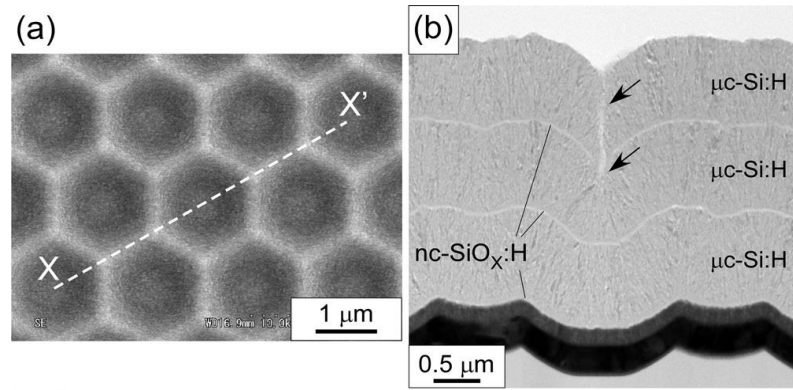
Figure 28. (a) Hexagonal surface texture on thermal oxide of Si wafer and the triple junction μc-Si:H solar cell [85]**.**

2.4.2.1. Transparent Conductive Oxide (TCO) Texturing

Transparent conductive oxide, which is usually ZnO:Al, can be coated on glass with RF or DC magnetron sputtering. Coated films have naturally rough surfaces as shown in Figure 29(a). However, ZnO:Al can be textured by diluted HCl (0.5%-2%) solution due to its anisotropic etching behavior [66], [86]–[88]. The resulting surface has U-shaped craters with micron sized dimensions as shown in Figure 29(b).
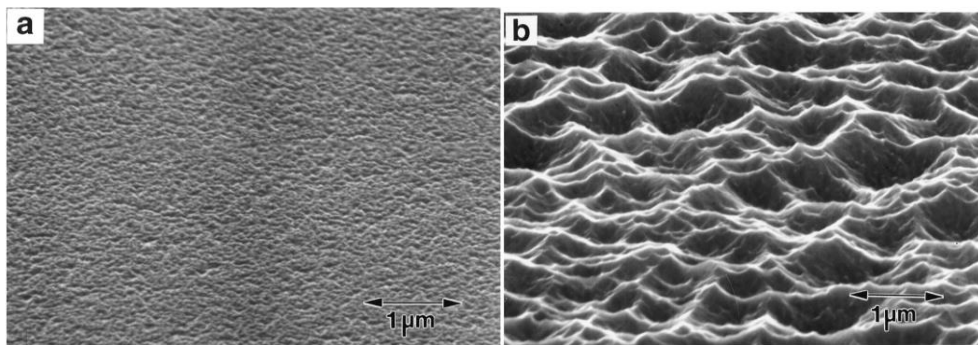
Figure 29. SEM image of RF sputtered ZNO:Al surfaces. (a) as deposited and (b) after HCl etching [87]**.**

Textured ZnO:Al surfaces can improve the quantum efficiency of thin film solar cells over the solar spectrum. An example for enhancement is given in Figure 30.

It is also reported that the efficiency (η) of a-Si:H solar cell can be increased to 10.2% from 9.0% by texturing the ZnO.
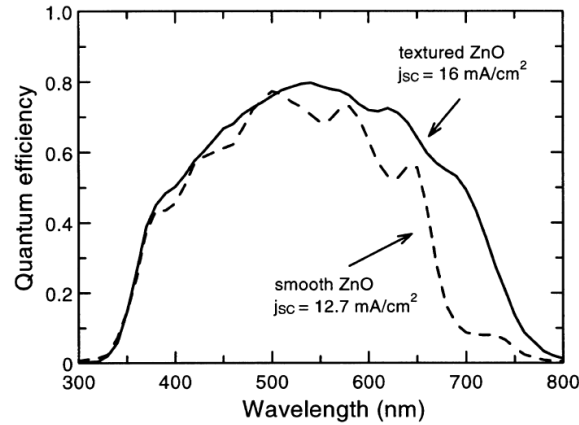
Figure 30. Quantum efficiency of a-Si p-i-n solar cells deposited on flat and textured ZnO coated glass substrate [87]**.**

2.4.2.2. Texturing of Glass Substrate/Superstrate

Texturing of glass surface can be employed for superstrate or substrate configuration. In the superstrate configuration, texture acts as a scattering back reflector [89]–[91]. On the other hand, substrate configuration enhance the optical path length by scattering the transmitted light [92]–[97]. In Figure 31, the effect of textured glass surface is explained. The scattering angle in solar cells having textured glass surface (θ_2) is higher than the solar cells having smooth glass surface θ_1 [98].

There exist various techniques to modify the glass surface periodically or randomly, such as dry etching, wet chemical etching, nano-imprinting, ZnO induced texturing (ZIT) and aluminum induced texturing (AIT), etc.
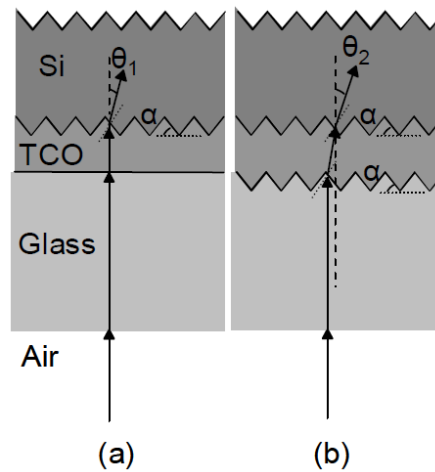
Figure 31. Schematic representation of a-Si:H solar cell with (a) flat glass/TCO interface and (b) textured glass/TCO interface [98].

2.4.2.2.1. Dry Etching for Texturing of Glass

Dry etching is conducted by corroding the glass by plasma or physical force like sandblasting. Plasma etching is usually used for microelectromechanical applications with SF_6/Ar plasma [99], [100]. However, thin film applicable texture can be formed by employment of nanoparticles as a masking material and reactive ion etching method to remove the glass from unmasked regions. After removing the metallic nanoparticles by wet chemical etching, the surface with sub-wavelength structure as shown in Figure 32 is obtained [94]. On the other hand, sandblasting is commercially used to obtain opal glasses. There are several attempts for producing both Si wafer based module and thin film solar cell compatible surface structures by sandblasting.
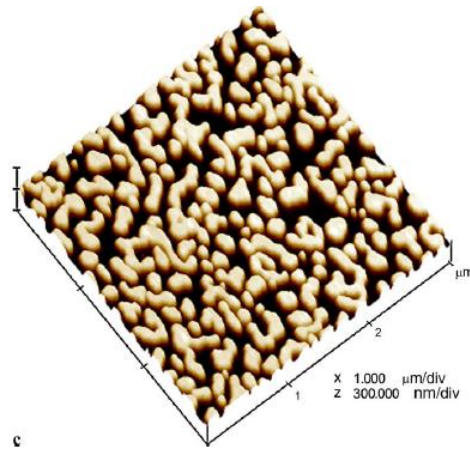
Figure 32. AFM image of the surface of RIE glass formed with Ag nanoparticle masking layer [94]

Sandblasting is achieved by sending nano or micro particles like SiC, SiO$_2$ with varying sizes. Accelerated particles by jet pressure physically damages the surface and alters it. As a result, a rough surface can be obtained [97]. This method can be employed to produce glass substrates for thin film solar cells [97] as well as to be used in c-Si wafer based solar modules as a window glass.

2.4.2.2.2. Wet Chemical Etching for Texturing of Glass

Apart from the usage of wet etching to selectively remove the glass components for anti-reflective purposes, addition of simple lithography step before chemical etching could result in textured surfaces. Simple HF etching after masking the surface forms periodic surface structures. HF starts to etch the glass from the openings and according to the shape of the openings, the texture is formed [101]. With the increase of HF etching time, structures enlarge and merge as seen in Figure 33 from (a) to (c). After the merging of each shape, damaged rough commissures smoothen with the increase of etching time and results in thin film compatible surface structure which can be transferred to following layers, which is shown in Figure 33(d).

40

The SEM image of AZO coated surface is given in Figure 34(a). In addition, optical measurements yield promising results with nearly 90% haze [Figure 34(b)].
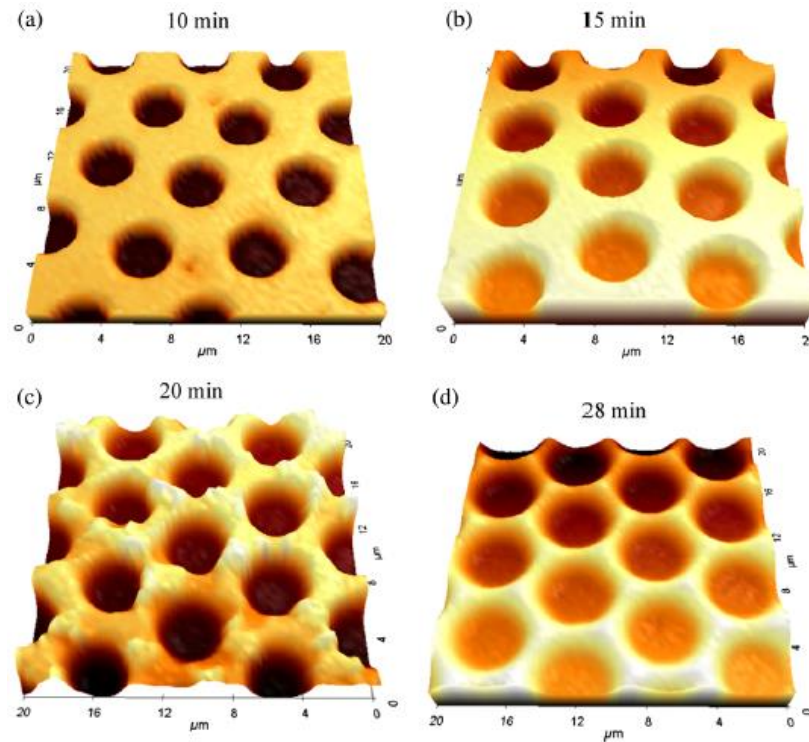
Figure 33. Different etching times with HF (1%) for honeycomb mask. (a) 10 min. (b) 15 min. (c) 20 min. (d) 28 min. [101]**.**
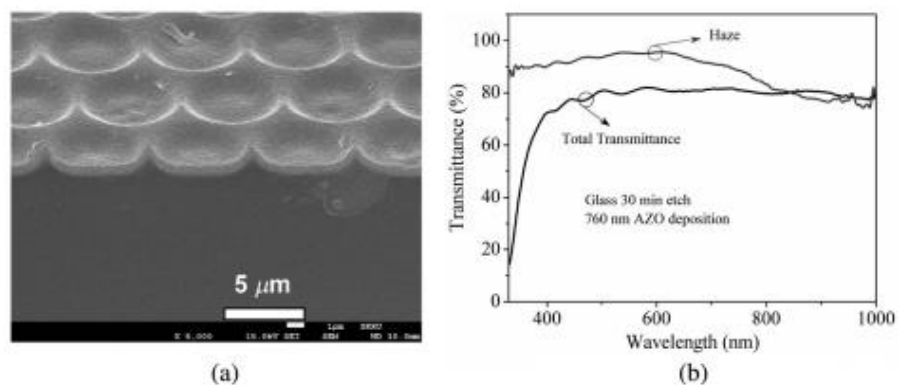
Figure 34. Periodically wet etched glass with 760 nm AZO layer. (a) cross sectional SEM image and (b) optical measurement results [101]**.**

2.4.2.2.3. Imprinting

Imprinting, which is also known as glass casting operation, is used to periodically texture the glass during production. It is basically a texture transfer from rolls to the glass surface. Various surface structures can be printed on rolls to produce different textures on the glass. Common structures used for solar modules are inverse and direct pyramids [102].

For thin film solar cell applications, besides, imprinting is conducted by structuring a glassy layer on the glass surface. The transferred texture can be the texture of ZnO:Al [103], random pyramids [104] or any other periodic or random thin film compatible structure. A soft polymer mold is coated on the master, which is the state-of-the-art surface texture. Then, the soft mold is separated from the master and heated at temperature more than the glass transition temperature of the polymer. Afterwards, the mold can be used to reproduce the master for multiple times on glassy soft layers [103]. An example for process flow of ZnO:Al master is given Figure 35.
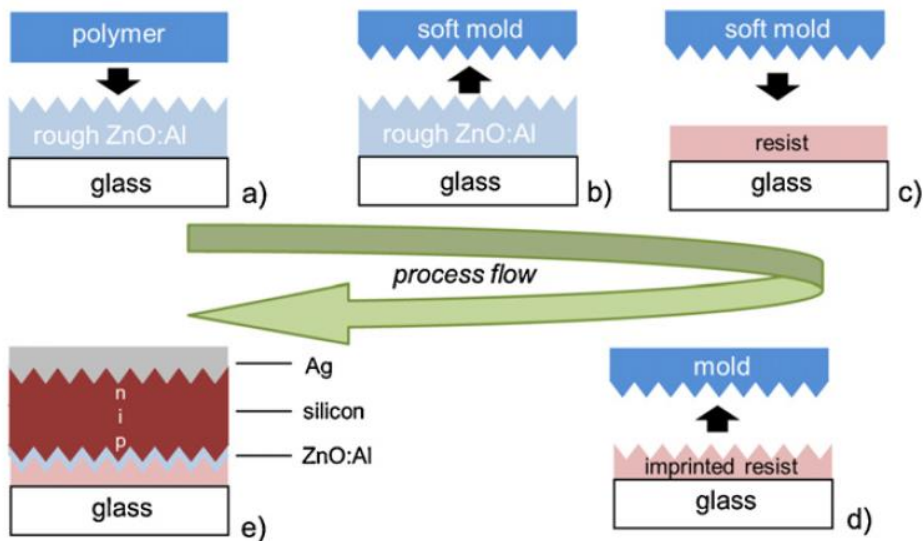
Figure 35. Process flow for nano-imprinting of ZnO:Al texture on glassy layer from (a) to (e) [103]**.**

2.4.2.2.4. ZnO Induced Glass Texturing (ZIT)

ZnO induced texturing (ZIT), which is also called as 3D texture transfer [98], requires sacrificial layer that is textured with desired structures. Because of the fact that ZnO:Al texturing is optimized and is a commercial process, it is prefered as a sacrificial layer for glass texturing. Textured ZnO is removed by ion beam etching [98]. The texture is transferred to the glass as shown in Figure 36.
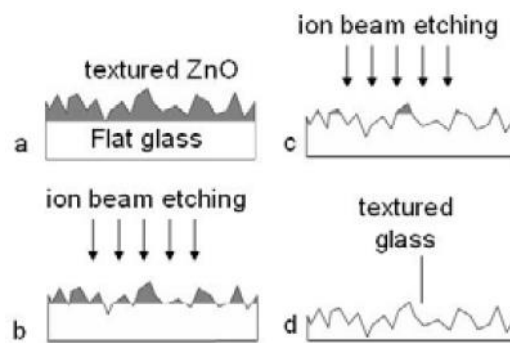
Figure 36. Process flow of ZnO induced texturing [98]**.**

2.4.2.2.5. Aluminum Induced Glass Texturing (AIT)

Aluminum induced glass texturing (AIT) is developed to produce an effective and cost-efficient texturing method [105]. For glass texturing methods, in which the lithography process is needed, are not large area compatible, large area production of solar cells is problematic where large area application is an advantage for thin film solar cells. Furthermore, texture transfer methods need a state-of-the-art master that is prepared perfectly or additional glassy layer between glass and transparent conductive oxide, which increase the processing costs. On the other hand, AIT can be employed by simple aluminum coating followed by annealing and etching, which results with U-shaped random craters [92], [106]. In addition, by changing parameters of AIT, it is possible to obtain surface structure having variety in feature size and roughness according to requirements [90], [107]. In AIT, a thin aluminum film, coated by thermal

43

evaporation or sputtering method, is used as a sacrificial layer to produce nano- and micro-sized craters on the surface of the glass [108]. The process is chiefly governed by the random redox reaction between Al and SiO_2 as shown below [75], [90], [109]–[112].

$$3SiO_2 + 4Al \rightarrow 3Si + 2Al_2O_3 \qquad \text{(Eq. 23)}$$
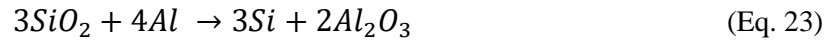
The redox reaction is induced by annealing the Al-coated glass at temperatures above 500 °C. Annealing temperatures between 500 and 620 °C have been reported [93], [105], [107], [111]–[114]. According to Huang et. al. [108], at the beginning of the annealing process, Al_2O_3 nodules are formed and grow inside of the glass, while Si dissolves into the surrounding Al and forms Si clusters. After annealing process, the reaction products are chemically etched, leaving behind a bare, textured glass surface. The reaction mechanism is schematically summarized in Figure 37. The surface structure can be altered by changing the parameters such as Al thickness, annealing temperature, etchants and rations.
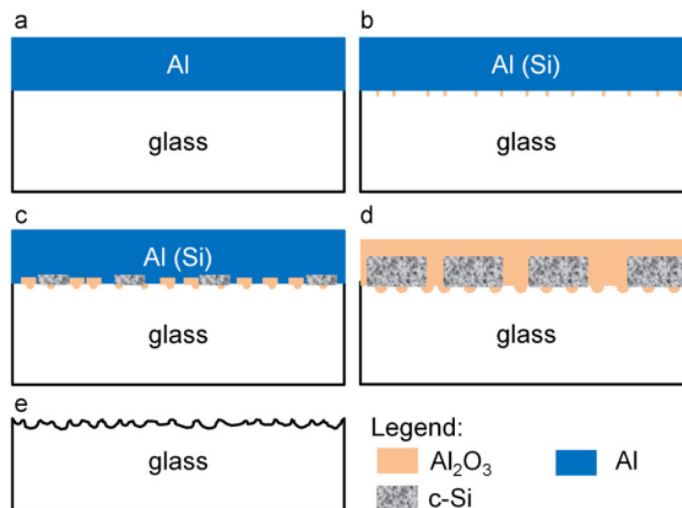
Figure 37. Schematic representation of AIT process flow. (a) Al film coated glass. (b) Early stage of the annealing of the sample. (c) intermediate stage of the annealing. (d) final stage of the annealing and (e) textured glass surface after wet chemical etching [108].

44

2.4.2.2.5.1. Aluminum Film for AIT Process

Aluminum coating on the glass designates the amount of the material joining the redox reaction. To obtain high efficiency on the reaction, the film should be free of impurities, especially oxygen impurity. For this reason, the coating is conducted under high vacuum. The coating method can be thermal evaporation [75], [109], [111], [112] or sputtering [75], [90]–[92], [107]–[109], [115]. Thinner aluminum results with shallower texture, thus week scattering behavior. However, there exists a threshold thickness of Al for texturing. The effect of Al thickness on roughness of the glass can be seen in Figure 38.
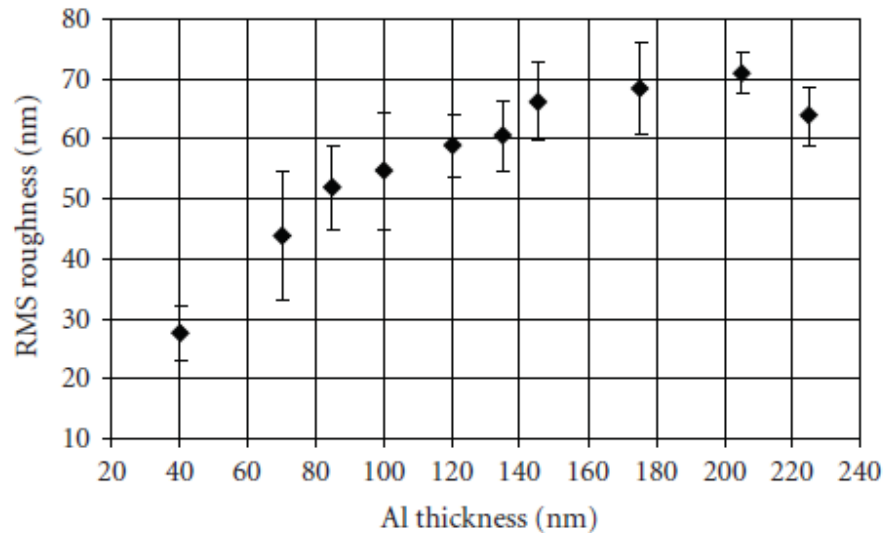
Figure 38. Roughness versus Al thickness graph obtained from AFM measurements for borosilicate glasses annealed at 610 °C for 40 min. and etched by first phosphoric acid for 10 min. and then HF:HNO3 etching for 10 seconds [112].

2.4.2.2.5.2. Annealing in AIT

Annealing is one of the most important steps for the formation of random textures. It is reported that Al diffuses into the glass and forms Al_2O_3. The elemental

Si formed from this reaction diffuses into Al from grain boundaries and interfaces. Then, Si forms in the film [108]. The evolution of the film during annealing is given in Figure 39 for 570 °C annealing temperature. The area numbered as 1 in Figure 39(a) is reported as hillock [108] formed due to the difference in thermal expansion coefficients between glass and Al film [116]. On the other hand, the area 2 in Figure 39(a) is identified as void, where the glass surface is exposed [108]. After one hour of annealing, greenish colored areas that have dendritic form were exposed as shown in Figure 39(b), which is numbered as 3. With increasing of the annealing time, different regions exposed as seen in Figure 39(c). The area 3 is identified as crystalline Si by Raman spectroscopy and XRD measurements as shown in Figure 40.
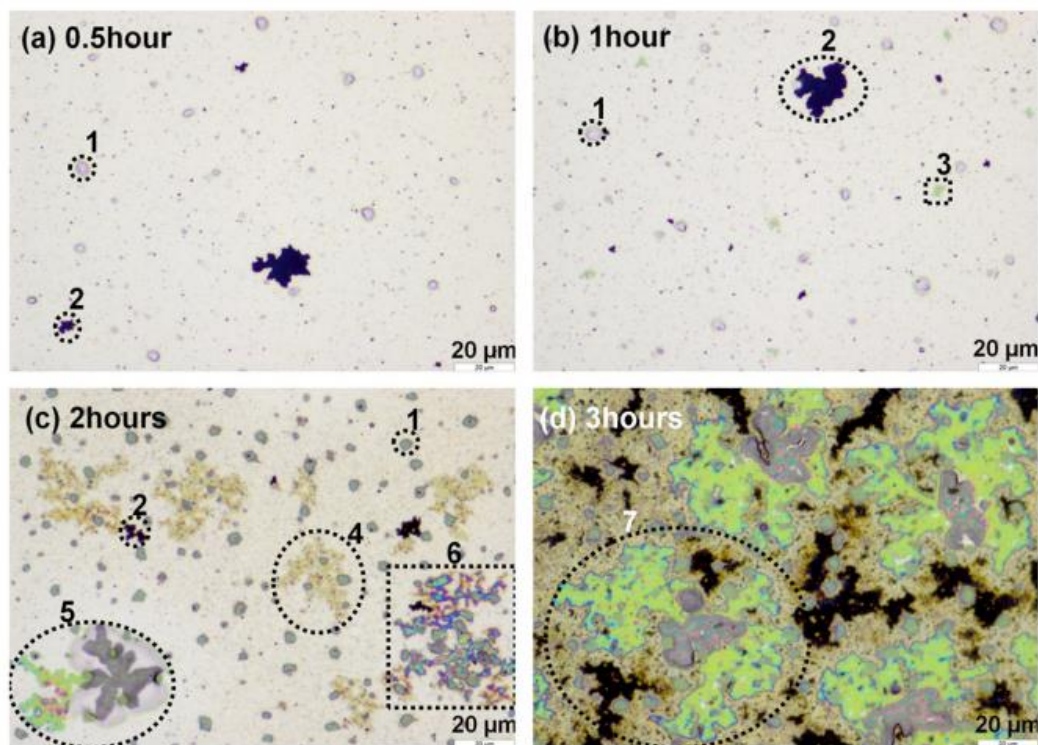
Figure 39. Optical microscope images of annealed samples with different annealing durations. (a) 0.5 hour annealing, (b) 1 hour annealing, (c) 2 hours annealing and (d) 3 hours annealing for annealing temperature of 570 °C [108]**.**
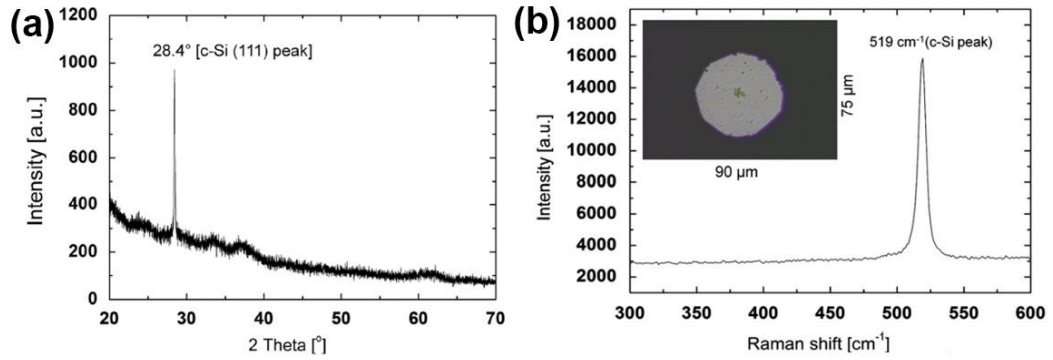
Figure 40. Identification of area 3 in Figure 39(b). (a) XRD measurement and (b) Raman spectroscopy [108]**.**

The formation of Al_2O_3 nodules by diffusion of Al into the glass can be seen in Figure 41(a). Silicon layer, on the other hand, grows laterally on the surface during the annealing as shown in Figure 41(b).
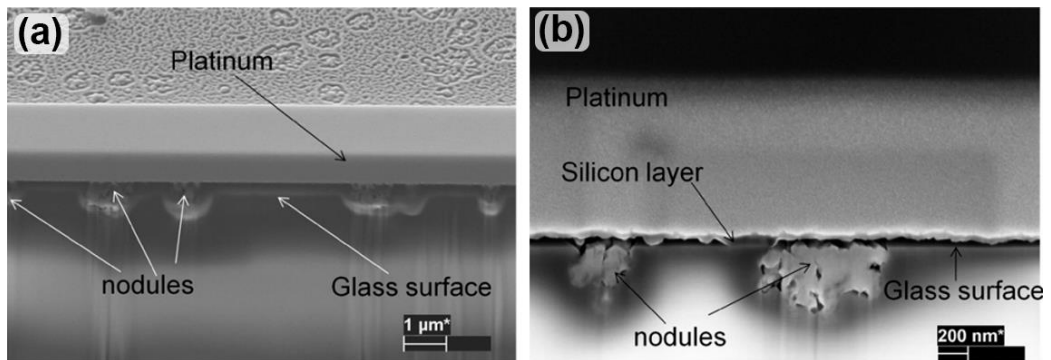
Figure 41. Cross sectional view of annealed for 3 hours at 570 °C. (a) Al_2O_3 nodules in the glass and (b) Si cluster on the surface [108]**.**

The reaction rate changes with the annealing temperature. Thus, to complete the reaction at lower temperatures, higher annealing durations are required. The reaction rate can be extracted by measurement of the amount of c-Si on the surface. In Figure 42(a), the change in the fraction of c-Si at different annealing temperatures is given. Increase in the annealing temperature leads to decrease in the annealing duration. It is seen that at 500 °C, the reaction finished after 12 hours of annealing.
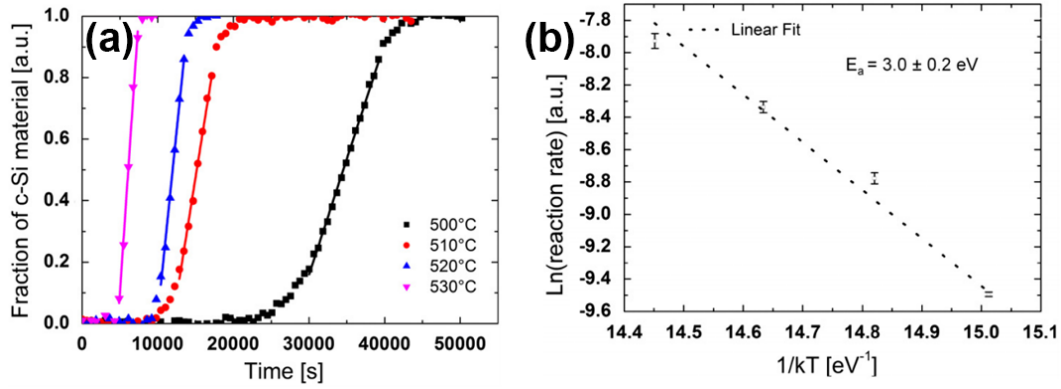
Figure 42. (a) Fraction of c-Si material versus time graph for different annealing temperatures and (b) Arrhenius plot for AIT process based on c-Si growth [108]**.**

The reaction between Al and SiO$_2$ has Arrhenius-type behavior in the temperature range of 200-850 °C as reported [117], [118]. The activation energy can be calculated by Arrhenius equation as given below.

$$Reaction\ Rate = Ae^{\frac{-E_a}{kT}}$$ (Eq. 24)[108]

where A is an arbitrary constant, k is the Boltzman constant, T is the annealing temperature and E$_a$ is the activation energy [108]. From Figure 42(a), reaction rates were extracted and Arrhenius plot is obtained as shown in Figure 42(b). The activation energy is found by Huang et al. as 3.0 ± 0.2 eV [108].

2.4.2.2.5.3. Etching for Textured Surface Reveal

Successful removing of the reaction products from the surface is important. To remove reaction products, 2-step chemical etching can be used [105]. The remaining Al can be removed by 15 minutes hot (110-180 °C [105], [111], [112]) phosphoric acid (H$_3$PO$_4$) etching . As a second step, hydrofluoric acid-nitric acid (HF:HNO$_3$) etching for couple seconds is employed. This solution also removes some portion of the glass. The amount of the HF in the aqueous solution, changes the amount of the

glass removed by HF [105]. As a result, in addition to annealing, exposure time to HF with different concentrations alters the textured surface [62], [109], [119]. The HF:HNO$_3$ ratio can be changed from 1:1 to 1:20 [93], [105]. 1:20 ratio solution results with craters smaller than 1 µm while 1:1 ratio HF:HNO$_3$ etching results with 2-5 µm sized craters [93].

In addition to 2-step etching, there exists various attempts to obtain the textured surface with only 1-step. It is also possible to remove reaction products, including remaining metallic Al, with only HF:HNO$_3$ etching [75], [89]–[91], [113]. There is no reported difference of employment hot phosphoric acid etching prior to HF:HNO$_3$ etching.

There are attempts to remove reaction products with different etching solutions. Potassium permanganate-hydrofluoric acid (KMnO$_4$:HF) solution [109], hydrofluoric acid-nitric acid-acetic acid (HF:HNO$_3$:CH$_3$COOH) solution [109], [110] and sodium hydroxide-hydrofluoric acid (NaOH:HF) solution [110] are used. In HF:HNO$_3$:CH$_3$COOH, acetic acid is used as a buffer layer in order to decrease the reaction rate because the reaction rate of HF:HNO$_3$ is high and the control on the etching process is poor [110]. On the other hand, KMnO$_4$:HF etched glasses exhibit poor light trapping property against conventional etching using HF:HNO$_3$ [109]. Furthermore, the 1-step etching by NaOH:HF solution demonstrates same texturing and light trapping properties as reported by Cui, et al. [110]. In Figure 43, the surface of AIT glasses can be seen for conventional etching by HF:HNO$_3$ and alternative etching by NaOH:HF.
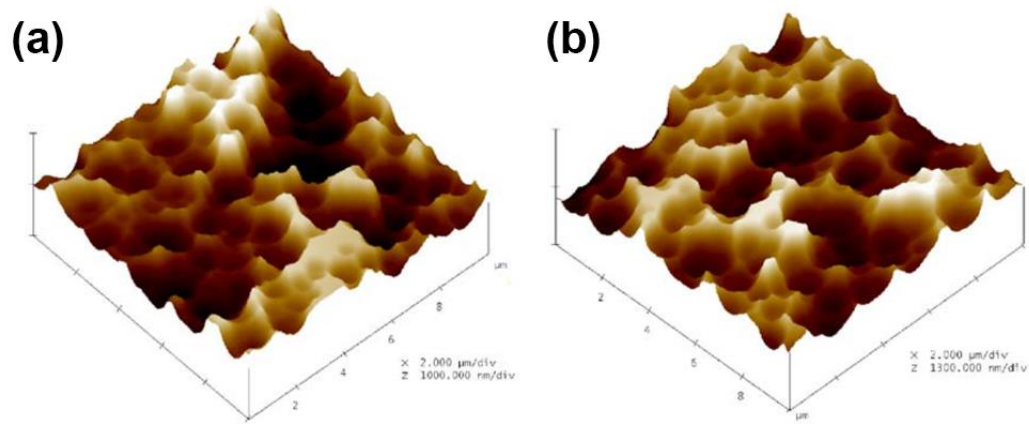
Figure 43. AFM images of AIT borosilicate glass surfaces after (a) conventional HF:HNO₃ etching and (b) NaOH:HF etching [110]**.**

The highest reported haze is around 79% for 400 nm wavelength [91]. In this thesis study, the optimization of AIT parameters for thin film solar cell production and development of an alternative solution to HF-based etching are conducted. In addition, series of experiments were conducted to have deeper understanding on the annealing step because with the absence of the HF, the texture is governed by only the annealing step and understanding the annealing process enables the control of the texture during this process.

CHAPTER III

EXPERIMENTAL PROCEDURES

Optimization of Al thickness used in aluminum induced texturing process alongside with etching duration optimization with conventional etching method are studied in this thesis. In addition to etching optimization with conventional etchants, alternative etchant was developed and new solution is used to produce AIT glasses with superior optical performance. Furthermore, to obtain a better understanding upon the random redox reaction during annealing, the evolution of Al/glass interface is studied, which assists the optimization of the annealing parameter. Additionally, the effects of non-SiO_2 components were studied by changing the glass type and an attempt to produce higher scattering values is made with the combination of macro texture and AIT textures.

3.1. Glasses and Preparation of Glasses

In this thesis, different glasses were used. Optimization of AIT parameters were conducted on soda-lime float glass with 4 mm thickness (manufactured by Türkiye Şişe ve Cam Fabrikaları A.Ş). On the other hand, for the investigation of the effect of non-SiO_2 components on AIT process, different glass types were employed. AIT process is applied on borosilicate glass, alkaline-free glass, fused silica glass and soda-lime glass for this purpose. The composition of each glass is given in Table 2. The fused silica is an amorphous form of the quartz. Alkaline-free glass, furthermore, contains low SiO_2 component.

Table 2. Chemical compositions of different glasses used in this thesis.

Name of Glass / Composition (%)	SiO$_2$	Al$_2$O$_3$	CaO	MgO	B$_2$O$_3$	Na$_2$O
Soda-Lime [120]	72	1	8	4	-	15
Borosilicate [121]	81	2	-	-	13	4
Alkaline-Free [122]	~60	~20	-	-	~10	~10
Fused silica glass [123]	100	-	-	-	-	-

Prior to Al coating, cleaning of the glass surface is important. The contaminants like dust particles can prevent the reaction between Al and the glass, which results with un-even surface texturing. Even tin containing surface is identified by UV light source before the utilization of glasses because tin also hinders the reaction. The samples were cleaned in an ultrasonic cleaner by Alconox, a special laboratory grade detergent, to remove contaminants. Rinsing liquid consists of only 5% detergent in DI water. First, glasses were cleaned by Alconox at 50 °C for 15 minutes, followed by DI water rinsing at 55 °C for 15 minutes to remove detergent residues. Furthermore, cold rinsing (25 °C) in ultrasonic cleaner for 20 minutes was conducted.

3.2. Aluminum Induced Glass Texturing: Optimization of Parameters

The optimization of AIT process has been carried out with separate steps. First of all, Al thickness and etching optimization studies have been conducted. Due to the fact that several samples can be produced on one Al coating process, etching optimization has merged with Al thickness optimization. For this study, the annealing conditions has been set to 600 °C temperature and 1 hour annealing duration. After optimization of Al thickness and etching process, a new solution optimization study has carried out on the pursuit of HF-free solution. Finally, annealing optimization has been conducted and detailed investigation of reaction mechanisms has been carried out.

3.2.1. Al Coating by Thermal Evaporation

For Al coating on glass samples has been developed in GUNAM facilities in Physics building. The thermal evaporation system is used for this purpose since Al coating should be conducted under vacuum to prevent oxidation of Al during deposition process, which is set 3×10^{-5} torr. It is also possible to coat Al with magnetron sputtering method, which was not employed in this thesis. Schematic diagram of the Al coating system has been given in Figure 44. Various thicknesses have been used for optimization of Al thickness. Al thicknesses that were coated by thermal evaporation are given in Table 3, which were measured by thickness monitor build in the evaporation system and confirmed by Veeco Dektak 6M Stylus Surface Profilometer.
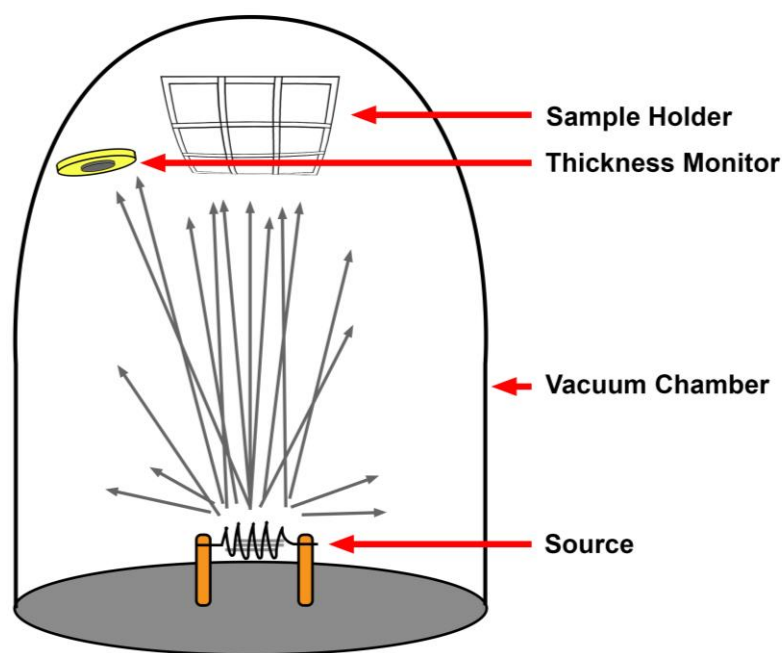
Figure 44. Schematic representation of thermal evaporation system in GUNAM

Table 3. Al thicknesses coated on glass surfaces on thermal evaporation system with sample names.

Sample Set	Al thickness (nm)
M8	100
M6	120
M5	130
M9	140
M7	150
M3	160
M4	350

Samples were annealed in the tube furnace at 600 °C for 1 hour under N_2 flow. Then, etching process has been conducted. For the optimization of etching process, 3 or 4 samples were produced at the same time on the thermal evaporation system.

3.2.2. Etching Optimization

3.2.2.1. Conventional Etching Process

Optimization of conventional etching process has been conducted for each Al thicknesses because each thickness results with different amounts of reaction products, which naturally changes the optimum etching time. The 2-step etching for AIT has been adapted in GUNAM. First step of etching was done by hot (130 °C) phosphoric acid (H_3PO_4) for 15 minutes. Then, $HF:HNO_3$ 1:1 volume ratio solution at room temperature was employed for final etching step. The etching time for each thickness changes from 10 to 25 seconds. Optimization of etching time has been summarized in Table 4 for each Al thickness. Sample naming was remade for better understanding of the analysis and comparison.

Table 4. Etching optimization for various Al thicknesses

Sample Set	Sample Name	Al Thickness (nm)	Etching Time (s)
	AIT_100nm_10sec	100	10
M8	AIT_100nm_15sec	100	15
	AIT_100nm_20sec	100	20
	AIT_120nm_15sec	120	15
M6	AIT_120nm_20sec	120	20
	AIT_120nm_25sec	120	25
	AIT_130nm_10sec	130	10
	AIT_130nm_15sec	130	15
M5	AIT_130nm_20sec	130	20
	AIT_130nm_25sec	130	25
	AIT_150nm_15sec	150	15
M7	AIT_150nm_20sec	150	20
	AIT_150nm_25sec	150	25
	AIT_160nm_15sec	160	15
M3	AIT_160nm_20sec	160	20
	AIT_160nm_25sec	160	25
	AIT_350nm_15sec	350	15
M4	AIT_350nm_20sec	350	20
	AIT_350nm_25sec	350	25

Produced samples were characterized by integrated sphere spectrometer having an 8-inch, 5-port integrating sphere (Oriel 70679NS) on standard configuration for optical characterization. Morphological characterization, on the other hand, was conducted by Nanomagetic Instruments atomic force microscope.

3.2.2.2. HF-free Solution Optimization

As an HF-free solution, $NaOH:H_2O_2:H_2O$ solution, was used. H_2O_2 acts as a buffer in the solution and NaOH removes the reaction products from the glass surface without altering the texture. First trials have conducted on a set of samples given in Table 5. 1:20:60 ratio of $NaOH:H_2O_2:H_2O$ at 75 °C was set as a base of this optimization process, which was used to etch Sample 1. For each sample, a different parameter was changed and results were compared each other by QUANTA 400F field emission scanning electron microscope (FE-SEM) and integrated sphere spectrometer on standard configuration.

Table 5. Produced sample parameters for HF-free solution optimization

Sample Name	Aluminum thickness	Annealing time & temperature	Etchant ratio	Etching time
1	150 nm	600 °C for 1 h	1:20:60	4 h
2	150 nm	600 °C for 1 h	1:20:60	8 h
3	150 nm	600 °C for 1 h	1:40:120	4 h
4	150 nm	600 °C for 1 h	1:20:100	4 h
5	150 nm	600 °C for 2 h	1:20:60	4 h
6	220 nm	600 °C for 1 h	1:20:60	4 h

Due to the fact that the etching time with HF-free solution is a disadvantage for these etchant ratios, the concentration of NaOH in the solution has been increased and the evolution of the surface with increasing etching time has been investigated. The concentration was kept constant as 1:2:6 in this trial in this study. Samples were coated with 150 nm Al and annealed at 600 °C for 1 hour in N_2 ambient. These samples, then, were etched for different durations as summarized in Table 6. The sample set was characterized by QUANTA 400F field emission scanning electron microscope (FE-SEM).

Table 6. Production parameters of sample set for etching time (min.) optimization with HF-free solution

Sample Name	N1	N2	N3	N4	N5	N6	N7	N8	N9	N10	N11	N12
Etching Time (min.)	10	20	30	40	50	60	70	80	90	100	110	120

3.2.2.3. Conventional Etchant and HF-free Etchant Comparison Study

For the comparison of HF-free solution with conventional etching solution, a sample set was prepared and 6 Al coated sample has produced. The Al thickness was set to 150 nm. These samples were annealed at 550 °C for 12 hours in tube furnace under N_2 flow. This annealing condition is chosen according to annealing optimization studies, which will be described in the section, 3.2.3. Annealing Optimization. Then, 3 sample has been used for conventional etching. The rest of the samples were used for HF-free etching. The further detail about process parameters are given in Table 7.

Table 7. Process parameters for samples produced to compare HF-free solution with conventional solution

	Conventional Etching			HF-free Etching	
Sample Name	H_3PO_4 *130 °C*	HF:HNO$_3$ *1:1 ratio*		**Sample Name**	NaOH:H_2O_2:H_2O *1:2:6 ratio in US cleaner*
HF_15	15 min	15 sec.		**NaOH_0.5**	0.5 hour
HF_30	15 min	30 sec.		**NaOH_1**	1 hour
HF_60	15 min	90 sec.		**NaOH_3**	3 hours

These samples were characterized by integrated sphere spectrometer having an 8-inch, 5-port integrating sphere (Oriel 70679NS) on reverse configuration for optical

characterization. In addition, structural and morphological analysis was conducted by SEM (Zeiss EVO HD) and atomic force microscope (Veeco diMultiMode V) using a ATEC-NC-20 tip in tapping mode.

3.2.3. Annealing Optimization

The optimization of the annealing was conducted with a classical tube furnace (10 cm diameter) under 4 slm N_2 flow. The schematic of the furnace is given in Figure 45. 2 samples can be annealed at a time due to space limitation on the quartz boat.

The annealing optimization was started by changing annealing ambient. Samples were annealed under N_2 flow and atmosphere, then surfaces were investigated by QUANTA 400F field emission scanning electron microscope (FE-SEM). For this purpose, 150 nm Al coated samples were annealed under different ambient with 1 hour annealing duration and 600 °C annealing temperature. The samples are given in Table 8 with relative production parameters.
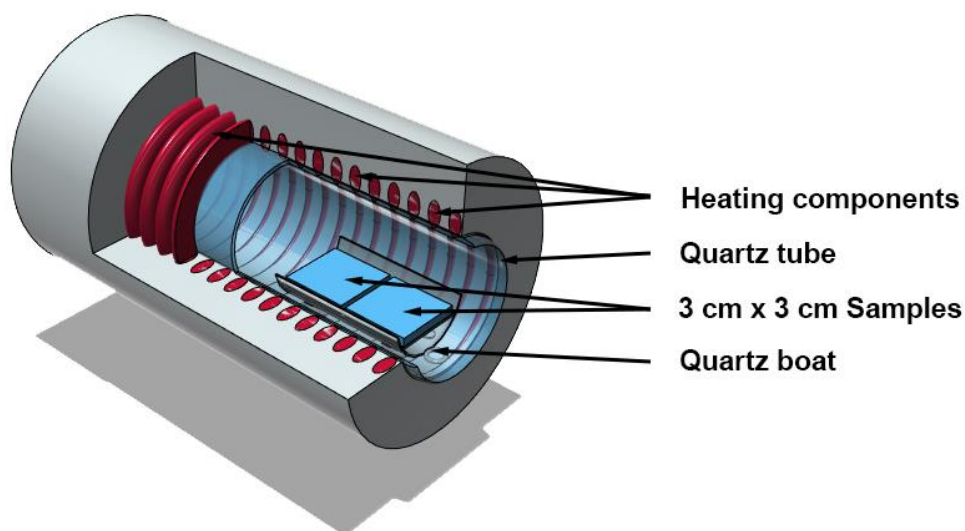
Figure 45. Cross-sectional view of the tube furnace

Table 8. Study conducted for the optimization annealing ambient.

Sample Name	Aluminum Thickness (nm)	Annealing time under 600 °C
A150_N2	150	1 h in N_2
A150_AIR	150	1 h in atmosphere

In addition, to have 3-dimentional information from annealed samples, a new set has been produced to be used for depth profiling by X-Ray Photoelectron Spectroscopy. For the survey scan, 350 nm Al coated samples were used. On the other hand, for detailed scans, 130 nm Al coated samples were chosen. These samples were annealed at 600 °C for 1 hour prior to characterization. Table 9 summarizes the samples with different annealing durations, produced for XPS investigation.

Table 9. Samples prepared for XPS study

Sample Name	X-0	X-5	X-7	X-10	X-15	X-20	X-40	X-60
Annealing Duration (min.)	No annealing (Ref)	5	7	10	15	20	40	60

The morphology of the samples was investigated by optical microscope (Nade metallurgical microscope - NMM-800TRF). The structural and compositional distribution was studied with PHI Versaprobe 5000 Scanning X-Ray Photoelectron Spectrometer (XPS) with Al Kα as a X-ray source by depth profiling. 24.9 W X-ray power used for analysis with 100 μm X-ray spot size and 45° take-off angle. For each region, 58.70 eV pass energy used for high resolution regional scan. Each layer was removed by Ar ion bombardment at 3 kV energy and 3 min dwell time. C1s peak is pinned to 283 eV for survey scans. In addition, survey scan of annealed samples was obtained after Ar ion bombardment for 5 times to reduce the contribution of surface oxides. The binding energy shifts related to surface charging during data collection was corrected using SiO_2 or Al peak positions, where applicable.

Then, for the pursuit of the understanding the annealing mechanism, different samples were produced. First of all, varying annealing temperatures with different durations were used to anneal 150 nm Al coated samples. Samples, for this set of sample, were named according to their annealing temperature and duration. For example, sample 550_060 was annealed at 550 °C for 60 minutes. The samples produced for this study are given in Table 10. These samples, then, were etched by HF-free solution as optimized in the section, 3.2.2.2. HF-free Solution Optimization. The evolution of the film and the effect of the annealing conditions on the optical properties of the samples were investigated.

Table 10. Samples produced for the optimization of annealing conditions

550 °C			575 °C		600 °C		
550_005	550_015	550_060	575_015	575_030	600_005	600_010	600_011
550_090	550_105	550_120	575_045	575_060	600_012	600_013	600_020
550_150	550_180	550_300	575_075	575_090	600_030	600_040	600_050
550_600	550_1020		575_105		600_060		

Structural, morphological, and optical characterization of the samples were made before and after etching. The morphology and the elemental distribution of the annealed film was investigated by an optical microscope (Nade metallurgical microscope - NMM-800TRF) and a QUANTA 400F field emission scanning electron microscope (FE-SEM) coupled with an Ametek EDAX energy dispersive X-ray spectroscope (EDX). The structural and compositional evolution of the over-layer was studied by Raman spectroscope (Horiba 800 Jobin Yvon). Selected EDX images were processed using Adobe Photoshop CC 2015. After texturing of samples, optical measurements were conducted with an 8-inch, 5-port integrating sphere (Oriel 70679NS) and topographical characterization with SEM (Zeiss EVO HD) and atomic force microscope (Veeco diMultiMode V) using a ATEC-NC-20 tip in tapping mode. 2D FFT images were obtained from AFM data using image analyses software Gwydion version 2.44.

3.2.3. The Effect of Glass Type

The AIT process was optimized for one glass type that is soda-lime glass. Due to fact that the random redox reaction between Al and SiO_2 is the base of this process, the amount of available SiO_2 should affect the resultant texture. That is the reason behind why the glass should be count as a parameter of AIT process even though it is not considered as in the literature. Different glasses were employed to investigate the effect of glass. Soda-lime glass, borosilicate glass, alkaline-free glass and fused silica glass were used for the investigation. The components of each glass are given in Table 2 in the section, 3.1. Glasses and Preparation of Glasses. 150 nm of Al were coated on each glass by thermal evaporation at 3×10^{-5} torr. Then, samples were annealed at 600 °C for 1 hour under N_2 flow. Finally, reaction products were removed by first using hot (130 °C) hot phosphoric acid (H_3PO_4) for 15 minutes and then 1:1 $HF:HNO_3$ solution for 15 seconds, except for the fused silica glass sample, which had to be kept in the 1:1 $HF:HNO_3$ solution for 35 seconds for full removal of the reaction products. The textured glass samples were optically characterized by 8-inch, 5-port integrating sphere (Oriel 70679NS) optically. Surface characterization is made by Atomic Force Microscope, AFM (Nanomagnetic Instruments, Ambient AFM/MFM) in tap-ping mode and Zeiss EVO HD SEM.

3.2.4. Combination of Macro and Micro/Nano Texture

In addition to flat surfaces used for AIT process, there exist attempts to make more effective light trapping interfaces with the combination of macro sized surface structures with micro or nano sized texture. The micro and nano sized textures were produced by using AIT method. HF-based conventional solution was used for the former and HF-free solution was employed for the latter. The macro-textured glasses are readily available in the market. These glasses are soda-lime glass having 4 mm thickness with low iron content. The periodically macro textured sample have inverted pyramid structure that is produced by glass casting operations. On the other hand,

randomly macro textured sample was produced by sandblasting method. SEM image and 2D surface profile obtained by Veeco Dektak 6M Stylus Surface Profilometer for each macro textured glass are given in Figure 46.
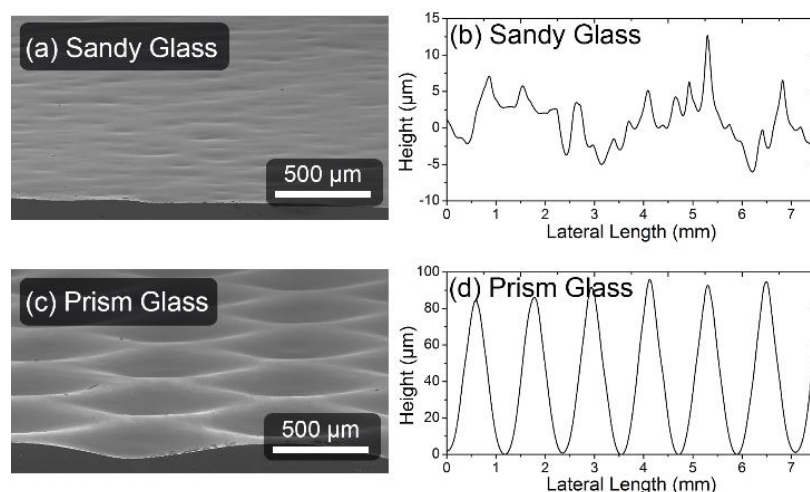
Figure 46. Sandy glass: (a) cross-sectional SEM image, (b) Dektak surface profile; and prism glass: (c) cross-sectional SEM image and (d) Dektak surface profile

The samples were coated with 150 nm Al and annealed at 550 °C for 10 hours. For each macro textured glass type, micro and nano sized texture production has conducted. The summary of processing parameters and naming of the sample is given in Table 11. For comparison, float soda-lime glass was textured with same parameters.

Table 11. Process parameters of macro textured glasses

Sample Name	Coating	Annealing	Etching
Float_Ref	-	-	-
Float_Acidic	150 nm Al	550 °C for 10h	H_3PO_4 & HF:HNO_3
Float_Basic	150 nm Al	550 °C for 10h	NaOH solution
Sandy_Ref	-	-	-
Sandy_Acidic	150 nm Al	550 °C for 10h	H_3PO_4 & HF:HNO_3
Sandy_Basic	150 nm Al	550 °C for 10h	NaOH solution
Prism_Ref	-	-	-
Prism_Acidic	150 nm Al	550 °C for 10h	H_3PO_4 & HF:HNO_3
Prism_Basic	150 nm Al	550 °C for 10h	NaOH solution

3.3. a-Si:H Thin Film and Solar Cell Production

The effect of the textured surface on the performance of thin film solar cells has been studied in this section. Thin films were deposited by plasma enhanced chemical vapor deposition (PECVD) system in GÜNAM. For samples AIT_130nm_20sec, AIT_130nm_25sec and AIT_350nm_25sec, 300 nm a-Si:H thin film was deposited. After absorption measurements, Al contacts were deposited for external quantum efficiency measurements. The structure is given in Figure 47.
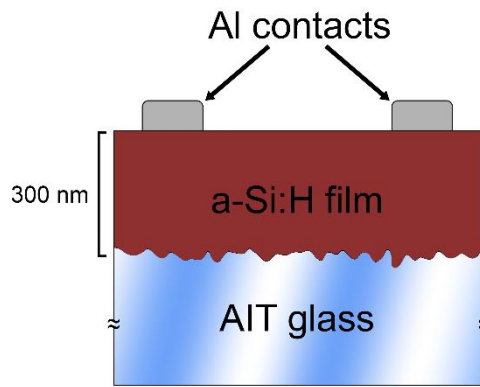
Figure 47. Mesh structure of a-Si:H coated samples prepared to

Additionally, a-Si:H solar cell with p-i-n structure has been deposited on textured float, sandy and prism glasses to observe the effect of AIT texture on the efficiency of solar cell. The structure is shown in Figure 48. 1 µm AZO was deposited on textured glass. Then, 25 nm p-type, 300 nm intrinsic and 30 nm n-type a-Si:H layers were deposited with PECVD system. For measurements, 300 nm Ag contacts were thermally evaporated.
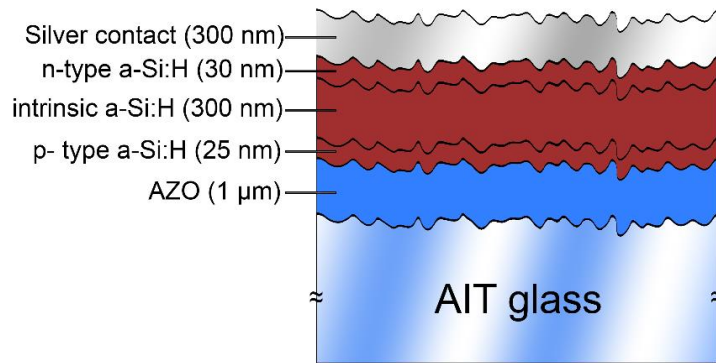
Figure 48. a-Si:H solar cell structure deposited on AIT glass

3.4. Characterization

For the characterization of samples, different instruments and setups have been employed. Optical characterizations such as reflection, transmission and diffuse transmission of the samples have conducted in Integrated Sphere Spectrometer (ISS), which is present in GUNAM. For the surface characterization, Atomic Force Microscope (AFM) in GUNAM and in Central Laboratory of METU were used. In addition, Secondary Electron Microscope (SEM) in Central Laboratory of METU and in GUNAM were employed for further surface investigation. The characterization of annealed samples were carried out by X-Ray Diffraction (XRD), Raman Spectrometer, Electron Dispersive X-Ray Spectroscopy (EDX) and X-Ray Photoelectron Spectroscopy (XPS) present in GUNAM and Central Laboratory of METU.

3.4.1. Integrated Sphere Spectrometer

Integrated sphere spectrometer employs a sphere which distributes the light, which is reflected or transmitted from the sample, inside of the sphere and only a fraction of the light is sent to the monochromator. An 8-inch, 5-port integrating sphere (Oriel 70679NS), Newport Monochromator 74100 and Stanford Research Systems SR830 DSP Lock-in Amplifier were employed in this setup. The schematic

representation of the reflection measurement setup is given in Figure 49. The light produced by halogen lamp is sent through a convex lens which focuses the light, a diaphragm that eliminates un-focused light at the focal point of the convex lens, a chopper that shapes the light as a signal with a frequency of 225 Hz and another convex lens which sends light to the infinity. Each wavelength is read out by Si detector from monochromator and signal sent to lock-in amplifier, which processes the signal having same frequency as chopper, thus reducing the noise in the measurement.
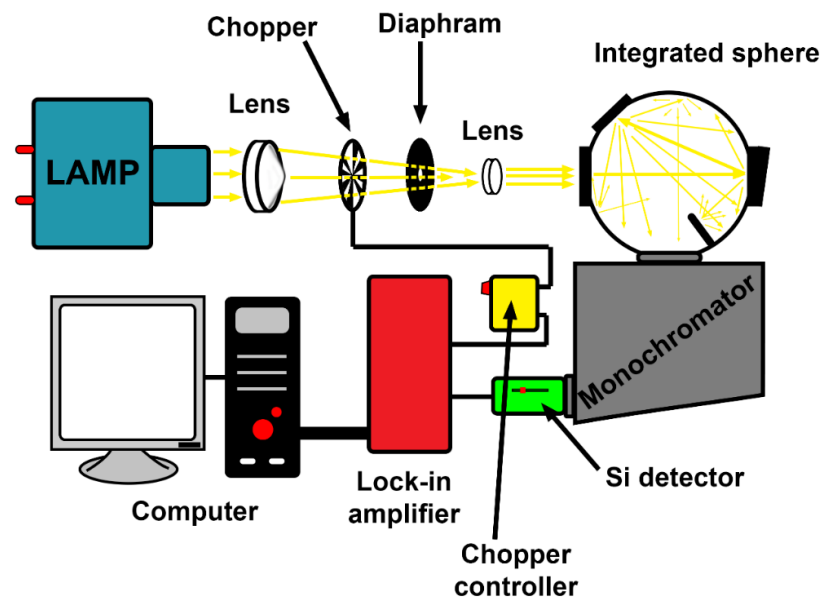
Figure 49. Schematic representation of reflection measurement in the integrated sphere spectrometer.

There are two ways to measure transmission and reflection in this set-up. The sphere, which has interior surface coating of $BaSO_4$, have 5 ports. 4 of these ports of the sphere are given in Figure 50 with buffer. The fifth port is at the top of the sphere used for alignment. In the configuration given at Figure 50(a), the light entering port is named as transmission port. The port where light exits from the sphere is named as reflection port. Reflection port, in addition, have 8-degree angle to make the reflected light do not exit from transmission port. However, for diffuse reflection measurements, a port is present at the second reflection point where direct reflection can be taken out

from the sphere and scattered light can be measured, which is shown as port 3 in Figure 50(a). For measurement, light is taken out from port 4, which is also called as measurement port. Transmission measurements are conducted with closed reflection and diffuse reflection ports and sample is placed at transmission port. For diffuse transmission measurement, reflection port is kept open and direct transmission can be taken out while diffuse transmitted light kept inside the sphere. Reflection measurement, furthermore, is done by placing the sample at reflection port while diffuse transmission port is closed. Between reflection port and measurement port, a buffer prevents direct reflection to the monochromator.
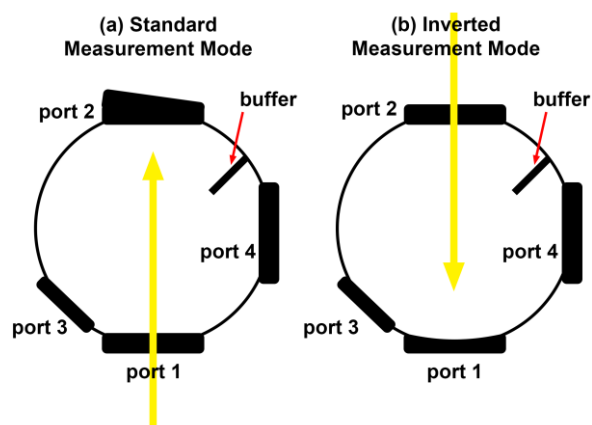
Figure 50. Ports of sphere as seen from the top. The top of the sphere has observation port that is used for alignment

For accurate measurements, the light distribution in the sphere should be uniform. However, for high scattering angles in transmission measurements, the uniformity on the sphere surface is disturbed and the total intensity is reduced because there is no blocking mechanism between transmission port and monochromator port. For this reason, in HF-free solution studies, where haze is higher than the conventional solutions, the set-up was modified. While the reflection measurements are taken with standard measurement mode, transmission and diffuse transmission were measured on inverted measurement mode. Light is sent from reflection port and this port is used as

transmission port. In this inverted configuration, the buffer prevents direct shining on the measurement port. As a result, more accurate measurements can be obtained.

The absorption of the sample can be calculated by subtraction of reflection and transmission from 1 if the sample is transparent or semi-transparent. However, if the sample do not transmit of the light, the absorption can be found by 1-R.

3.4.2. External Quantum Efficiency Setup

The external quantum efficiency (EQE) is another technique used for the characterization of solar cells. In this technique, number of electrons generated per photon is measured. Figure 51 shows the setup used to characterize a-Si:H thin film and solar cells. The components of the setup is similar with optical measurement setup with the exception of integrating sphere. In this configuration, light interacts with the sample after passing through the monochromator. Spectral response can be extracted from EQE measurements by the given formula in Eq. 25.
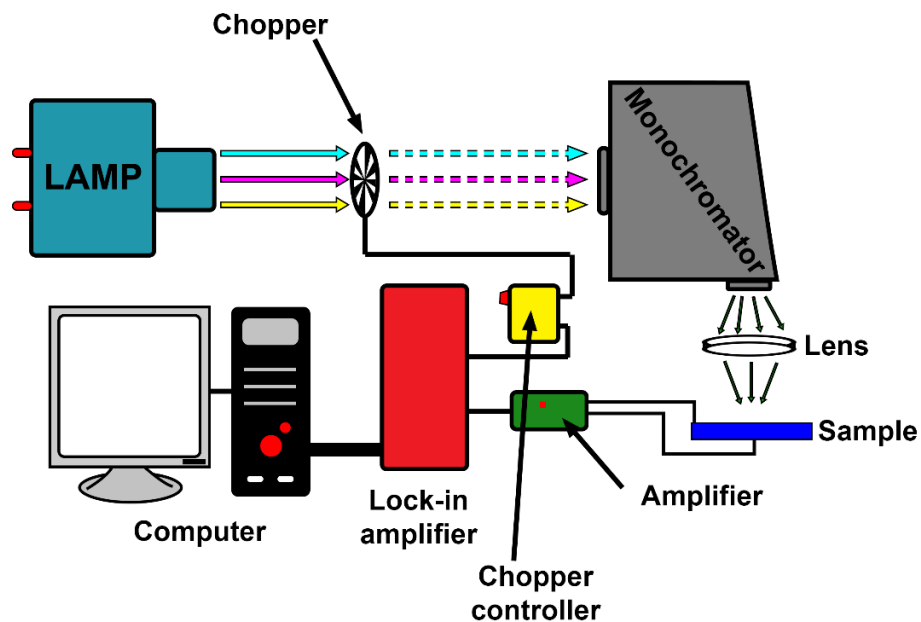
Figure 51. Schematic of external quantum efficiency setup in GUNAM.

67

$$SR = \frac{q\lambda}{hc} QE \qquad\qquad\qquad \text{(Eq. 25)}^{[124]}$$

3.4.3. I-V Measurement

I-V measurement is one of the basic characterization methods used for solar cells. Newport Solar simulator was used for the characterization of a-Si:H thin film solar cells. The schematic representation of the system is given in Figure 52. The measurements were conducted under 1 SUN AM 1.5G illumination. From I-V measurements, cell parameters such as fill factor, open circuit voltage, short circuit current, series resistance, shunt resistance, etc. can be found.
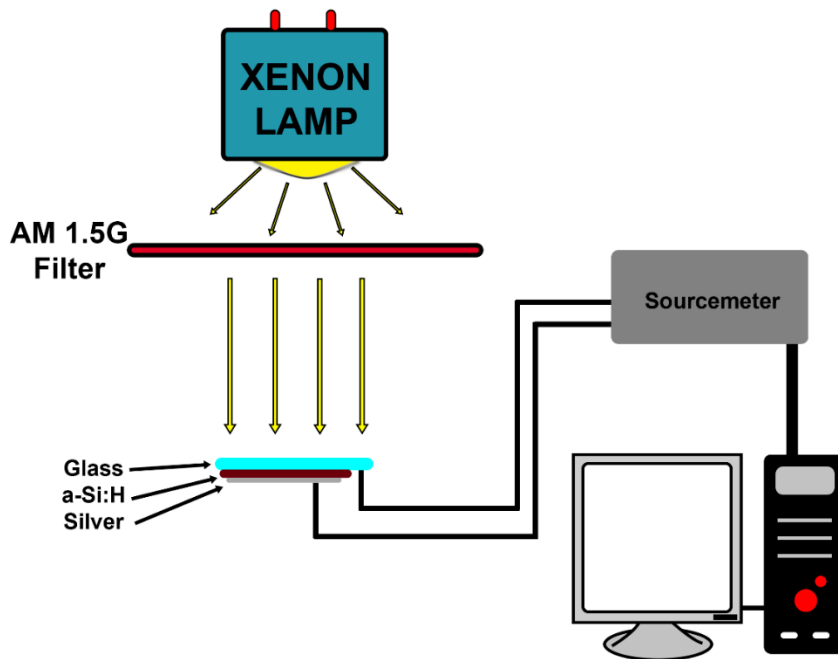
Figure 52. Schematic of solar simulator in GUNAM

3.4.3. Atomic Force Microscope

Atomic force microscope (AFM) is employed for 3 dimensional analysis of the surface. AFM scans the surface with a sharp tip on a cantilever as shown in Figure 53(a). A laser beam reflected from the surface of the cantilever to a 4-quadrant detector detects the movement of the tip. Then, according to data coming from the 1-quadrant detector, the surface profile is generated on a computer screen. For an AFM measurement, the tip should be close or even touch to the surface [Figure 53(b)].
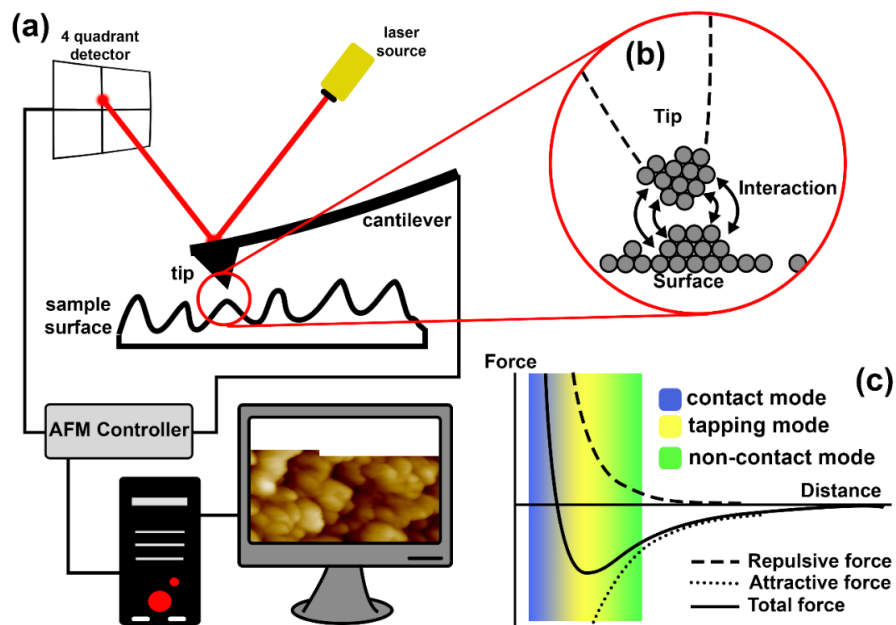
Figure 53. (a) Schematic representation of a measurement by AFM, (b) tip-sample interaction and (c) force versus distance graph showing atomic forces and operation modes of AFM

There are 3 main different measurement modes in the AFM. The measurement can be done by directly touching the surface, which is called as contact mode. In this measurement mode, laser beam detects the change in the position of the tip. This mode is used for solid material measurement and tip can damage the surface. If there is no physical contact, the tip is oscillated in a positon that interaction between surface atoms and tip is still possible. According to the distance to the sample, the oscillation

frequency of the cantilever changes. By laser beam, this change in the frequency is detected and measurement conducted. This measurement mode is usually employed for biological measurements. In addition to these modes, tapping mode is also available, in which the cantilever taps on the surface with a certain frequency. The change in the tapping frequency is detected and surface is reconstructed on a computer. Operation modes with applicable distances are given in Figure 53(c).

The obtained raw data was analyzed with Gywidion 2.44. By using this analyzing program, 2D and 3D surface profiles were obtained. Apart from surface profiling, it is possible to obtain the roughness (σ) that is part of a surface texture of the scanned surface. σ_a (arithmetic mean height) shows the height difference of each point to the arithmetical mean of the surface whereas σ_{rms} gives the root-mean-square average of height distribution from the mean line. In this thesis, σ_{rms} is used for roughness measurements.

In this thesis, Veeco diMultiMode V using a ATEC-NC-20 tip in tapping mode was employed for AFM measurements.

3.4.4. Scanning Electron Microscope

The scanning electron microscope (SEM) is generally employed for detailed examination of the surface. A monochromatic beam of an accelerated electron is sent to the sample and secondary electrons are collected. This beam scans the surface and surface is constructed. SEM does not give height information. However, some rough ideas can be obtained by tilted measurements. In addition to secondary electrons, Auger electron, back scattering electrons and X-rays can be generated during the measurement and different characterization methods can be employed in SEM setup.

In this thesis, QUANTA 400F field emission scanning electron microscope (FE-SEM) and Zeiss EVO HD scanning electron microscope (SEM) were used.

70

3.4.5. Energy Dispersive X-Ray Spectroscopy

Energy Dispersive X-Ray Spectroscopy (EDX) is a measurement mode of the SEM. EDX gives the opportunity to identify and roughly quantify the each material in the sample. When electron beam heats an atom in the sample, an electron from core shells can be emitted. Following this emission, an electron from higher shells relaxes to empty state and emits an X-ray. Due to the fact that energy differences between orbitals are identical to each atom, analyzing the energy of the emitted X-ray can be used to identify the material. According to the strength of the signal for a specific energy, a quantification can be made. For material distribution analysis, this method is employed. For EDX measurements, Ametek EDAX energy dispersive X-ray spectroscope was employed coupled with FE-SEM.

3.4.6. X-Ray Photoelectron Spectroscopy

X-Ray Photoelectron Spectroscopy (XPS) gives same information as EDX but with higher precision. In this measurement method, monochromatic beam of X-ray is send to the sample. X-ray causes emission of an electron from the core shell levels of the atom. The electron emitted from the sample passes from a magnetic field. According to the strength of the magnetic field, electrons that have different kinetic energies can be sent to the detector separately. Then, composition of the material can be identified. In addition to composition, chemical states can be obtained from this measurement because each bond formation between atoms changes the bounding energy of electrons that are present in the core shells, thus, kinetic energy of emitted electrons by X-ray bombardment changes. By Ar bombardment, it is also possible to obtain data from deeper layers and making depth profile.

PHI Versaprobe 5000 Scanning X-Ray Photoelectron Spectrometer (XPS) with Al Kα as a X-ray source was used for characterization. 24.9 W X-ray power used for analysis with 100 μm X-ray spot size and 45° take-off angle. For each region, 58.70 eV pass energy was used for high resolution regional scan. Each layer was removed

by Ar ion bombardment at 3 kV energy and 3 min dwell time. C1s peak was pinned to 283 eV for survey scans. In addition, survey scan of annealed samples were obtained after Ar ion bombardment for 5 times to reduce the contribution of surface oxides. The binding energy shifts related to surface charging during data collection was corrected using SiO_2 or Al peak positions, where applicable.

3.4.7. X-Ray Diffraction

X-Ray Diffraction (XRD) is used to identify the crystal parameters alongside with the crystalline material. This method relays on diffraction of X-ray beam from the crystalline material. According to the orientation of the crystal, crystal parameter d, and material, constructive interference occurs for specific angles. The obtained diffraction patterns can be used to obtain the orientation, lattice constant of the crystal and the material information. Even though the measurement setup identifies each peak by its database, it is also possible to make identification and of each crystal parameter by hand. XRD measurements usually conducted with powder samples, which is called as powder diffraction method. In addition, single crystal measurements are also possible but it needs specific XRD setups. In this thesis, Rigaku Miniflex XRD system equipped with Cu Kα radiation source was employed.

3.4.8. Raman Spectroscopy

Raman spectroscopy is another method used for identification of vibrational modes in the sample. In this thesis, Horiba iHR550 Jobin Yvon Raman Spectrometer was used. When light interacts with a material, it is either transmitted, reflected or scattered. In the scattered light, less than 1% of the light have different frequency than the frequency of the initial light. This portion has made inelastic collision and the frequency difference between this 1% portion and the rest determines the material

properties. In this thesis, it is used to determine the form of the elemental Si formed during annealing as in XRD measurements.

CHAPTER IV

RESULTS AND DISCUSSION

4.1. Al Thickness and Etching Optimization for Commercial Recipe

Al thickness and etching time by conventional etchants were investigated together because the amount of Al affects the optimum etching time. Different Al thicknesses were used for optimization. In this section, the results of using different thicknesses and etching durations are given. In addition, optical comparison between different thicknesses for same the etching time was made with corresponding AFM images.

4.1.1. 100 nm Al Coated Samples

For 100 nm of Al thickness, 3 samples were prepared by $HF:HNO_3$ with etching times of 10, 15 and 20 seconds. When surface morphology was investigated by AFM, whose 3D and 2D images are presented in Figure 54, roughness values for each sample are observed as following: 82 nm for AIT_100nm_10sec, 98 nm for AIT_100nm_15sec and 78 nm for AIT_100nm_20sec. It is seen that roughness was increased when etching time was increased from 10 to 15 seconds. However, the roughness decreased when the etching time was increased to 20 seconds. In addition, rather smooth surface is obtained for 20 sec. etched sample as seen in Figure 54(c). Furthermore, optically, there is no significant change in the transmittance of samples as presented in Figure 55(a). The average haze for 400 nm wavelength is around 27%

as seen in Figure 55(b). With the increase of the wavelength, the haze decreases for all sample. AIT_100nm_10sec and AIT_100nm_15sec shows the same trend but AIT_100nm_20sec have higher haze at longer wavelengths. The difference in the haze for longer wavelengths can be attributed to the crater sizes. It is known that HF smoothens the rough glass surfaces as it is discussed in the section 2.4.2.2.5.3. Etching for Textured Surface Reveal. Increasing the etching time results with enlargement of small craters, thus, the roughness decreases. Bigger craters, in addition, exhibits higher scattering behavior for longer wavelengths.
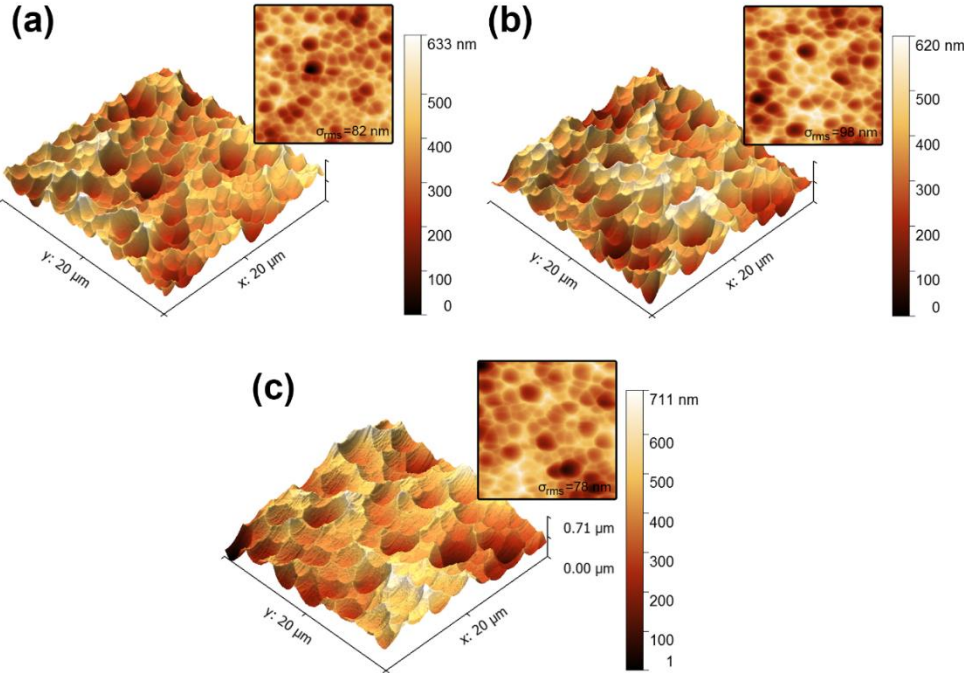
Figure 54. 20 µm x 20 µm AFM images of AIT samples: (a) AIT_100nm_10sec, (b) AIT_100nm_15sec and (c) AIT_100nm_20sec.
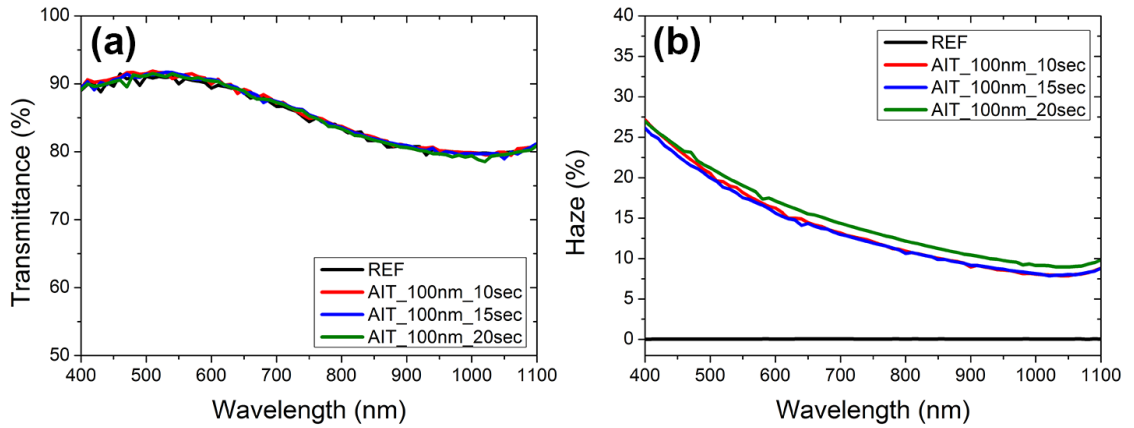
Figure 55. (a) Transmittance and (b) haze of 100 nm Al used samples

4.1.2. 120 nm Al Coated Samples

For the 120 nm Al thickness, 3 samples were prepared with etching times of 15, 20 and 25 seconds by HF:HNO$_3$. From AFM images presented in Figure 56, it can be seen that crater size is smaller for AIT_120nm_15sec. With the increase of the etching time, crater size also increases for AIT_120nm_20sec and AIT_120nm_25sec. Roughness values are also observed to increase when the etching time is increased to 20 sec. from 82 nm to 129 nm. However, further increase in the etching time resulted in a decrease in the roughness to 107 nm. The effect of this change can be seen from optical measurement results as given in Figure 57. In this sample set, no change in the transmittance is observed. In addition, increase in the etching time results in decrease in the haze of the samples as shown in Figure 57(b). 15 sec. etched sample have 25% haze for 400 nm wavelength of the light. At 20 seconds etched sample, this value drops to 21% and for 25 seconds, it decreases to 19%. With the increase of the wavelength, decrease in the haze is observed with same trend as in the samples coated with 100 nm Al. Increase in the etching time results with decrease in the scattering behavior of AIT glasses.
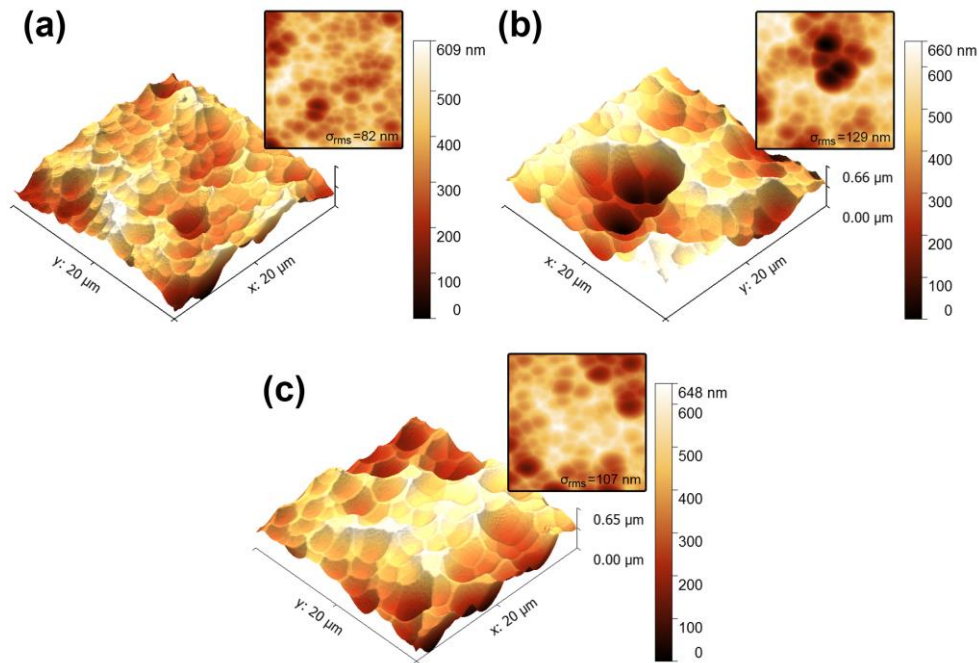
Figure 56. 20 µm x 20 µm AFM images of AIT samples: (a) AIT_120nm_15sec, (b) AIT_120nm_20sec and (c) AIT_120nm_25sec.
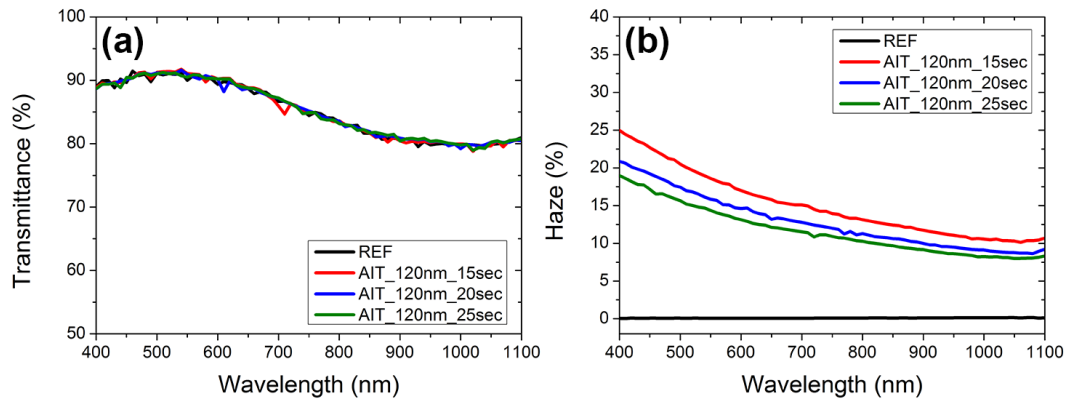
Figure 57. (a) Transmittance and (b) haze of 120 nm Al used samples.

4.1.3. 130 nm Al Coated Samples

For 130 nm Al thickness, 4 sample were prepared by HF:HNO$_3$ etching with 10, 15, 20 and 25 seconds etching durations. In Figure 58(a), it can be observed that AIT_130nm_10sec sample have residue in the craters and regional height differences

are present after 10 sec. of etching by conventional etchants. With the increase of the etching time, the residues were removed as shown in Figure 58(b). At 20 seconds etching time, bigger craters are observed [Figure 58(c)]. In addition, increasing of the etching time led to more uniform surface distribution [Figure 58(d)]. Optically, on the other hand, transmittance was not affected from the texturing process as presented in Figure 59(a). In the haze graph [Figure 59(b)], increase in haze with increasing the etching time from 10 sec. to 15 sec. is observed. Then, further increase resulted in decrease in the haze. The maximum haze for 400 nm wavelength is 32% for AIT_130nm_15sec. The sample etched for 10 sec. (AIT_130nm_10sec) have higher haze than AIT_130nm_20sec for small wavelengths. However, increasing in the wavelength results with different behaviors. At higher wavelengths, AIT_130nm_20sec have higher haze. This change in the scattering behavior is attributed to change in the crater size of the samples. In addition, AIT_130nm_25sec have smaller scattering behavior due to flattening effect with HF usage during etching process.
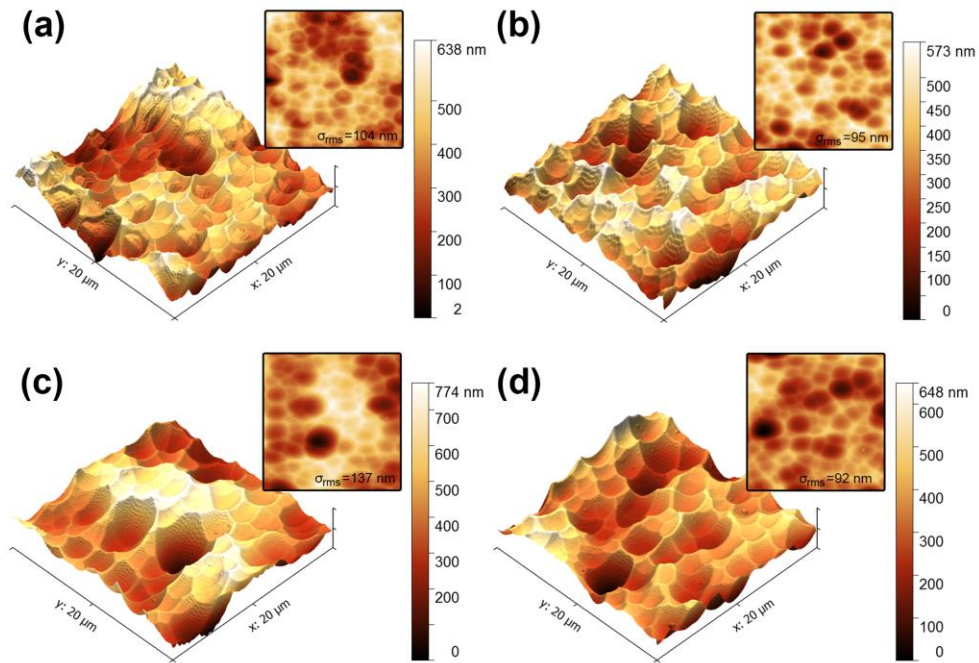
Figure 58. 20 μm x 20 μm AFM images of AIT samples: (a) AIT_130nm_10sec, (b) AIT_130nm_15sec, (c) AIT_130nm_20sec and (d) AIT_130nm_25sec.
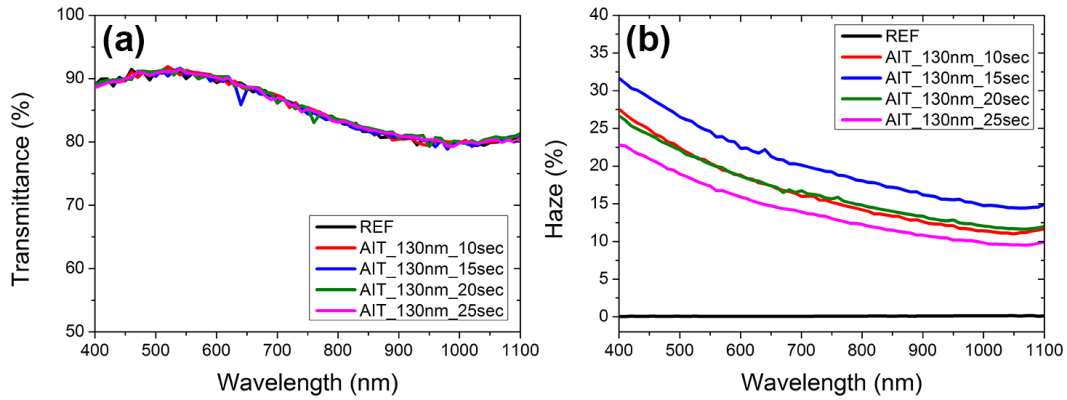
Figure 59. (a) Transmittance and (b) haze of AIT samples coated with 130 nm Al.

4.1.4. 140 nm Al Coated Samples

For 140 nm Al thickness, 3 samples were prepared by $HF:HNO_3$ etching with 15, 20 and 25 seconds etching durations. The evolution of the surface structure with the increase in the etching time can be seen 3D and 2D AFM images having 20 μm x 20 μm scan area presented in Figure 60. In Figure 60(a), it can be seen that after 15 sec. of etching, surface has craters with 2-3 μm diameter and the roughness of the surface is 122 nm. Increase in the etching time to 20 sec. has resulted in shallower craters as seen in Figure 60(b) but the roughness increases to 163 nm due to non-uniformity on the surface. Moreover, 25 sec. etching has resulted in 245 nm roughness and bigger craters as presented in Figure 60(c). On the other hand, optical results given in Figure 61(a) shows that the transmittance of samples do not change. However, the haze decreases with the increase of the etching time as shown in Figure 61(b). The haze of AIT_140nm_15sec is 35% for 400 nm wavelength. In addition, it is 27% for AIT_140nm_20sec and 24% for AIT_140nm_25sec.
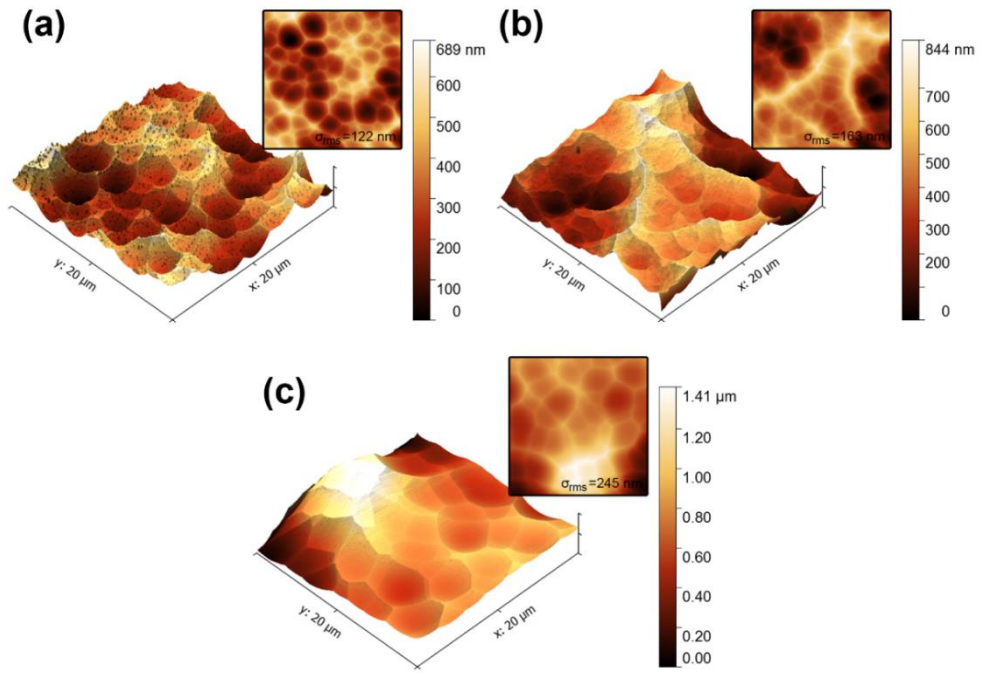
Figure 60. 20 µm x 20 µm AFM images of AIT samples: (a) AIT_140nm_15sec, (b) AIT_140nm_20sec and (c) AIT_140nm_25sec.
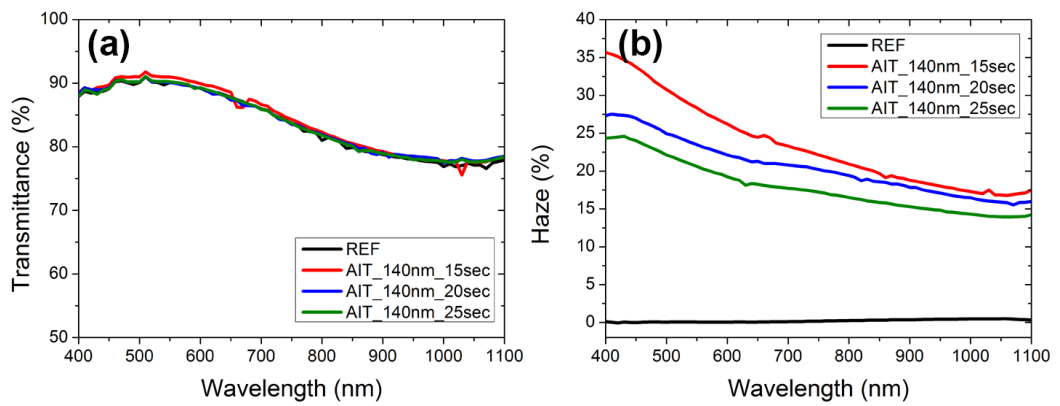
Figure 61. (a) Transmittance and (b) haze of AIT samples coated with 140 nm Al.

4.1.5. 150 nm Al Coated Samples

For 150 nm Al thickness, 3 samples were prepared by HF:HNO$_3$ etching with 15, 20 and 25 seconds etching durations. In Figure 62, surface morphologies of these

samples are given. The same trend as observed in previous samples is present for the morphology. In Figure 62(a), which belongs to the surface of AIT_150nm_15sec, smaller craters are present. With the increase of the etching time, crater size increases. The surface roughness of AIT_150nm_15sec for AFM image given in Figure 62(a) is 82 nm while it is 130 nm for AIT_150nm_20sec and 107 nm for AIT_150nm_25 sec, which are presented in Figure 62(b) and Figure 62(c) correspondingly. Optically, there is no change observed in the transmission as shown in Figure 63(a) while sample having small craters (AIT_150nm_15sec) have higher haze as shown in Figure 63(b), which is, slightly higher than AIT_140nm_15sec, 36% for 400 nm wavelength and decreases with the increase in the wavelength of the light. On the other hand, increase in the etching time gradually decreases the haze as shown. AIT_150_20sec have 30% and AIT_150nm_25sec have 26% haze at 400 nm wavelength.
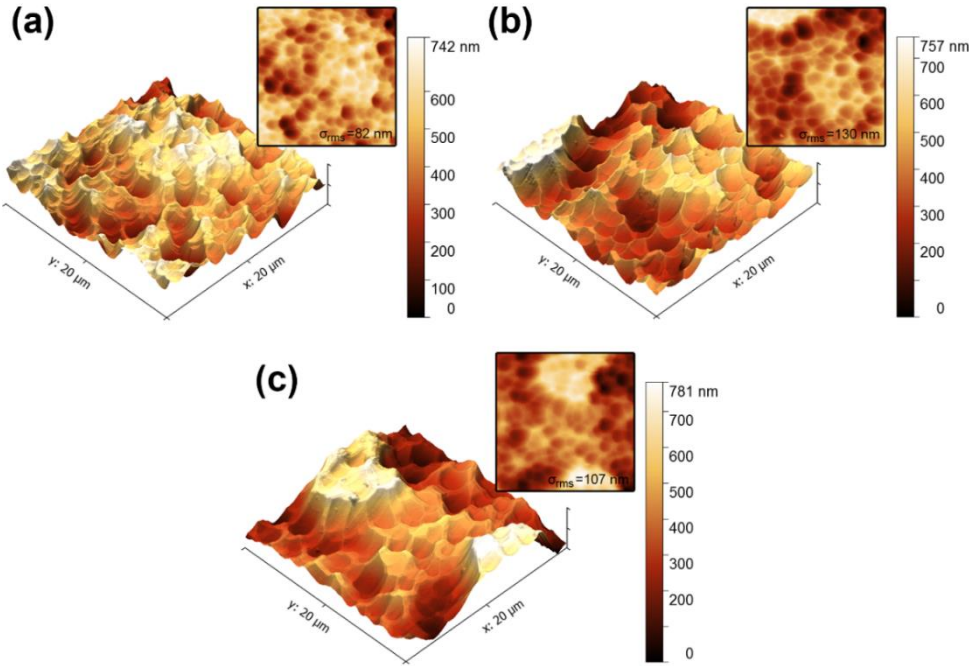
Figure 62. 20 µm x 20 µm AFM images of AIT samples: (a) AIT_150nm_15sec, (b) AIT_150nm_20sec and (c) AIT_150nm_25sec.
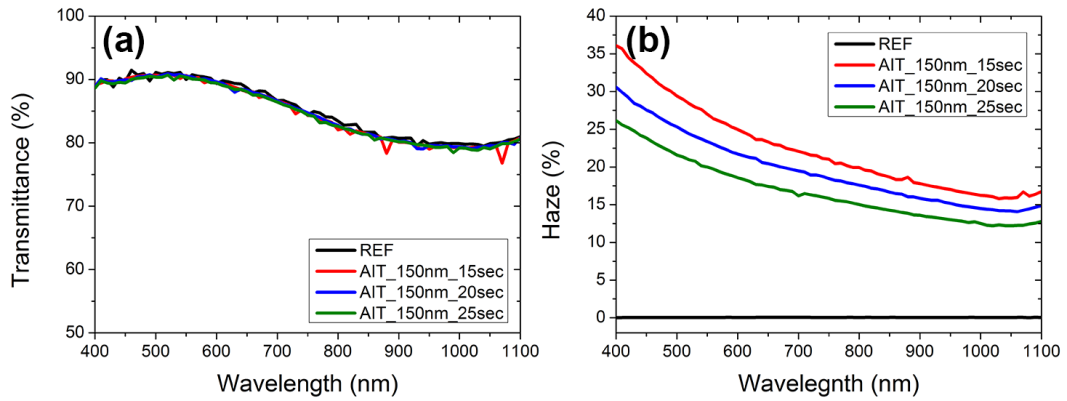
Figure 63. (a) Transmittance and (b) haze of AIT samples coated with 150 nm Al.

4.1.6. 160 nm Al Coated Samples

For 160 nm Al thickness, samples were etched by HF:HNO₃ solution for 15, 20 and 25 seconds. As shown in Figure 64, crater size increases with increase of the etching duration. Also in this thickness, U-shaped craters are formed successfully. Optically, again, there is no change in the transmittance of the samples as presented in Figure 65(a). Maximum haze is obtained with AIT_160nm_20sec, which is 30% for 400 nm wavelength [Figure 65(b)]. In this thickness, it is seen that haze increase with the increase of the etching time from 15 sec. to 20 sec. Then, it drops to same value as 15 sec. etching for 25 sec. etching.
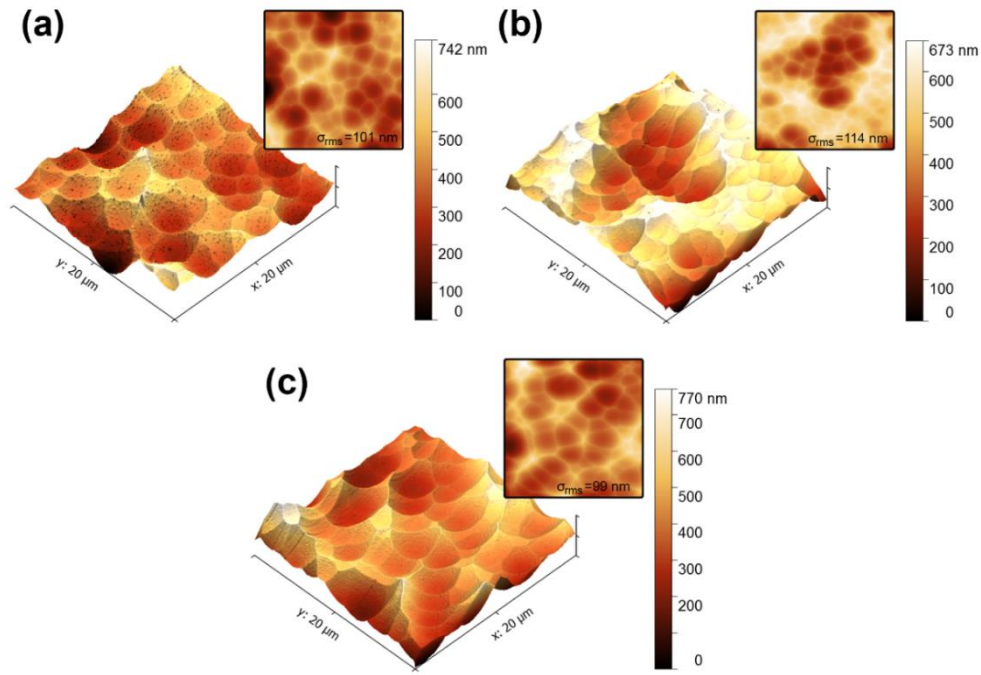
Figure 64. 20 µm x 20 µm AFM images of AIT samples: (a) AIT_160nm_15sec, (b) AIT_160nm_20sec and (c) AIT_160nm_25sec
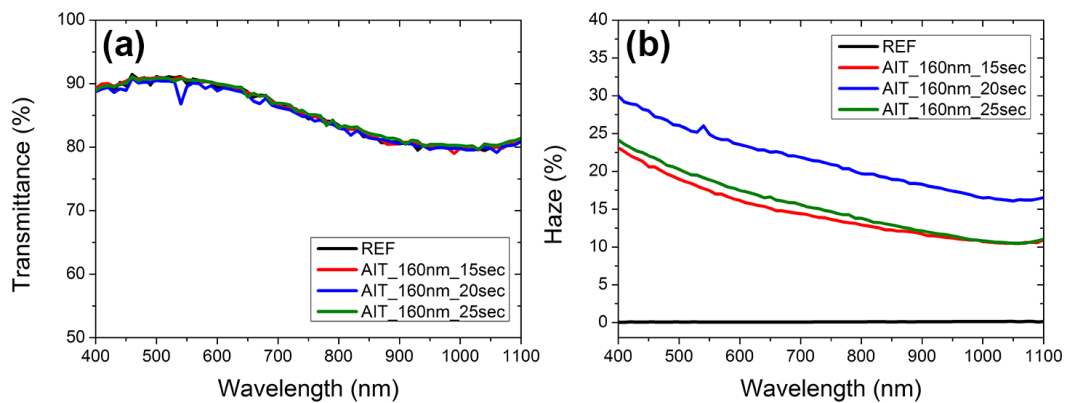
Figure 65. (a) Transmittance and (b) haze of AIT samples coated with 160 nm Al.

4.1.7. 350 nm Al Coated Samples

Up to this point, maximum haze is obtained for the sample with 150 nm Al. To investigate the effect of Al thickness for the extreme values, 350 nm Al was coated. Samples were etched by HF:HNO$_3$ solution with 15, 20 and 25 seconds etching

durations. Figure 66 shows the surface morphologies of these samples taken by AFM with 20 μm x 20 μm scan area. For thick Al usage, small craters are obtained for AIT_350nm_15sec as presented in Figure 66(a). The roughness of this sample is 39 nm. Increasing the etching duration increases the roughness to 71 nm and the size of craters increases for AIT_350nm_20sec, that is shown in Figure 66(b). Further increasing in the etching time led to increase in the crater size with same roughness value as AIT_350nm_20sec for AIT_350nm_25sec as presented in Figure 66(c). In addition, it can be seen that peak to peak value is increasing with increase in the etching time. On the other hand, while there is no significant change in the transmittance of samples as given in Figure 67(a), haze is 8% for 400 nm wavelength at AIT_350nm_15sec [Figure 67(b)]. With the increase of the etching time, surface is restructured, bigger craters formed and haze increase to 23% for AIT_350nm_20sec [Figure 67(b)]. Maximum haze is obtained for AIT_350nm_25sec as 27% at 400 nm wavelength.
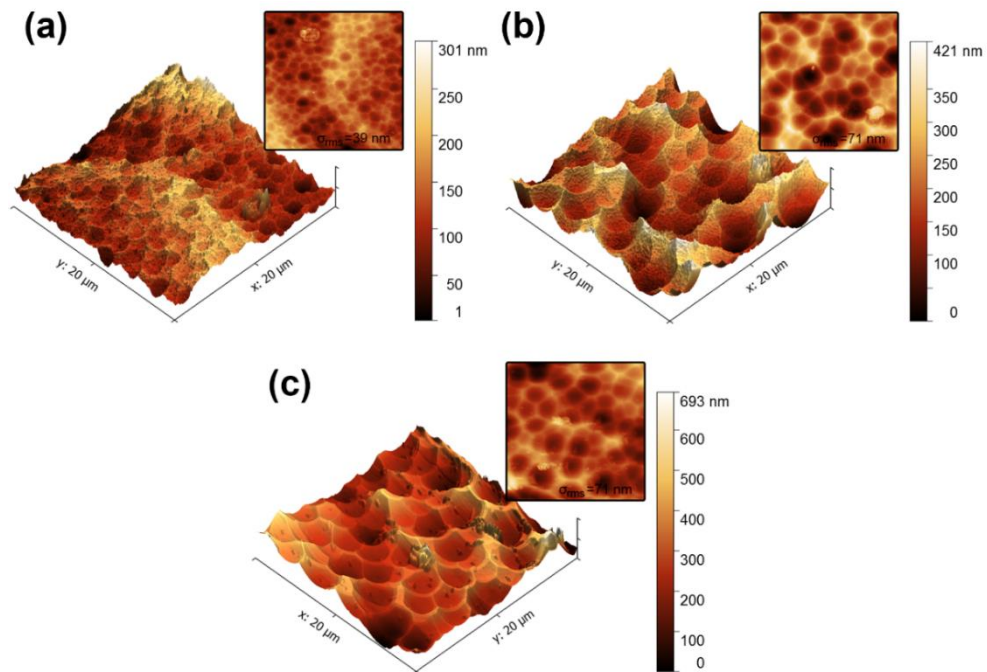
Figure 66. 20 μm x 20 μm AFM images of AIT samples: (a) AIT_350nm_15sec, (b) AIT_350nm_20sec and (c) AIT_350nm_25sec
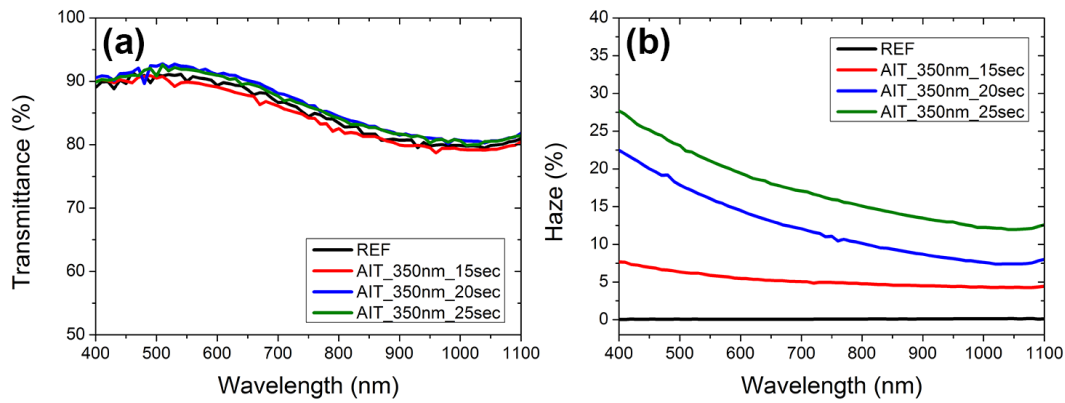
Figure 67. (a) Transmittance and (b) haze of AIT samples coated with 350 nm Al.

4.1.8. Comparison Different Al Thicknesses

Maximum haze value at 400 nm wavelength was obtained for AIT_150nm_15sec, which is 36% and at 1000 nm wavelength, AIT_140nm_15sec has maximum haze of 17%. To observe the effect of the Al thickness in the AIT process, comparison of haze values at 400 nm and 1000 nm for same etching durations is made alongside with 20 µm x 20 µm 2D AFM images of these samples. In Figure 68, it can be seen the haze is maximum for 150 nm Al coated samples. As an exception, 350 nm Al coated and 25 seconds etched sample has similar haze with 150 nm Al coated sample as seen in Figure 68(c). It can be said that for 400 nm wavelength, 150 nm Al coating results with higher haze value. On the other hand, it can be speculated that higher etching duration than 25 sec. for 350 nm Al coated sample could give haze as high as that of AIT_150nm_15sec but it is not logical to use 200 nm more Al and spend more time in the etching to obtain similar haze. In Figure 69, it can be seen that 140 nm Al coated samples perform better for 1000 nm wavelength. However, for 20 sec. etching, the pattern changes. AIT_160nm_20sec have same scattering behavior as of AIT_140nm_20sec for the light having wavelength around 1000 nm, which is 17%. This behavior could be important for thin film technologies having wider bandgap that exhibits low absorption at this wavelength as shown in Figure 15.

86
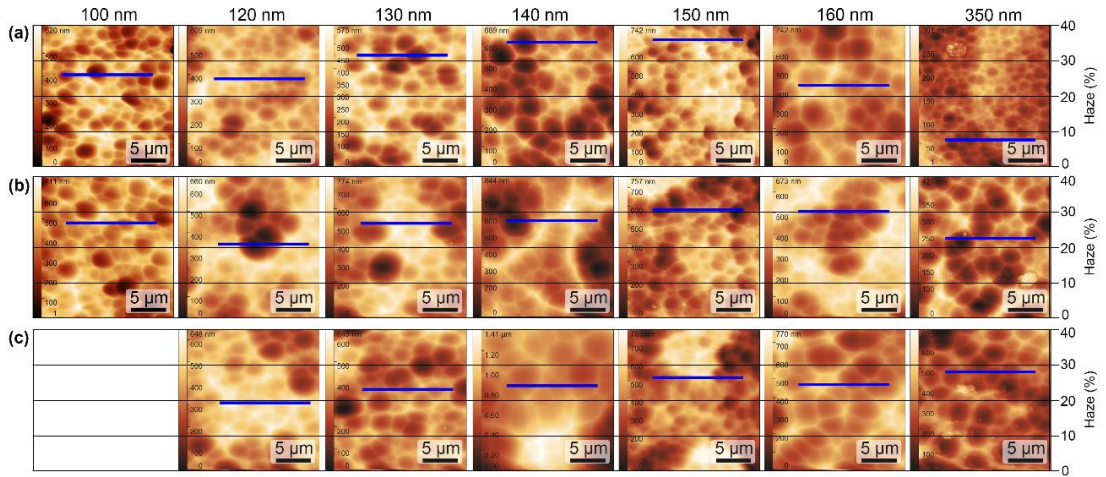
Figure 68. Comparison of the effect of Al thickness in AIT process for 400 nm wavelength at etching durations of (a) 15 sec, (b) 20sec, and (c) 25 sec.
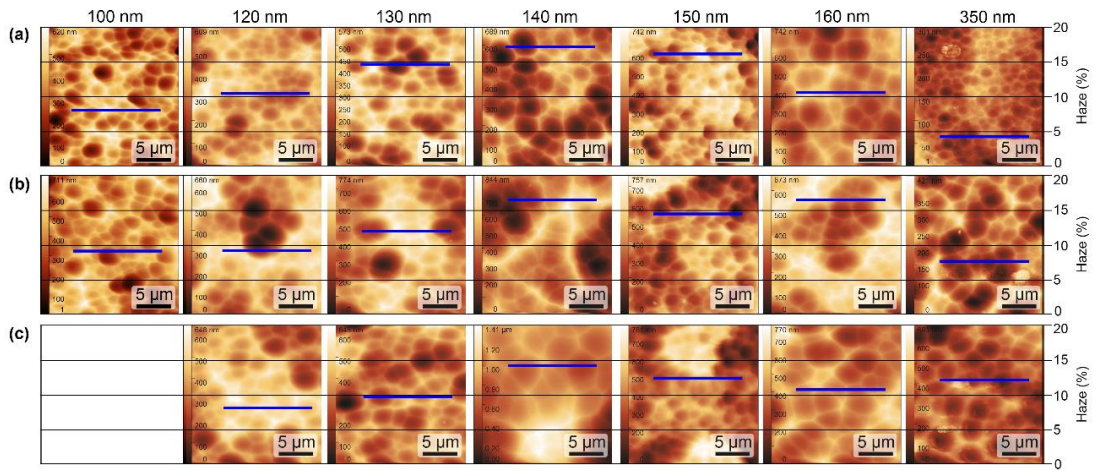
Figure 69. Comparison of the effect of Al thickness in AIT process for 1000 nm wavelength at etching durations of (a) 15 sec, (b) 20sec, and (c) 25 sec.

4.2. HF-free Solution Optimization Studies

4.2.1. First Trials

In order to optimize diluted NaOH:H_2O_2 solution, different parameters were changed from optimized process parameters in conventional AIT process. Sample 1

has assigned as a control sample in which the ratio of NaOH:H_2O_2:H_2O is assigned as 1:20:60. Optical measurements resulted in promising results for this solution as shown in Figure 70. Decrease in the transmission was measured with integrating sphere spectrometer on standard configuration as given in Figure 70(a). With conventional etching procedure, the maximum obtainable haze was 36%. However, by new solution, this value can be pushed up to 65% as shown in Figure 70(b) for Sample 2 in which 4 hour etching was conducted and the minimum haze was obtained for this set of sample is more than 51% for Sample 6 in which 220 nm Al is used. A detailed comparison study according to different parameters were conducted alongside with surface profiles obtained by FE-SEM.
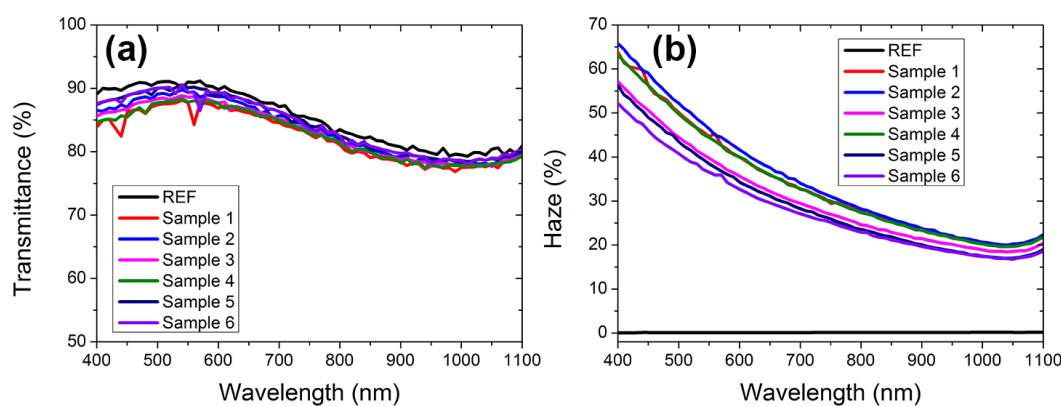
Figure 70. (a) Transmittance and (b) haze of basic etched sample used for optimization of parameters

4.2.1.1. Sample 1: Standard AIT process with NaOH:H_2O_2:H_2O 1:20:60 ratio

Optical results show that Sample 1 which is prepared by new solution has superior scattering behavior than standard etching processes as compared in Figure 71. There is a decrease in the transmittance of Sample 1 observed by integrating sphere spectrometer on standard configuration as presented in Figure 71(a). On the other hand, haze of Sample 1 is around 61% at 400 nm wavelength, which doubles the haze value for standard etchants, in which haze is 36%. It is seen that the decrease in the

haze of Sample 1 with the increase of the wavelength is higher than that of the sample prepared by conventional etchants. To investigate the reason of this behavior, FE-SEM images were taken because attempts to take AFM measurements were failed due to the surface structure. In Figure 72, a comparison of HF used sample and HF-free AIT sample is presented. In Figure 72(a), it is seen that crater size is in the range of 1-5 µm. On the other hand, in Figure 72(b), HF-free solution offers highly porous surface with crater sizes ranging from 200 nm to 1 µm. Due to this change in the crater sizes, Sample 1 has more reduction in the haze with the increase of the wavelength.
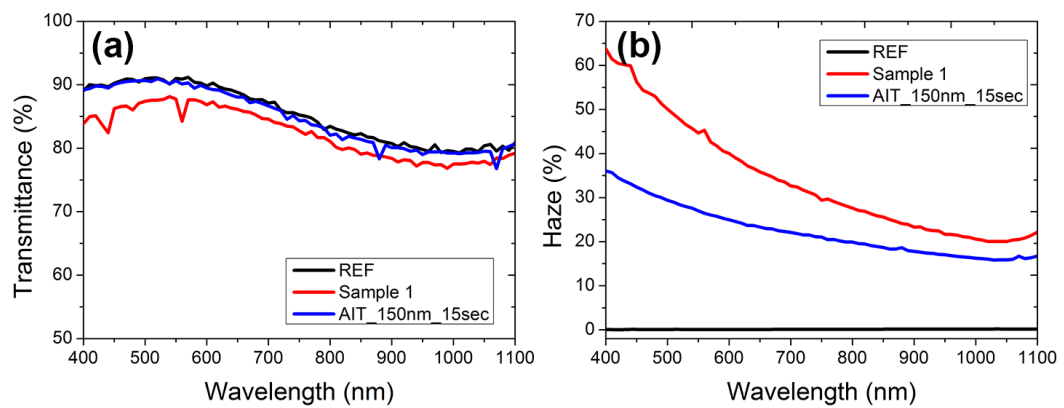
Figure 71. (a) Transmittance and (b) haze of Sample 1 and AIT_150nm_15sec measured by integrated sphere spectrometer on standard configuration
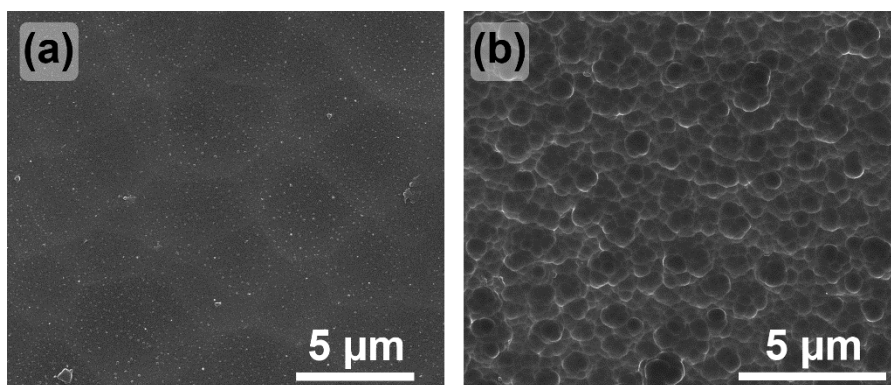
Figure 72. FE-SEM images of (a) AIT_150nm_15sec and (b) Sample 1.

In addition, there are some nodules present on the surface as presented in Figure 73(a). In Figure 73(b), tilted view of one of these nodules is present. These nodules are elevated from the surrounding. This might be the reason behind the trouble with AFM measurements. In addition, porous like surface structure can be seen clearly in the tilted view.
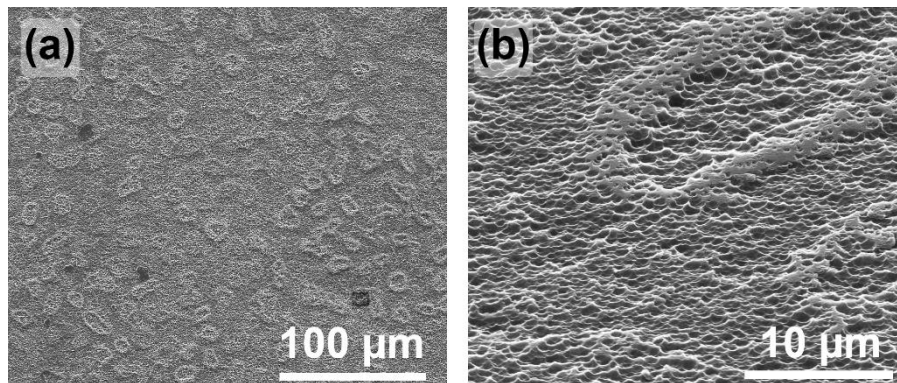
Figure 73. FE-SEM image of Sample 1 with (a) 1000x magnification and (b) 10000x magnification with 60° tilt angle

4.2.1.2. Sample 2: Etching Time Doubled (8 hours)

When the etching time is doubled, it is observed that there is a slight increase in the transmission as shown in Figure 74(a). In addition, same enhancement can be seen in haze results. The haze of Sample 2 is increased to 65%, whereas Sample 1 has 61% haze for 400 nm wavelength, which is shown in Figure 74(b). On the other hand, surface structure has not changed significantly as seen in Figure 75.
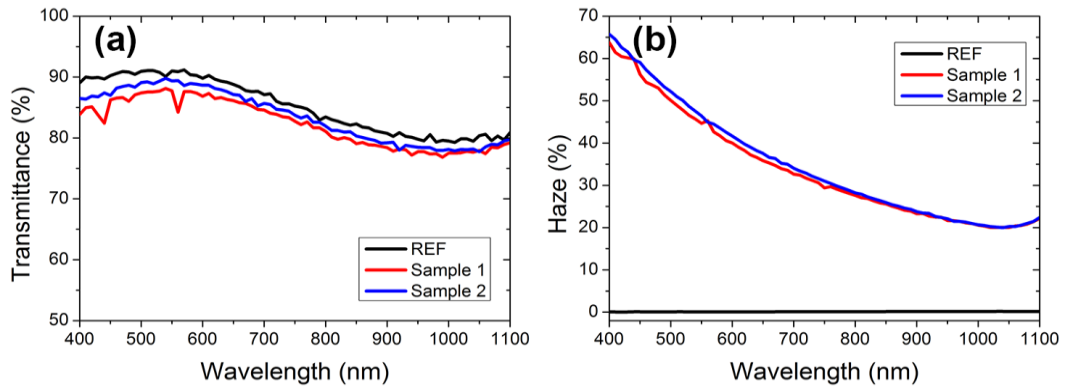
Figure 74. Optical comparison of Sample 2 and Sample 1: (a) Transmittance and (b) haze
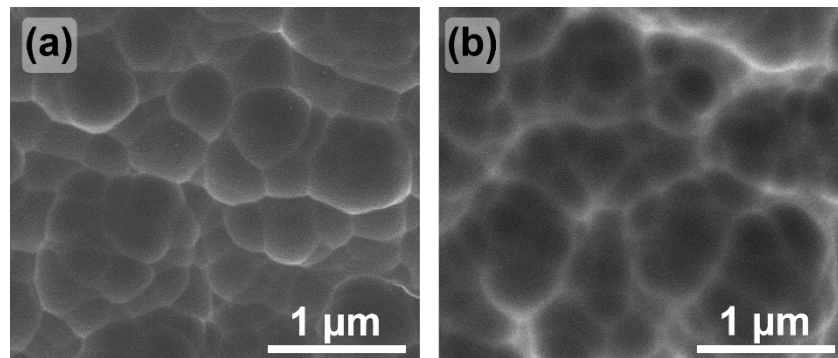
Figure 75. FE-SEM images of (a) Sample 1 and (b) Sample 2

4.2.1.3. Sample 3: Less NaOH Content (1:40:120 ratio of $NaOH:H_2O_2:H_2O$)

Reducing the NaOH content in the etching solution causes a decrease in the haze of the Sample 3 without a change in transmittance. The haze is decreased to 57%. Optical results are presented in Figure 76. Morphologically, it is seen that residues present on the surface of Sample 3 as seen in Figure 77(b). In addition, at general view of Sample 1 and Sample 3, presented in Figure 77(c) and Figure 77(d), it can be observed that middle of nodules are empty for Sample 1 while it is filled in Sample 3. In addition, when these nodules are investigated by EDX, it is observed that there is Al present on these nodules as presented in Figure 78. The atomic and weight

percentages of elements present in the glass and over layer are given in Table 12 that is obtained with 20 keV acceleration energy.
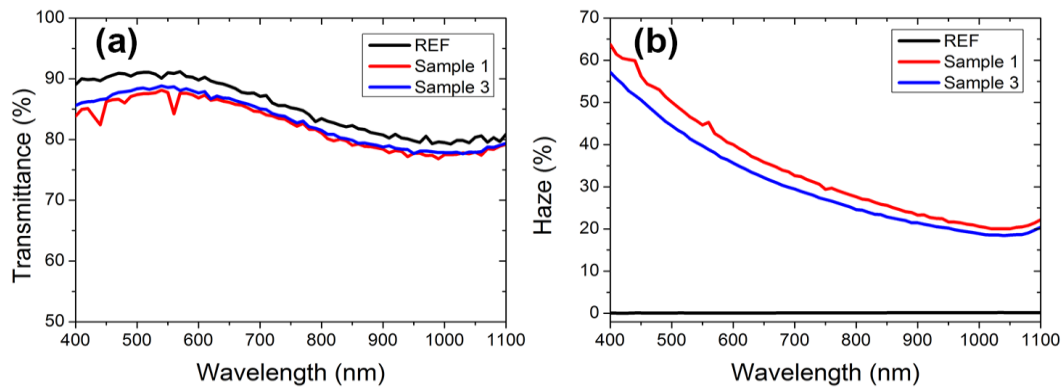
Figure 76. Comparison of Sample 1 and Sample 3: (a) transmittance and (b) haze.
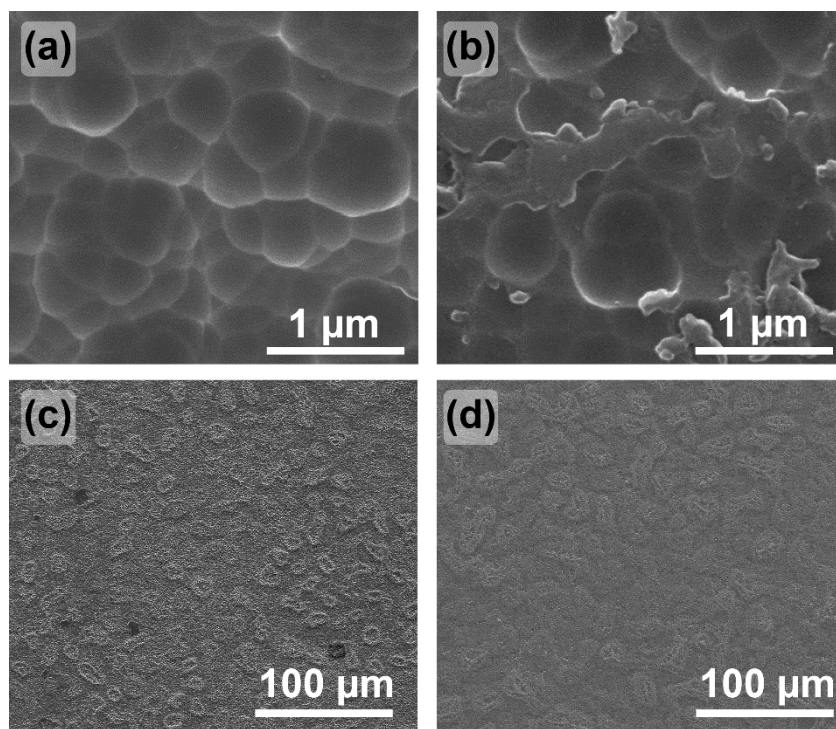
Figure 77. FE-SEM images of (a) Sample 1 and (b) Sample 3. General view of (c) Sample 1 and (d) Sample 3.
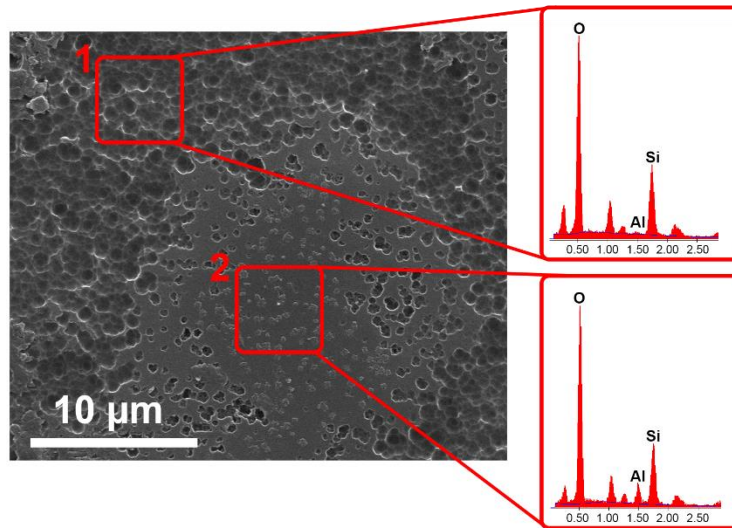
Figure 78. EDX measurement of surface and nodules of Sample 3.

Table 12. Weight percentage and atomic percentage for Area 1 and Area 2 defined in Figure 78

Element	Area 1 Wt %	Area 1 At %	Area 2 Wt %	Area 2 At %
C	9.90	20.00	6.26	12.90
O	29.25	44.33	30.92	47.85
Na	6.45	6.80	5.40	5.81
Mg	2.07	2.07	2.47	2.52
Al	0.54	0.49	5.6	5.14
Si	26.93	23.26	25.90	22.83
Au	24.85	3.06	23.45	2.95
Ca	0	0	0	0
Total	100	100	100	100

4.2.1.4. Sample 4: Diluted Solution (1:20:100 ratio of NaOH:H_2O_2:H_2O)

When solution is diluted, no optical change was observed as shown in Figure 79. The haze of the Sample 4 is 61% like that of Sample 1 for 400 nm wavelength. In addition, Sample 4 has similar surface structure as shown in Figure 80(a)-(b). On the other hand, in general view of the samples, it is seen that some of the nodules have not empty center. Due to the fact that Al_2O_3 has high bandgap, which transmits the 400-1000 nm region and these kind of nodules are not common, it has no effect on optical properties. However, these regions could be hazardous for thin film solar cell application.
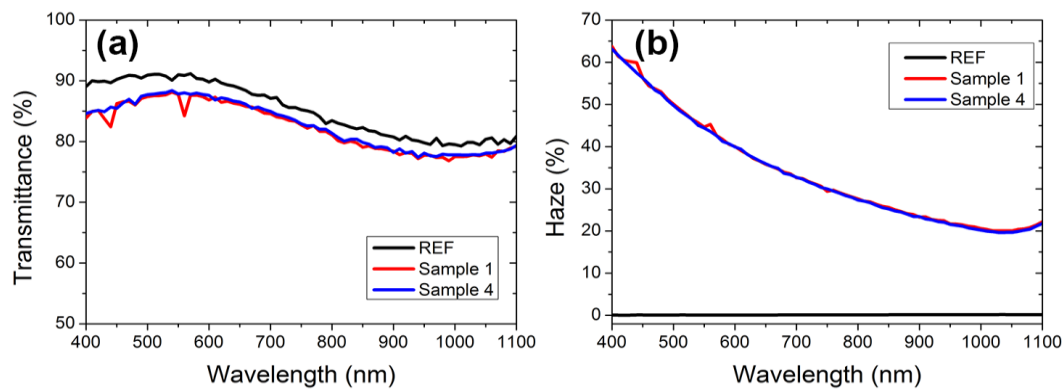
Figure 79. Comparison of (a) Transmittance and (b) haze of Sample 1 and Sample 4
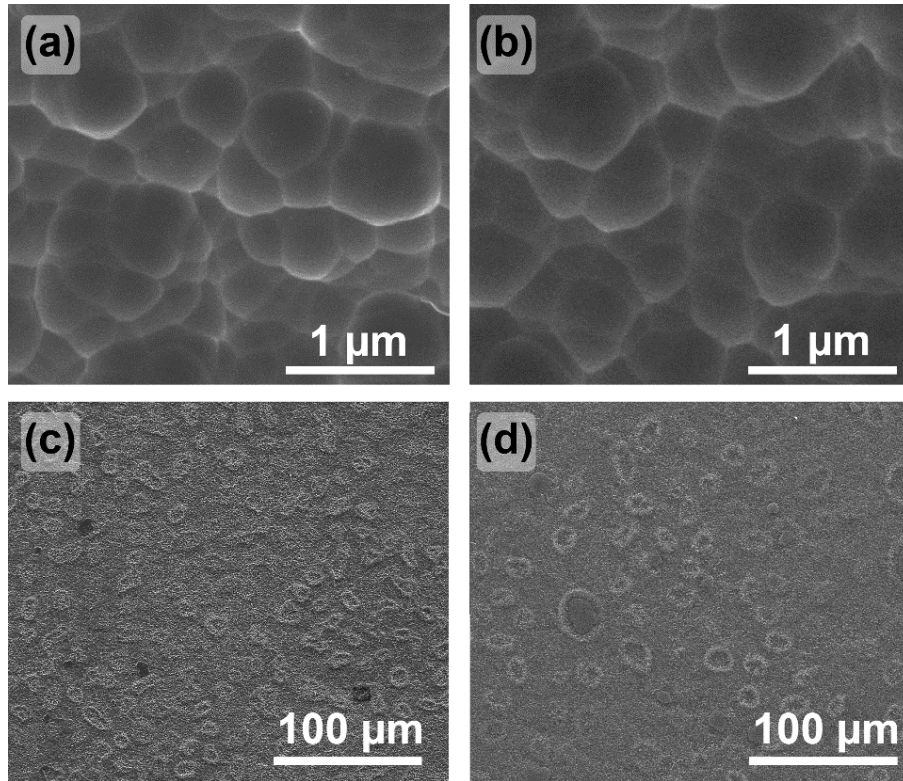
Figure 80. Comparison of Sample 1 and Sample 4 by FE-SEM: (a) Sample 1, (b) Sample 4, (c) General view of Sample 1 and (d) General view of Sample 4.

4.2.1.5. Sample 5: Double Annealing Time (2 hours at 600 °C)

When the annealing time is doubled, haze was observed to decrease. In addition, the transmittance of Sample 5 was close to the reference float sample as shown in Figure 81. The haze is decreased to 54% for 400 nm wavelength. On the other hand, there is no significant change in the FE-SEM images as presented in Figure 82.
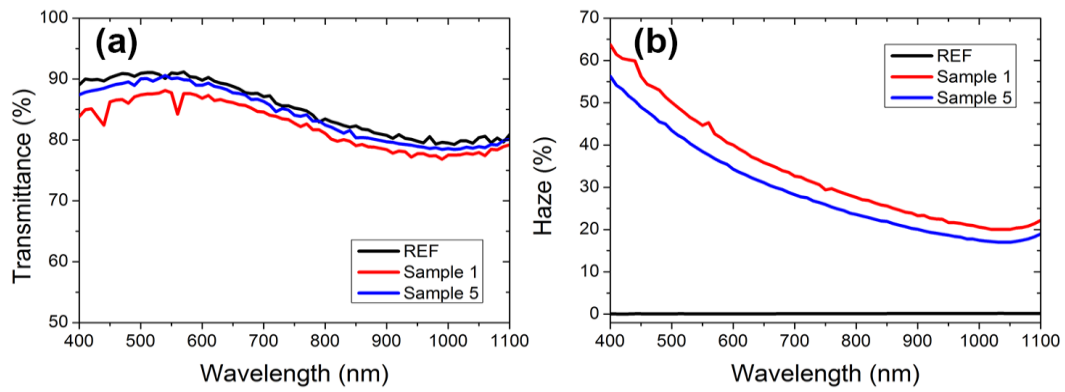
Figure 81. Optical comparison of Sample 1 and Sample 5: (a) transmittance and (b) haze
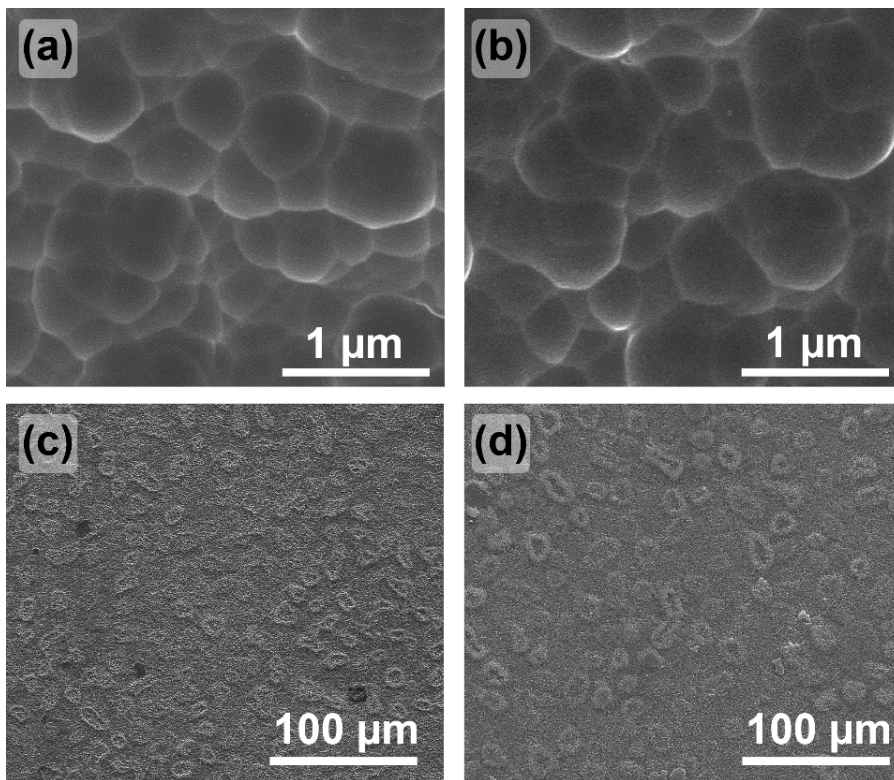
Figure 82. FE-SEM images of (a) Sample 1, (b) Sample 2. General view of surfaces of (c) Sample 1 and (d) Sample 5.

4.2.1.6. Sample 6: Thicker Al (220 nm)

When the Al thickness is increased from 150 nm to 220 nm, float regions on the surface of Sample 6was observed as presented in Figure 83(b). These float regions are probably Al_2O_3 residue on the surface because no decrease in the transmission is observed as given in Figure 84(a). In addition, due to high density of these float regions, the haze is decreased to 51%, which is the minimum haze value among Samples 1-6.
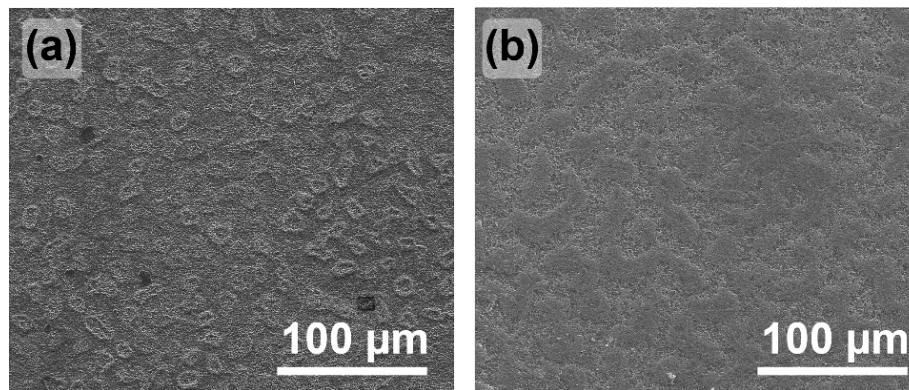
Figure 83. General view of (a) Sample 1 and (b) Sample 6.
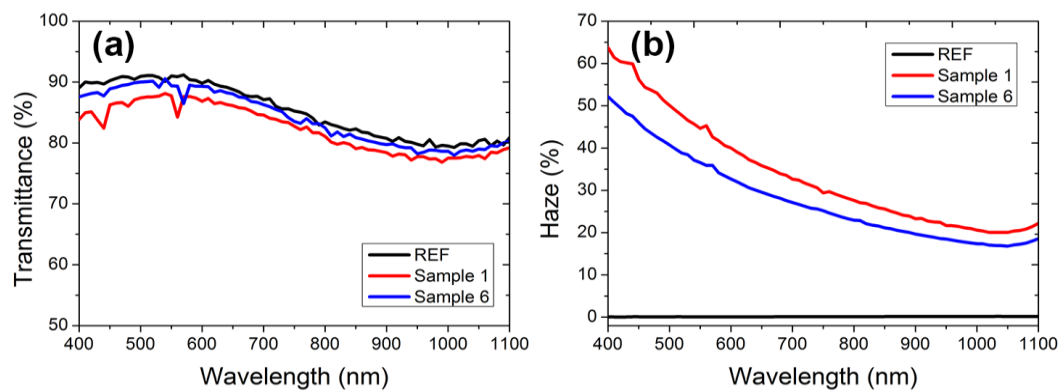
Figure 84. Optical comparison of Sample 1 and Sample 6: (a) Transmittance and (b) haze.

First trials revealed that $NaOH:H_2O_2:H_2O$ offers effective scattering interface for thin film solar cells. However, long etching durations (8 hours) and nodules on the surface are two main problems of this solution. Because of the fact that this new basic solution does not affects the glass surface, that can be seen by comparison of FE-SEM image of Sample 1 and Sample 2, these nodules could have been formed during the reaction in the annealing step. For detailed investigation of this solution, however, evolution of the surface with the increase in the etching duration is studied. In addition, the solution has made concentrated as an attempt to decrease the etching time.

4.2.2. Investigation of the Evolution of Surface During Etching by Basic Solution with 1:2:6 Ratio

The evolution of the surface is investigated by FE-SEM through Figure 85(a) to Figure 85(h). After 30 min of etching by concentric new basic solution at 75 °C, nodules that are observed in first trials exposed. However, glass surface is not revealed. After 40 min of etching, cracks on the surface is observed. In Figure 86(a), it can be seen that some part of the over layer is removed. However, after 50 min of etching, significant portion of the textured surface is exposed. In a closer look, it is seen that in the boundary of textured surface and over layer, particles filled the texture craters as presented in Figure 86(b). In addition, 60 min of etching can remove all reaction products on the surface. There is no change in the surface structure observed for further etching durations. The texture can be seen in Figure 87.
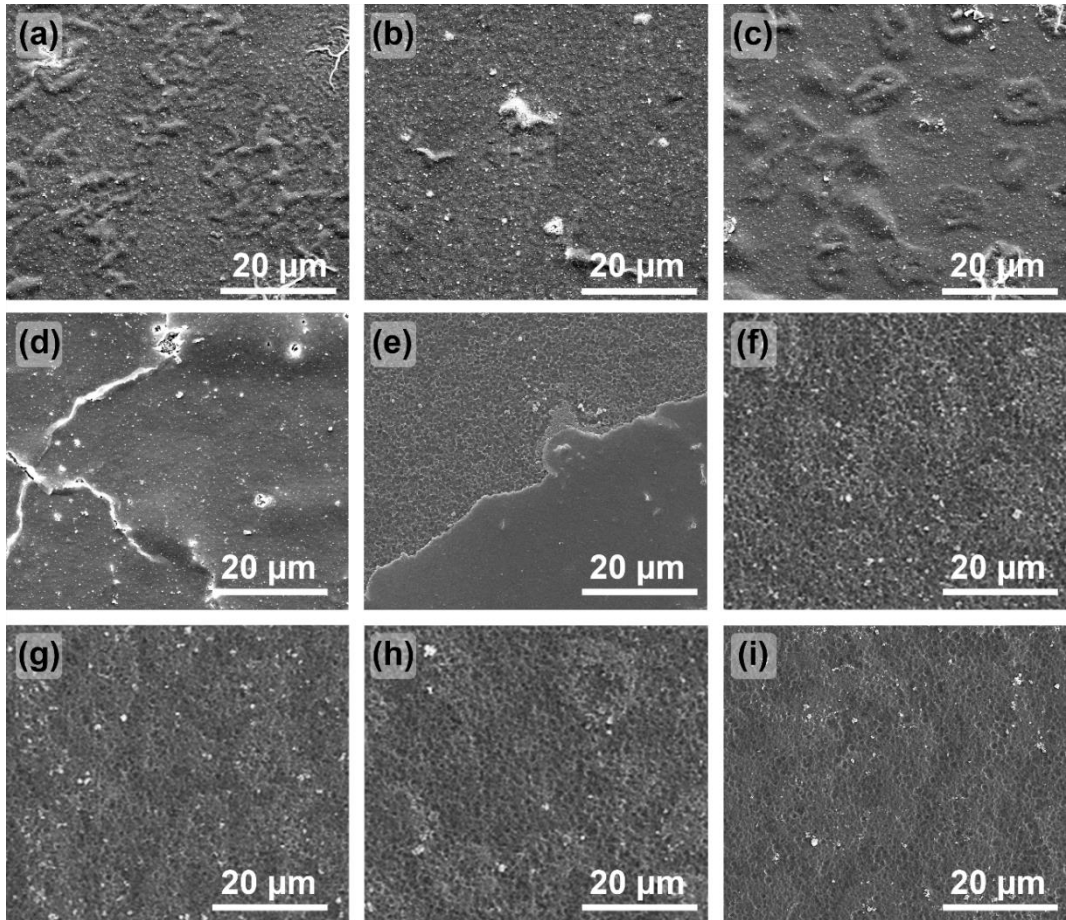
Figure 85. FE-SEM images of the evolution of the surface during etching by basic solution: (a) 10 min, (b) 20 min, (c) 30 min, (d) 40 min, (e) 50 min, (f) 60 min, (g) 90 min, (h) 110 min and (i) 120 min of etching at 75 °C.
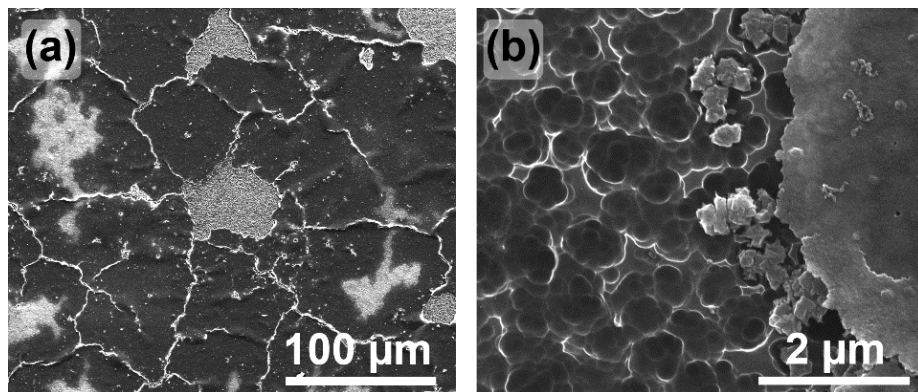
Figure 86. Surface of sample after (a) 40 min and (b) 50 min of etching by basic solution
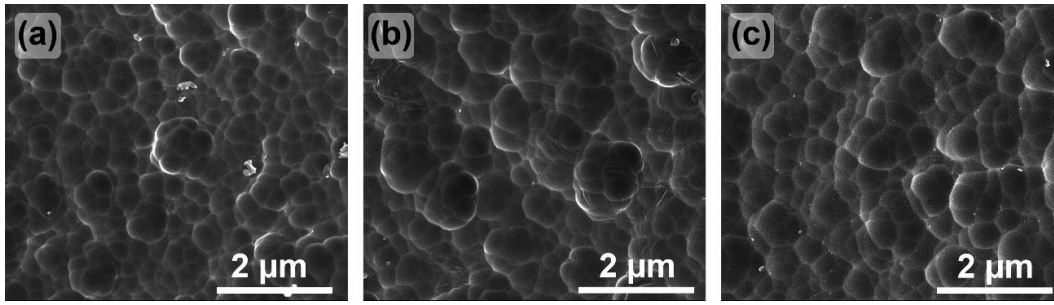
Figure 87. Texture of surface after (a) 60 min, (b) 90 min and (c) 120 min of etching by basic solution

The etching duration is decreased from 8 hours to 1 hour as discussed above with concentric solution. Further decrease can be obtained by increasing the etching temperature or using sonication during etching.

4.3. Comparison of HF-free Solution with Conventional Etchant

The obtained results from recipes that employ conventional etching and HF-free etching processes have presented separately in previous sections. In this section, a consistent comparison was made with 8 samples that are coated with 150 nm Al and annealed at 550 °C. The change in the annealing temperature is made according to annealing optimizations discussed in the section, 4.4. Annealing Optimization. The optical characterization of these samples are made by integrated sphere spectrometer in inverted configuration to decrease the error in the measurement coming from non-uniform distribution of the light in the integrated sphere.

It is observed in the optical measurements presented in Figure 88 that there is an enhancement in the transmittance for all samples. However, for HF containing etching process, the transmission is decreasing to the transmittance value of reference glass with the increase of etching time as shown in Figure 88(a). The reason for the decrease is the decrease in the haze of the HF-used glasses with the increase of the etching duration, which can be observed in Figure 88(b). 50% haze is obtained for 15

seconds etched glass by conventional HF containing solution. When the etching duration is increased to 30 seconds, haze decreases to 30%. Finally, 90 seconds etching results with 7% haze. On the other hand, for newly developed solution that does not contain HF, the enhancement in the transmittance is significant as given in Figure 88(a). The transmittance of the glass is increases from 87% to 92% for 400 nm wavelength. The haze of NaOH etched samples is significantly higher than the ones obtained by conventional etching as presented in Figure 88(b). The haze for NaOH_0.5h is 80% for 400 nm wavelength and it is not changing with the further increase of the etching duration as measured for 1 and 3 hours of etching.
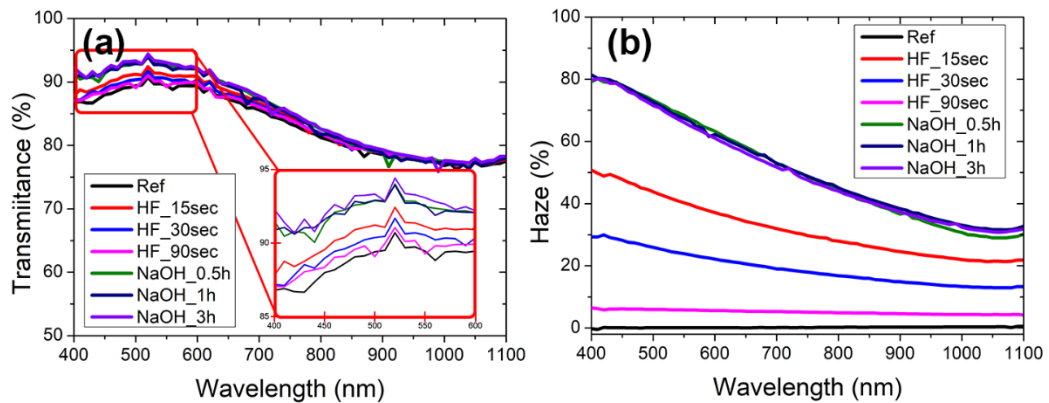
Figure 88. Optical comparison of AIT samples prepared by conventional etchants and Hf-free solution: (a) Transmittance and (b) haze.

Figure 89 shows 3D and 2D AFM images of corresponding samples. It is observed that with the increase of the etching time with HF based solution, the surface roughness decreases and craters got bigger as given in Figure 89(a)-(c). The change in the surface morphology with the increase of the etching time resulted with decrease in the haze. On the other hand, for NaOH based solution used AIT samples, craters are small and the morphology did not changed with the increase of the etching time as presented in Figure 89(d)-(f).
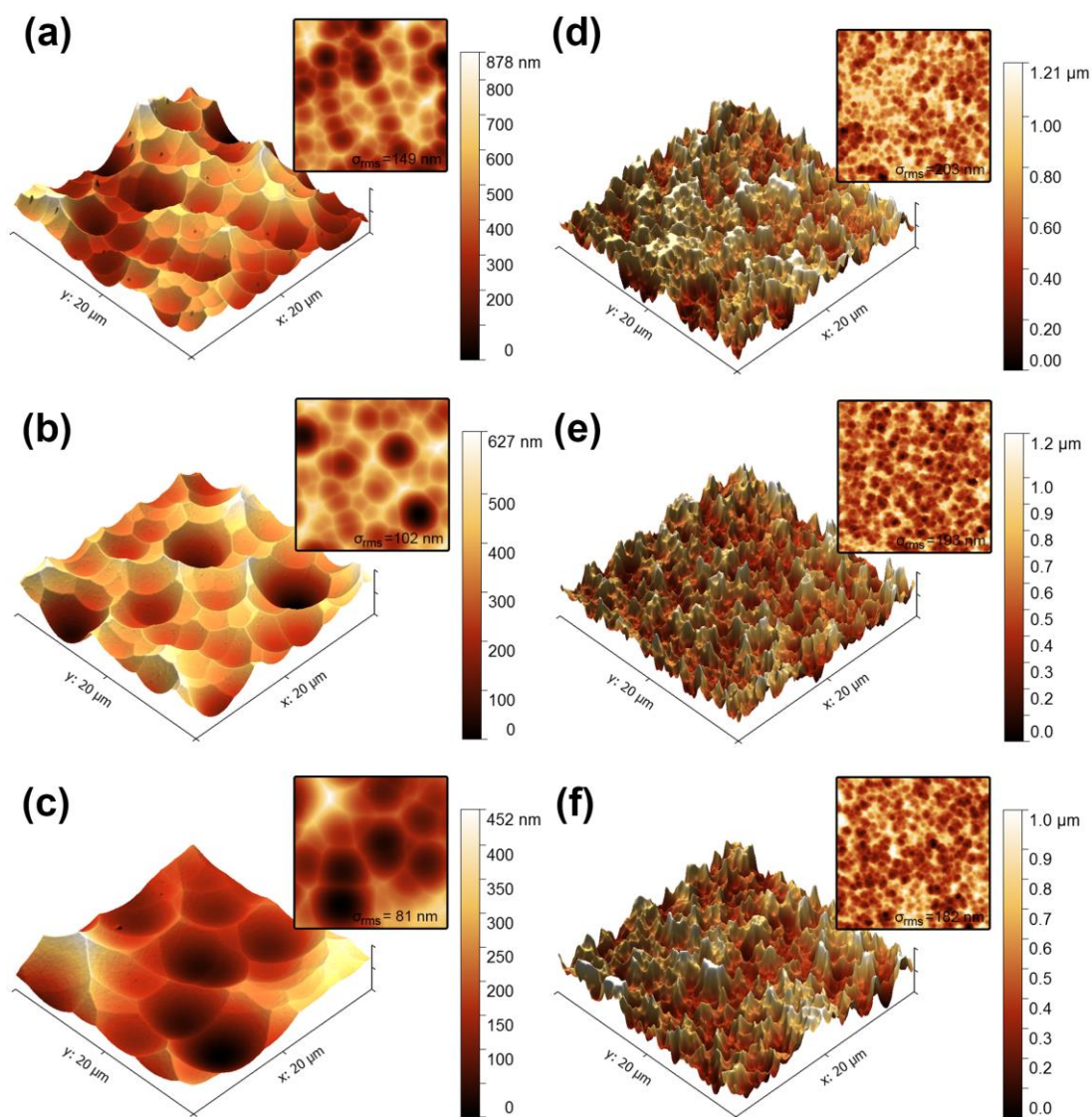
Figure 89. 20 μm x 20 μm AFM images of (a) HF_15sec, (b) HF_30sec, (c) HF_90sec, (d) NaOH_0.5h, (e) NaOH_1h and (f) NaOH_3h.

4.4. Annealing Optimization

For the optimization of annealing step, firstly, annealing ambient was investigated. Then, structural analysis for different annealing durations was made by XPS, which is supported by optical microscope images, to obtain information about the evolution of the Al/Al$_2$O$_3$ over layer. For a detailed investigation, evolution of the surface was investigated alongside with SEM and EDX with the effect of the annealing

102

conditions that are temperature and duration on the final texture, which is important to eliminate non-uniformity on the surface texture exposed by basic solution.

4.4.1. Annealing Ambient Optimization

The AIT process is basically an oxidation process of Al. For an effective annealing process, the annealing ambient is important because Al can be oxidized by oxygen in the air. To investigate the annealing ambient effect, 2 samples that are coated with 150 nm Al and annealed for 1 hour at 600 °C were prepared. Two different ambients, air and N_2, were used.

It is seen that samples have discontinuities on the film after annealing on both N_2 ambient and air. These discontinuities have circular shapes. However, the density of these shapes changes for different annealing ambients. A150_N2 has low density of discontinuity as shown in Figure 90 while A150_AIR have high density of discontinuity as shown in Figure 91.
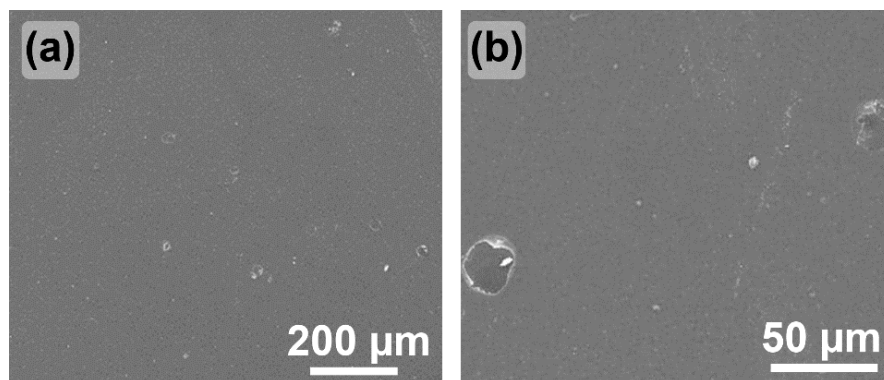
Figure 90. SEM image of A150_N2 with (a) 100x and (b) 500x magnification
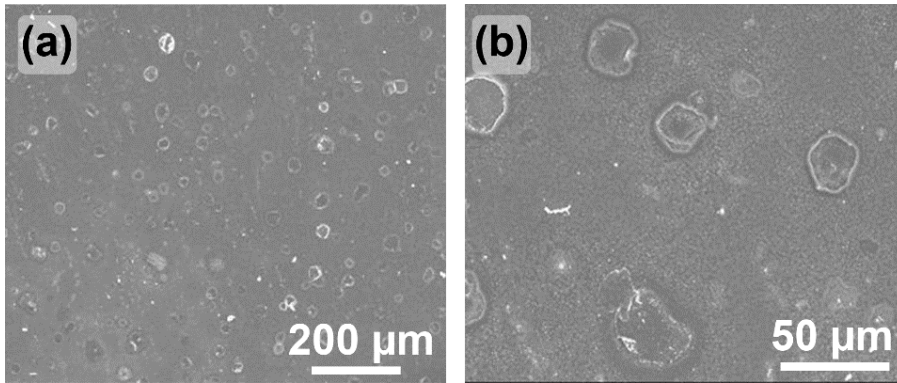
Figure 91. SEM image of A150_N2 with (a) 100x and (b) 500x magnification.

To understand the nature of these discontinuities, EDX measurement was conducted. In the FE-SEM image of the sample, which is presented in Figure 92(a), it is seen that these circular shapes are like exploded bubbles. The marked area, 1, has no Al detectable by EDX while area 2 has significant amount of Al as shown in Figure 92(b). The weight percentage and atomic percentage obtained from EDX measurements are given in Table 13.
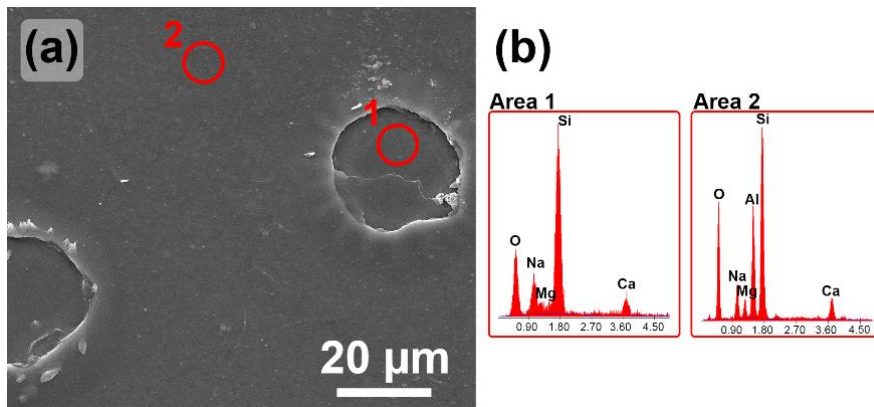
Figure 92. (a) FE-SEM image of annealed sample under air with 3000x magnification, 20 kV acceleration voltage and (b) EDX measurements of numbered areas.

Table 13. Weight percentage and atomic percentage for Area 1 and Area 2 defined in Figure 92.

Element	Area 1		Area 2	
	Wt %	At %	Wt %	At %
O	39.63	52.96	37.91	51.44
Na	11.58	10.77	6.15	5.81
Mg	3.26	2.86	2.70	2.41
Al	-	-	15.37	12.37
Si	40.02	30.47	32.26	24.94
Ca	5.51	2.94	5.60	3.03
Total	100	100	100	100

There are two mechanisms that could explain the formation of these discontinuities. The first mechanism is that the thermal expansion differences causes hillock formation [116], [125], [126]. Then, because of the reaction between Al and glass, these hillocks become bubbles. The thermal expansion coefficient of the Al is 28×10^{-6} °C^{-1} [127]. On the other hand, the thermal expansion coefficient of the glass is less than 10×10^{-6} °C^{-1} [128], [129]. The total volume of the hillocks can be calculated with the given formula in Eq. 26.

$$V_{hillock} = 2t_f(\alpha_{al} - \alpha_{sub})(T - T_c)$$

(Eq. 26)[116]

where $V_{hillock}$ is the volume of the hillock, t_f is the film thickness, α_{al} is the thermal expansion coefficient of Al, α_{sub} is the thermal expansion coefficient of the substrate, T is the annealing temperature and T_c is the critical temperature where plastic deformation occurs, which is reported as 90 °C for glass/Al case [116]. This kind of discontinuities are inevitable during annealing.

The second mechanism is the interaction of the film with air molecules by surface diffusion. O_2/H_2O in the air can penetrate into the interface and causes increase

in the density of hillocks on the surface. For different metals, hillock formation due to O_2 annealing has reported [130].

It is observed that annealing under air disturbs the surface uniformity. Different mechanisms are proposed to understand the formation of discontinuities on the film.

4.4.2. XPS Study on Annealing Effect for Al/Glass Interface During AIT

In this study, survey scans have obtained from 350 nm Al coated samples. On the other hand, for detailed scans, 130 nm Al coated samples are used to decrease the sputtering time during depth profiling by XPS. In addition, these samples were annealed at 600 °C with different durations. Soda-lime glass investigated in this study has a composition that is given in Table 14. The morphology of the samples was investigated by optical microscope and the structural and compositional distribution was studied with PHI Versaprobe 5000 Scanning X-Ray Photoelectron Spectrometer (XPS) with Al Kα as an X-ray source by depth profiling.

Table 14. Chemical composition (wt%, approx.) of soda-lime float glass

SiO_2	Al_2O_3	CaO	MgO	Na_2O	Trace
71.8	1.1	8.2	4.4	14.3	0.2

The evolution of the film during annealing was monitored by optical microscopy, as shown in Figure 93 for 350 nm Al coated samples. After 5 minutes of annealing, there are dark spots that can be observed by reflected light, which appear as bright regions under transmitted light as given in Figure 93(a). The surface morphology was dramatically changed after 7 minutes of annealing; elongated features that resemble peanut shells with a high contrast can be seen in the reflection images, while the density of the bright spots on the transmission image has greatly increased as shown in Figure 93(b). After 10 min. of annealing, as presented in Figure 93(c), a

more uniform contrast is seen for the reflection image, whereas areas with high brightness can be observed in the transmission image.
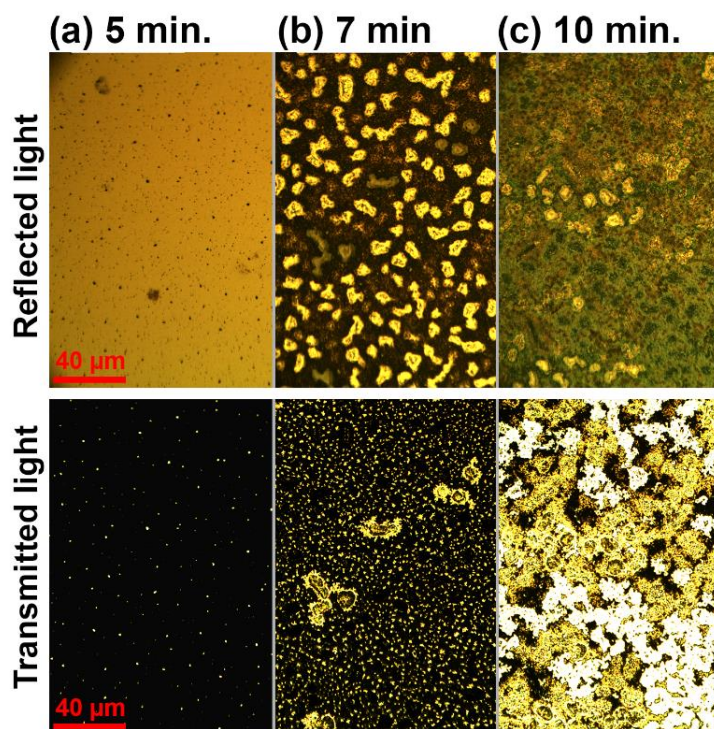
Figure 93. Optical microscopy images of 350 nm Al coated samples annealed for (a) 5 min., (b) 7 min. and (c) 10 min. at 600 °C recorded by using reflected light (top) and transmitted light (bottom).

The dark features seen in 5 min. annealed sample with reflected light [Figure 93(a)] are probably representative of Al_2O_3 formed during early stage of annealing because of its high transmittance resulted from wide bandgap of Al_2O_3 [131], [132]. On the other hand, in sample annealed for 7 min. given in Figure 93(b), bright regions observed by reflected light are c-Si clusters formed around Al_2O_3. c-Si probably acts as a diffusion barrier to Al and hinders its interaction with the oxide layer. Accordingly, Al on top of c-Si remains metallic and yield high brightness in the reflection image. Optical image of 7 min. annealed sample taken by transmitted light reveal a drastic intensity increase in the number of bright Al_2O_3 spots. In addition, several areas where the Al_2O_3 nodules have accumulated can be identified. We

speculate that these areas are preferential nucleation sites for Al_2O_3 (such as cracks and/or other morphological defects), which promotes a reduction in activation energy. When we look at the sample annealed for 10 min. [Figure 93(c)], bright regions seen by reflected light in the sample annealed for 7 min. [Figure 93(b)] are disappeared due to oxidation of Al at later stage of annealing. By looking at low reflectance and high transmittance of this sample, it can be said that most of the Al is oxidized.

The compositional distribution at 10 min annealed sample was investigated by XPS with as-deposited film and soda-lime glass substrate. Figure 94 shows composition distribution of non-annealed Al film and soda-lime glass. In Figure 94(a), it is seen that the film is metallic Al as expected. The plasmon peaks of metallic Al can also be noticed in Figure 94(a). Peaks present in the survey scan of non-annealed film are identified as Al2p (72 eV) and Al2s (117 eV) with plasmon satellite peaks as summarized in Table 15. The constituents of the soda-lime float glass can be observed in Figure 94(b), which appears to be in accordance with Table 14. It is observed that there is Al present in the glass appears at 75 eV that belongs to Al2p energy in Al_2O_3 structure. In addition, oxide peaks of other components of the glass are identified as Na_2O, CaO, MgO and SiO_2, which are given with peak positions in Table 15. These two spectra indicate two distinct layers (Al and glass) prior to annealing.
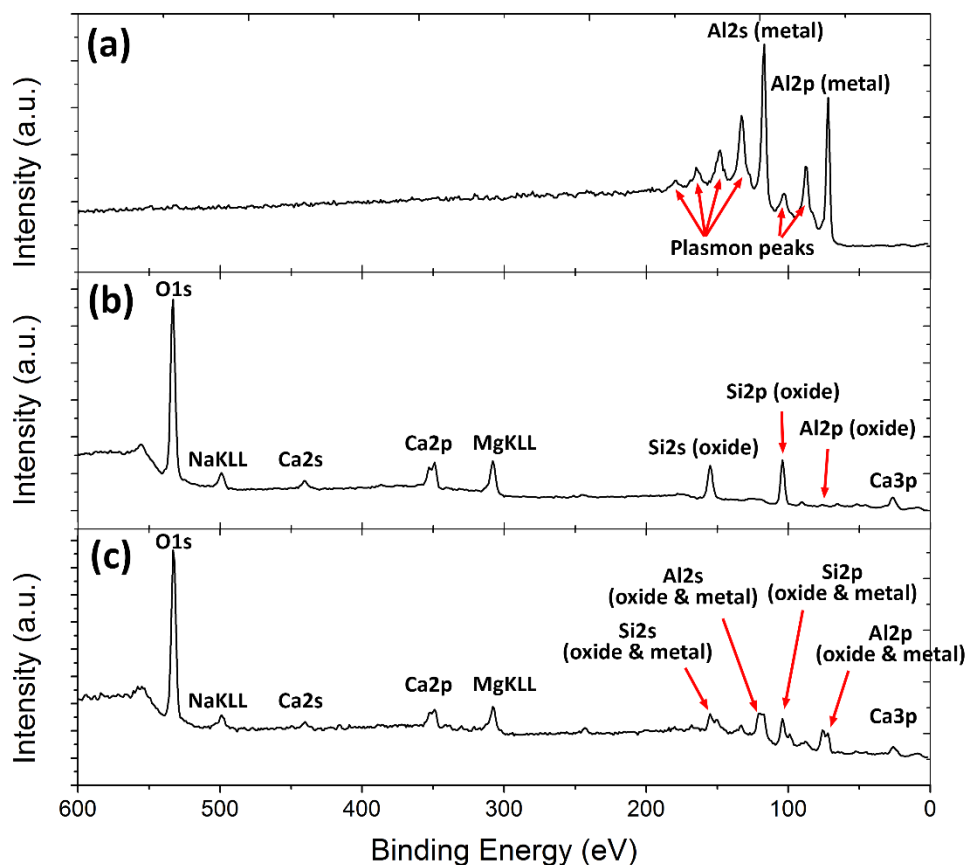
Figure 94. Survey scans of (a) deposited Al film and (b) soda-lime glass and (c) 10 min. annealed sample by XPS.

Table 15. Identification of peaks in deposited Al film presented in Figure 94(a) with related references and identified peak positions in the literature

Peak P. (eV)	Element & Spec. Line	Identification	Reported Peak Position (eV)
72	Al2p	Al	72.2 [133], 73.0 [134]
88	Al2p	1st plasmon satellite peak of metallic Al2p	15 eV [135] or 15.5 eV [136] lower than observed Al2p binding energy
103	Al2p	2nd plasmon satellite peak of metallic Al2p	30 eV [135] lower than observed Al2p binding energy
117	Al2s	Al	117.9 [137], 117.7 [138], 118.0 [139][134]
133	Al2s	1st plasmon satellite peak of metallic Al2s	16 eV [134], [140] lower than observed Al2s binding energy

Table 15 (continuous). Identification of peaks in deposited Al film presented in Figure 94(a) with related references and identified peak positions in the literature

Peak P. (eV)	Element & Spec. Line	Identification	Reported Peak Position (eV)
148	Al2s	2nd plasmon satellite peak of metallic Al2s	32 eV [140] lower than observed Al2s binding energy
165	A2s	3rd plasmon satellite peak of metallic Al2s	49 eV [140] lower than observed Al2s binding energy
180	Al2s	4th plasmon satellite peak of metallic Al2s	64 eV [140] lower than observed Al2s binding energy

Table 16. Identification of peaks in glass presented in Figure 94(b) with related references and identified peak positions in the literature

Peak Position (eV)	Element & Spectral Line	Identification	Reported Peak Position (eV)
27	Ca3p	CaO	27 eV [141], 26.2 eV [142]
75	Al2p	Al_2O_3	74.4 eV [143], 73.8 eV [144], 74.7 eV [145], 75.6 eV [146]
104	Si2p	SiO_2	103 eV [147], 103.5 eV [148], 103.6 eV [134]
155	Si2s	SiO_2	155 eV [134], 154.8 eV [149], 155.3 eV [150]
308	MgKLL	MgO	307.5 eV [151]
349	Ca2p	CaO	347.6 eV [152], 347.1 eV [142], 349.30 eV [153]
441	Ca2s	CaO	440 [134]
499	NaKLL	Na_2O	496.9 eV [154], 497 eV [134]
		Al_2O_3	531 eV [134], 531.3 eV [143]
		SiO_2	533 eV [148], 533,7 eV [150]
533	O1s	Na_2O	529.7 eV [134]
		CaO	531.3 eV [134], 529.9 eV [142]
		MgO	530.0 eV, 531.2 eV, 532.1 eV [134]

Following 10 minutes of annealing, the XPS spectra suggests an intermixing of components, as shown in Figure 94(c); photoelectron peaks of Al, Si, O, Na, Ca and Mg can all be identified in a single spectrum. There are double peaks for the binding energies of Si and Al as given in Table 17. Si2p peak appears at 99 eV and 104 eV, the former belongs to elemental forms of Si while the latter represents Si binding energy in SiO_2 form. In addition, Al2p peak arises at 72 eV and 75 eV. The 3 eV binding energy different corresponds to oxidation of Al in the form of Al_2O_3. However, in other components of the glass, which are CaO, MgO, Na_2O, any change in the oxidation states could not identified in survey scan due to low intensity of the signal. In 10 min annealed sample, Ca2p (2p3/2) peak appears at 349 eV, MgKLL peak at 308 and NaKLL peak at 499 eV.

Table 17. Identification of peaks in 10 min. annealed sample given in Figure 94(c) with related references and identified peak positions in the literature.

Peak Position (eV)	Element & Spectral Line	Identification	Reported Peak Position (eV)
72	Al2p	Al	72.2 [133], 73.0 [134]
75	Al2p	Al_2O_3	74.4 eV [143], 73.8 eV [144], 74.7 eV [145], 75.6 eV [146]
99	Si2p	Si	99.0 eV [134]
104	Si2p	SiO_2	103 eV [147], 103.5 eV [148], 103.6 eV [134]
118	Al2s	Al	117.9 [137], 117.7 [138], 118.0 [139][134]
121	Al2s	Al_2O_3	119.3 eV [155], 121.20 eV [146]
151	Si2s	Si	151 eV [134]
155	Si2s	SiO_2	155 eV [134], 154.8 eV [149], 155.3 eV [150]

In order to acquire a deeper understanding of the chemical changes that occur during annealing, high resolution XPS spectra from each element was collected for 130 nm Al coated samples. In Figure 95, photoelectron spectra of Al for different

depths and different annealing durations are presented. For non-annealed sample, presented in Figure 95(a), the film is elemental Al, in which Al2p appears at 72 eV binding energy. There is a peak in the 20th and 30th layers which is corresponding binding energy of Al in Al_2O_3 structure which presents inside the soda-lime glass. After 7 minutes of annealing, there is significant amount of elemental Al present with a broad Al_2O_3 peak as shown in Figure 95(b). When annealing time is increased to 15 minutes, on the other hand, it is observed that the film is composing of Al_2O_3 mostly, which is presented in Figure 95(c). After 40 minutes of annealing, the reaction is completed [Figure 95(d)]. There is a small amount of elemental Al in this sample but there is no further change is observed when annealing time is increased to 60 minutes for 130 nm Al coated sample.
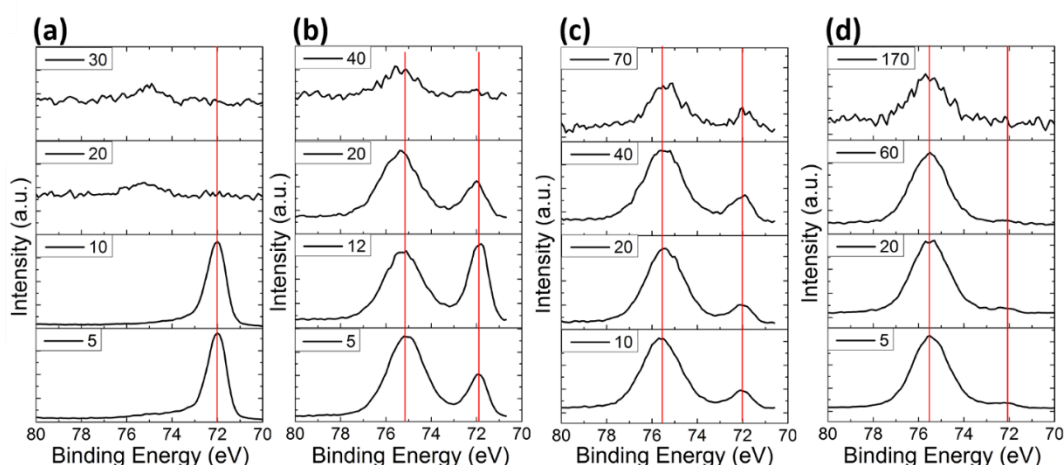
Figure 95. Binding energy of Al from different depths for samples; (a) non-annelaed, (b) annealed for 7 min., (c) annealed for 15 min. and (d) annealed for 40 min. Number for each graph represents layer that the scan is taken.

When we look at binding energies of Si from different depths, a scenario parallel with the case of Al can be seen as presented in Figure 96. In Figure 96(a), the signal appears at 103 eV for 5th and 10th layers belongs to second plasmon satellite peak of elemental Al coming from metallic Al film. After 7 minutes of annealing, elemental Si is formed inside the film, which can be seen in Figure 96(b). It can be seen clearly in 15 min. annealed sample that both elemental Si and SiO_2 can be present

in the same layer as given in Figure 96(c). This indicates non-uniform reaction rate coming from solid phase and liquid phase difference. The Si binding energy distribution in 40 min. annealed sample can be seen in Figure 96(d). As the redox reaction progresses, more c-Si is formed near the surface, as evidenced by the distinct elemental Si peaks on 5th and 20th layers.
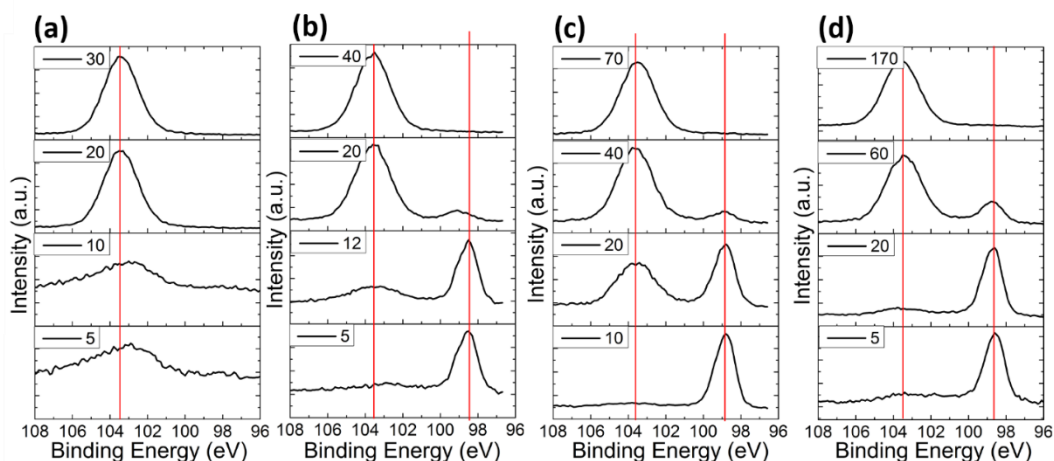
Figure 96. Binding energy of Si2p after different number of sputtering cycles for samples (a) non-annealed, (b) annealed for 7 min., (c) annealed for 15 min. and (d) annealed for 40 min. Number for each graph represents layer which the scan is taken.

When other components of soda-lime glass is investigated, it is seen that Na, Ca and Mg are diffused through the film and especially Na is accumulated on the surface as shown in Figure 97. For this analysis, binding energies for Ca2p, Mg2p and Na1s are investigated. Binding energies of Ca and Mg appears at 348.10 eV and 50.80 eV for Ca2p (2p3/2) and Mg2p peak correspondingly, which are belongs to binding energy of Ca in CaO [142], [152], [153] and Mg in MgO [153]. There is no chemical reduction of Ca and Mg as suggested in the literature [156]. However, it is observed that significant amount of Na has diffused to the surface and binding energy is shifted to lower binding energy on the surficial layers. The binding energy of Na in the glass for Na1s peak is measured as 1073.10 eV. On the surface of the annealed film, on the other hand, peak position of Na1s shifts to 1071.50 eV that is defined as elemental Na [134]. Oxidation potential of Al is higher than Na, which explains existence of

elemental Na on the surface [157], [158]. The accumulation seen in the XPS graphs, presented in Figure 97(d), of the elemental Na is also observed by SEM and EDX as given in Figure 98.Na-rich regions appear on top of Si rich regions. However, when annealing time is increased more such as up to 240 minutes, the accumulation of Na on non-Si rich regions can be also observed as seen in Figure 99. Even though redox reaction finalized, the alkaline and earth alkaline metals from the glass continue to diffuse.
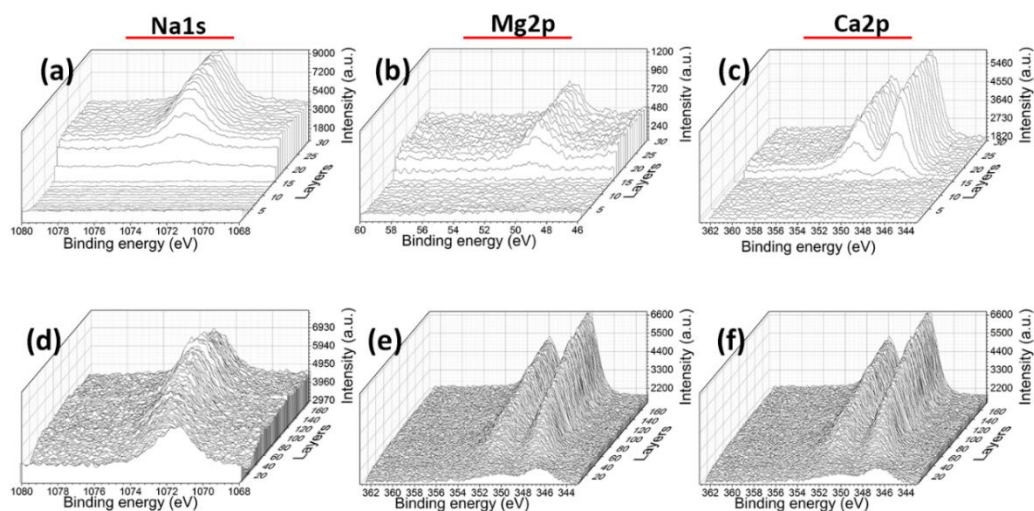
Figure 97. XPS depth profiles of non-annealed; (a) Na1s, (b) Mg2p, (c) Ca2p; and fully annealed (40 min.) Samples; (d) Na1s, (e) Mg2p, (f) Ca2p
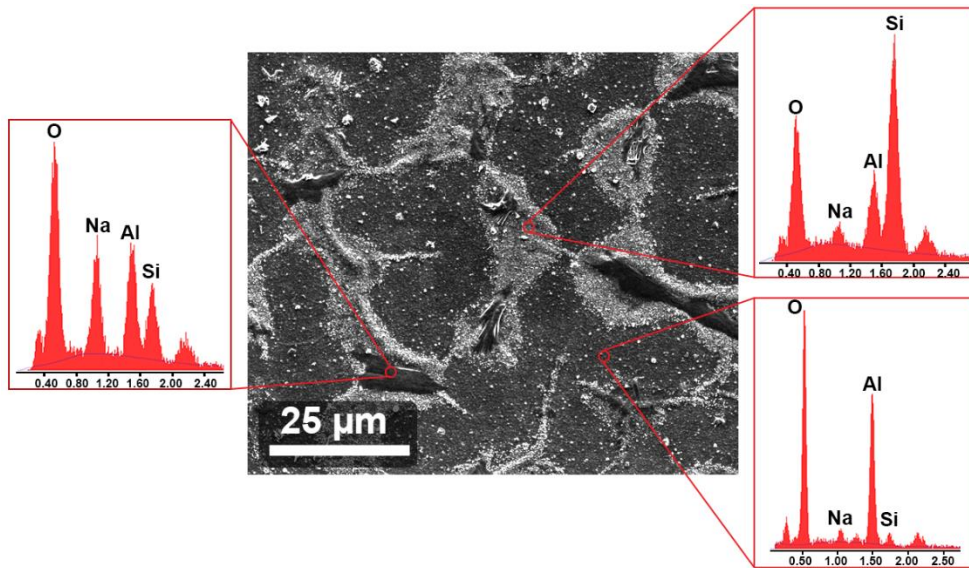
Figure 98. SEM image (x2500 mag.) showing Na reach regions with EDX measurements
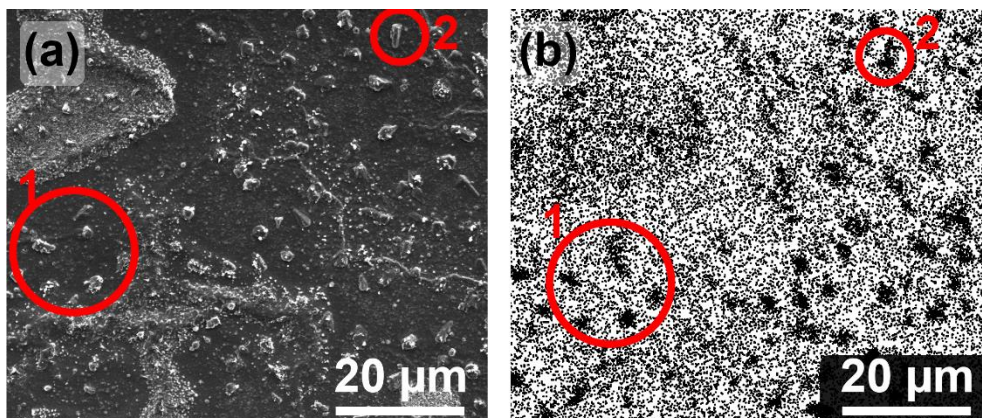
Figure 99. Comparison of (a) SEM image and (b) EDX map of Na, which is showing accumulation of Na on the surface for 240 min. of annealing. Numbered circles indicates accumulated Na on both EDX Map and SEM image.

4.4.3. Structural Evolution of Al/Glass Interface During Annealing and Its Impact on Texturing

Structural, morphological, and optical characterization of the samples were made before and after etching. The morphology and the elemental distribution of the annealed film was investigated by an optical microscope and FE-SEM coupled with

EDX. The structural and compositional evolution of the over-layer was studied by Raman spectroscope. After texturing of samples, optical measurements were conducted with an integrating sphere and topographical characterization with SEM and atomic force microscope.

The optic microscope (OM) images and corresponding Raman spectra obtained from samples annealed at 550 °C for 90 and 120 min (550_090 and 550_120, respectively) are given in Figure 100(a) through Figure 100(f). The OM image of the 550_090 sample shows a high contrast Al background darker, micrometer sized spots dispersed on the surface as seen in previous study discussed in the section, 4.4.2. XPS Study on Annealing Effect for Al/Glass Interface During AIT. In addition, agglomerate-like features with low contrast can be observed, as seen in the center of the higher magnification image given in Figure 100(b) (taken by the built-in optical microscope of the Raman spectroscope). The laser beam of the tool was focused on the agglomerate-like feature, and Raman spectra was obtained that is shown in Figure 100(c). The Raman peak near 521 cm^{-1} is distinguishable, which corresponds to crystalline Si. Accordingly, it appears that nucleation of the reduced Si has already begun at 90 min, and the dark features in the optical microscope image are Si precipitates. The optical images for the 550_120 sample [Figure 100(d) and Figure 100(e)] show that the precipitates further grow into dendritic structures with a distinct crystalline Si Raman peak, as shown in Figure 100(f). In addition, these crystals gives a peak at 28.4° that corresponds to crystalline silicon with (111) orientation as identified in powder diffraction file of Si [159]. To investigate on the compositional distribution of the annealed samples, EDX mapping was carried out for silicon, oxygen and aluminum.
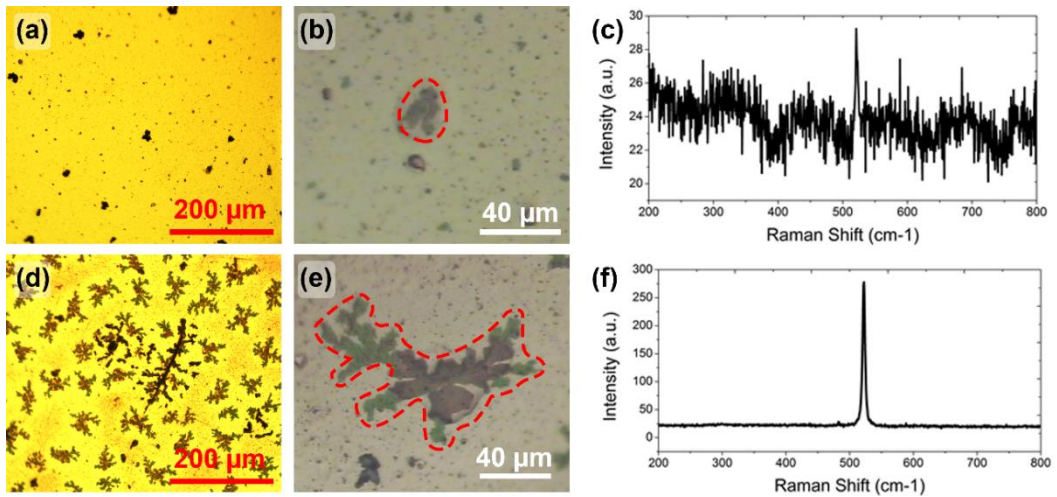
Figure 100. (a) OM of 550_090, (b) image from built-in optical microscope of Raman spectroscope of 550_090, (c) Raman spectra of 550_090, (d) OM of 550_120, (e) image from built-in optical microscope of Raman spectroscope of 550_120, (f) Raman spectra of 550_120.
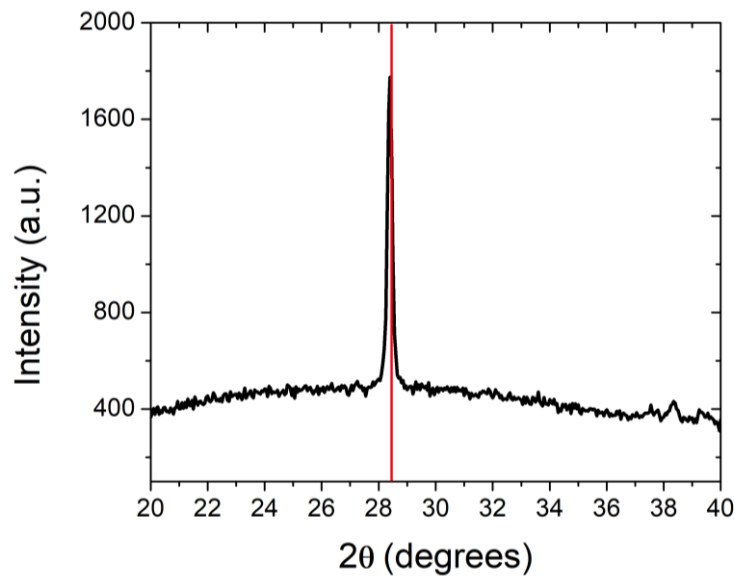
Figure 101. XRD pattern of 550_600. Red line shows (111) Si peak at 28.4° given in the PDF file.

Figure 102(a) and Figure 102(b) shows EDX maps taken from samples 550_120 and 550_300, along with their respective secondary electron (SE) images. The brightness of the color is proportional to the signal intensity obtained from its respective element. A distinct compositional separation is noticeable on the 550_120

sample, where the dendritic Si islands are enclosed by a mixture of Al and O as given in Figure 102(a). In the near-vicinity of the Si dendrites Al signal is particularly bright, whereas the O map reveals very low contrast. The high contrast Al regions are considered to be metallic Al, while the surrounding area is aluminum oxide. In Figure 102(b), EDX map of Si, O and Al for 550_300 is given with corresponding SEM image. In this sample, Si dendrites appear to have grown into a more equiaxed morphology and no metallic Al is present near them.
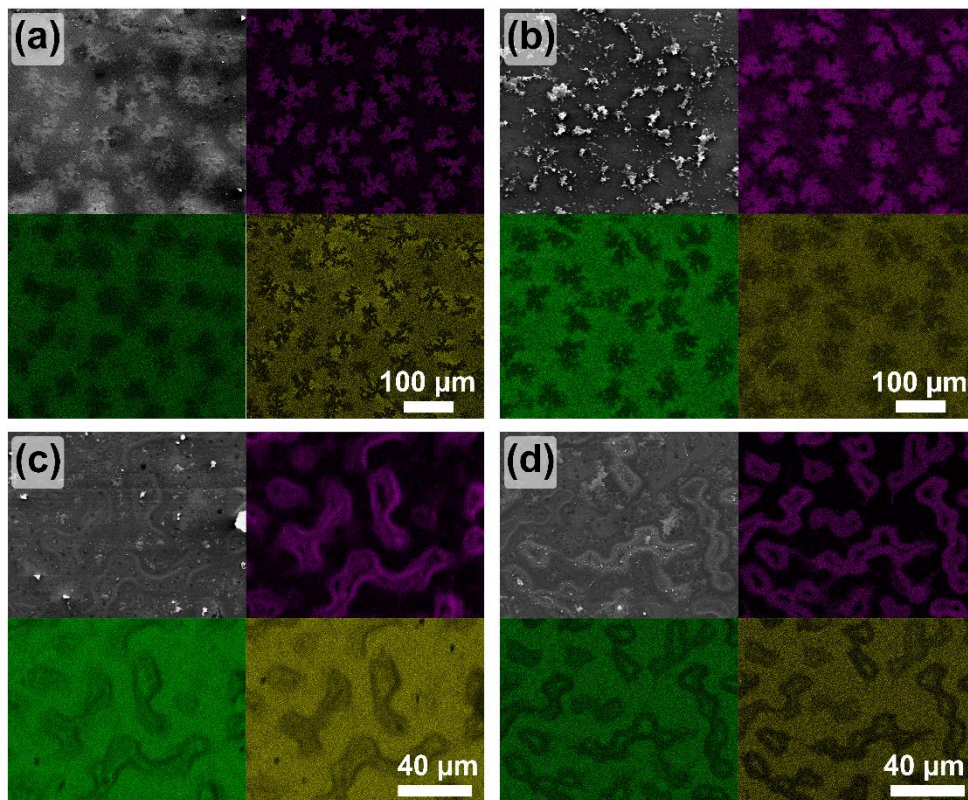
Figure 102. EDX mapping for (a) 550_120, (b) 550_300, (c) 575_105 and (d) 600_060. Secondary electron image (top left) and maps of Si (top right), O (bottom left) and Al (bottom right).
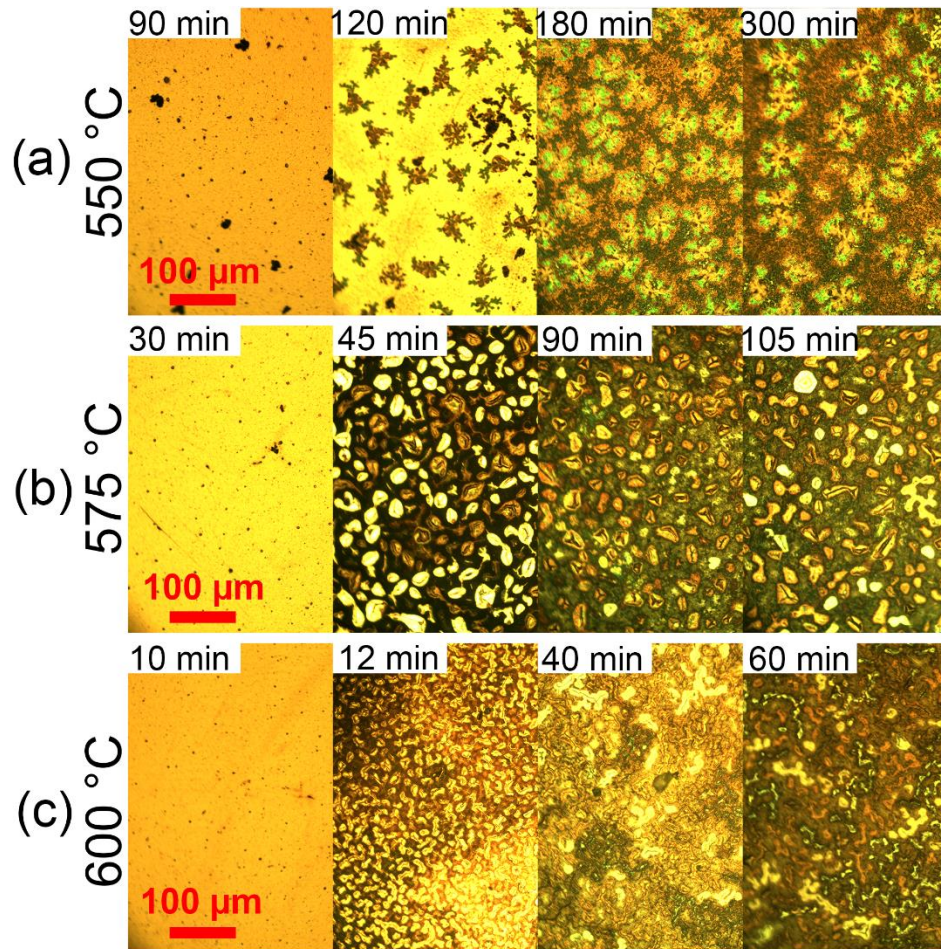
Figure 103. Optical images of annealed samples with varying durations at a temperature of a) 550 °C, b) 575 °C, c) 600 °C. All images are obtained using reflected light.

The evolution of the surface morphology during 550 °C annealing can be monitored by the optic microscope images taken from samples annealed for varying times, as shown in Figure 103(a). The dendritic Si crystals reach their final structure between 120 and 180 min. of annealing, and further annealing up to 300 min. does not produce a significant effect. For the 550_120 sample, the dendritic structures yield low contrast, while for longer annealing times, they appear bright and the surrounding area have a brownish color. This discrepancy is likely due to the reduction in the amount of reflected light from the oxidized Al background, which results in the change in the relative contrast between the dendrites and the background. When the OM images of the 550 °C annealed samples are compared to those of 575 °C [Figure 103(b)] and 600

°C [Figure 103(c)], a drastic difference in the morphology of the surface feature can be seen. At 575 °C and 600 °C annealing, circular features are visible instead of Si dendrites at the early stages of annealing. Upon further annealing, these structures coalesce into unidirectional, "peanut-shell" shaped features (we will refer to these features as "peanuts" for the rest of the text). These features appear smaller for the samples annealed at 600 °C compared to those annealed at 575 °C. Figure 103 also shows that the necessary annealing time to complete the reaction reduced significantly with increasing annealing temperature.

Figure 102(c) and Figure 102(d) lists the SEM images and EDX maps (Si, O, Al) for samples annealed at 575 and 600 °C, respectively. The annealing durations were chosen to ensure that the process reached completion (i.e., all of the Al has been oxidized) for each sample. It is noticeable that the peanut-like structures formed at 575 and 600 °C are not compositionally uniform; Si-rich regions are located at the periphery, and a high concentration of Al and O is detectable inside of these features. The separation is particularly distinguishable for the sample annealed at 600 °C as shown in Figure 102(d).

Following the annealing runs, the samples were chemically etched by an alkaline solution to remove the reactions products, and the texture of the bare glass samples were investigated via SEM. Figure 104 shows SEM images with varying magnification and viewing angles, taken from samples representing different stages of annealing at 550 °C. At 90 min. depressions ("craters") up to 2 µm diameter are distributed on the flat glass surface [Figure 104(a)]. After 120 min. of annealing, the crater density have increased significantly, while flat areas can still be detected, as shown in Figure 104(b). The craters coalesced into larger groups, forming a foam-like network on the surface. At the end of 300 min. [Figure 104(c)] the surface is completely textured. The flat zones observed for sample 550_120 appear to be textured in 550_300, albeit with a smaller crater size compared to their surroundings.
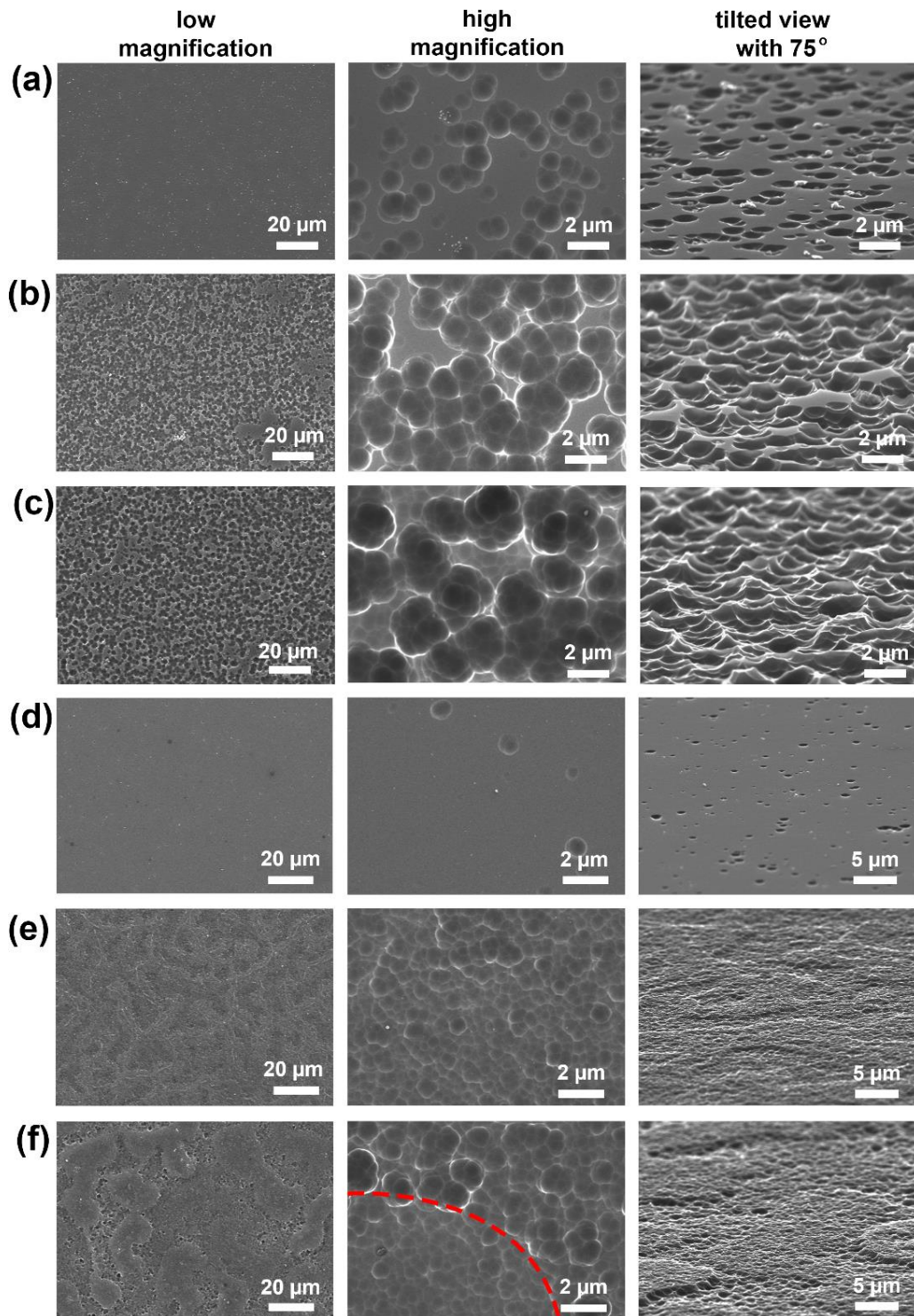
Figure 104. SEM images of samples after etching. (a) 550_090, (b) 550_120, (c) 550_300, (d) 600_010, (e) 600_030, and (f) 600_060. Left column shows low magnification image, middle high magnification image, and right column tilted view for each temperature.
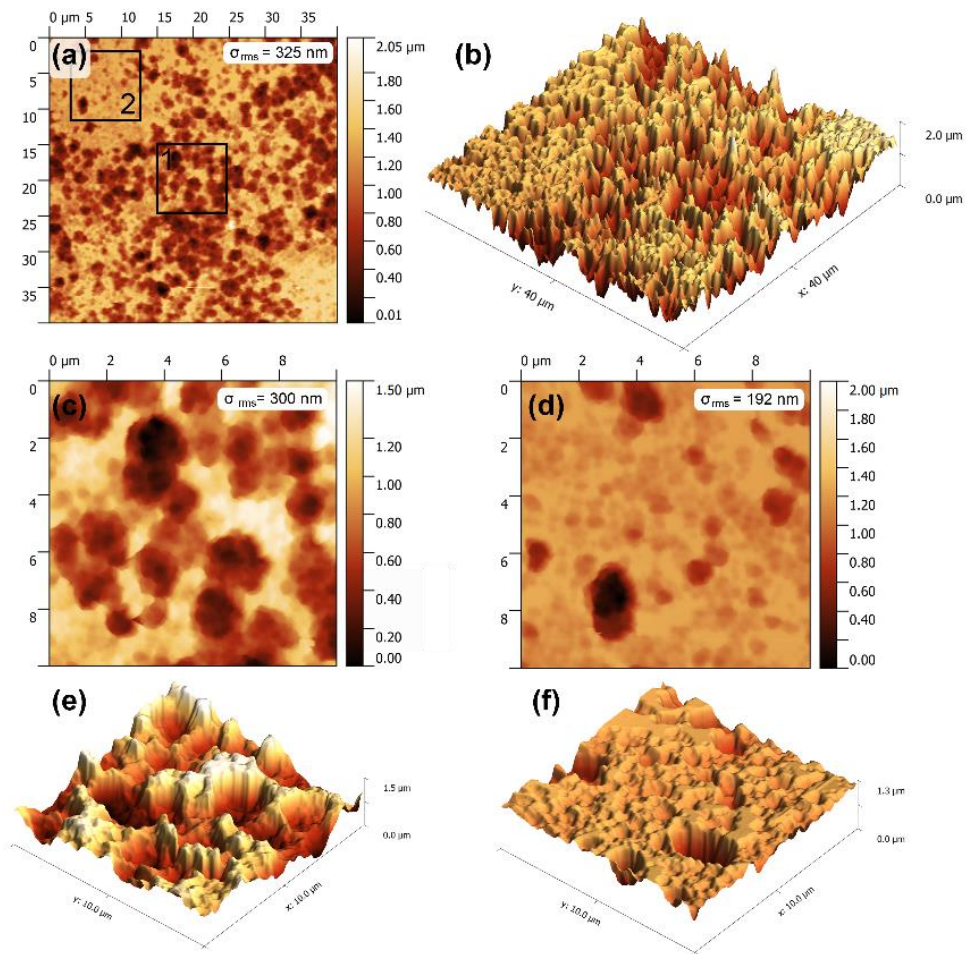
Figure 105. AFM images of sample 550_300. (a) 2D image with 40 μm x 40 μm scan area (b) 3D image with 40 μm x 40 μm scan area, (c) 2D image with 10 μm x 10 μm scan area of the place indicated as "1" in the image with 40 μm² scan area (d) 2D image with 10 μm x 10 μm scan area of the place indicated as "2" in the image with 40 μm² scan area, (e) 3D image of "1" with 10 μm x 10 μm scan area and (f) 3D image of "2" with 10 μm x 10 μm scan area.

The bare glass surfaces from the samples annealed at 575 °C and 600 °C were quite similar to each other, therefore, only the SEM images of the latter is presented. Figure 104(d) shows secondary electron micrographs obtained from the sample annealed at 600 °C for 10 min. Craters with a diameter of 1 μm or less can be seen randomly distributed on the glass surface. At 30 min of annealing, the surface is fully covered with craters, a pattern can be seen due to the contrast difference in the plan view images [Figure 104(e)]. The pattern resembles the peanut-like shapes shown Figure 102(d). The 75° tilted view reveals that the observed contrast in the plan view images is due

to a height difference between adjacent regions. After 60 min. of annealing, the peanut-like features appear larger, and the height difference is more pronounced [Figure 104(f)]. It can also be noted that the craters on these features appear to be smaller than those on the surrounding areas.

Figure 105 shows 2D and 3D AFM images of 550_300 with 40 µm x 40 µm and 10 µm x 10 µm scan areas. The surface roughness (σ_{rms}) for measurement with 40 µm^2 scan area is 325 nm [Figure 105(a)]. In both 2D and 3D AFM image of 550_300, Figure 105(a) and Figure 105(b), there are relatively flat areas on the surface. Highly textured area is numbered with "1" while relatively flat area numbered with "2". When 10 µm x 10 µm images taken from these two areas are compared it can be seen that in area "1" there are deep craters (with diameter approximately 2 µm) and the surface roughness is 300 nm as given in Figure 105(c). On the other hand, in the area "2" at Figure 105(d), there are a few deep craters which are predominantly made up of shallow craters with the surface roughness, 192 nm as given in Figure 105(d). The difference between these two areas can be seen clearly in 3D AFM images given in Figure 105(e) and Figure 105(f).
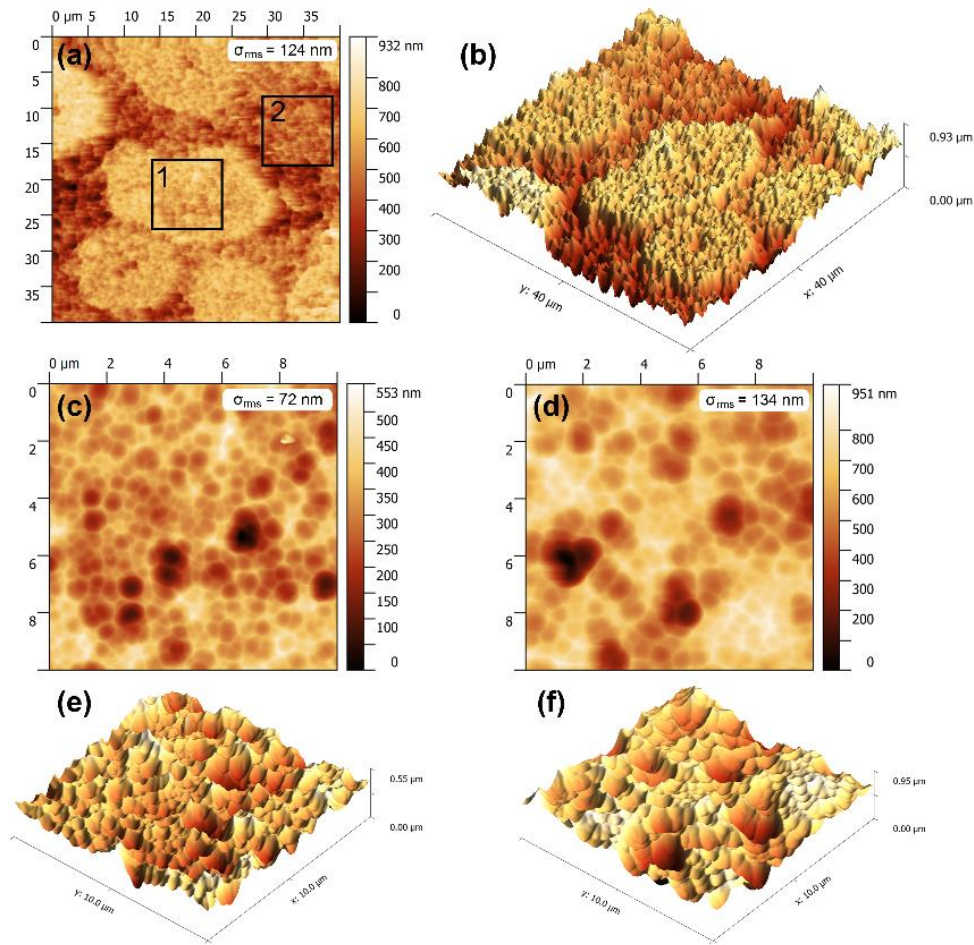
Figure 106. AFM images of 600_060. (a) 2D image with 40 µm x 40 µm scan area (b) 3D image with 40 µm x 40 µm scan area, (c) 2D image with 10 µm x 10 µm scan area of the place indicated as "1" in the image with 40 µm² scan area (d) 2D image with 10 µm x 10 µm scan area of the place indicated as "2" in the image with 40 µm² scan area, (e) 3D image of "1" with 10 µm x 10 µm scan area and (f) 3D image of "2" with 10 µm x 10 µm scan area.

On the other hand, in Figure 106, 2D and 3D AFM images of 600_060 with 40 µm x 40 µm and 10 µm x 10 µm scan areas are given. The surface roughness (σ_{rms}) for measurement with 40 µm² scan area [Figure 106(a)] is 124 nm. The peanut-like features observed by other imaging techniques above can also be seen in the wide area scans [Figure 106(a) and Figure 106(b)]. These areas are elevated from the surface by approximately 500 nm. When the surface of this elevated area is investigated [Figure 106(c)], it is seen that the surface craters have diameter smaller than 500 nm resulting in a local roughness of 72 nm. However, on the surrounding area [Figure 106(d)], the

craters are larger (>700 nm) and the surface roughness is considerably higher (134 nm). The difference between two surface can be compared in Figure 106(e) and Figure 106(f) with 3D images.

To compare the optical properties of the textured samples annealed at different temperatures, total transmittance and haze (ratio of the diffused transmittance to total transmittance) measurements were carried out by integrated sphere spectrometer on reverse configuration. The light was sent through the textured side and the integrated sphere was placed behind, facing the flat side of the sample. All samples were "fully annealed", i.e., further annealing did not produce a change in the surface morphology (since temperature uniformities were observed for the 30 mm x 30 mm sample annealed at 550 °C, the annealing duration was chosen as 600 min to ensure the process was completed across the sample surface). The % transmittance values distributed between wavelengths of 400 nm and 1100 nm were similar for all AIT samples as well as samples Ref1 and Ref2, as shown in Figure 107(a). Transmittance of the 550_600 sample appeared several percentage points (pp) higher than the rest of the samples. The haze values from representative AIT and reference samples are given in Figure 107(b). As expected, diffused transmittance for the non-textured Ref1 and Ref2 is negligible, while considerable haze was observed for the AIT samples at all wavelengths measured. Among these, the 550_600 sample showed significantly more haze than its 575 and 600 °C counterparts (between 20 to 40 pp, depending on the wavelength of the incoming light).
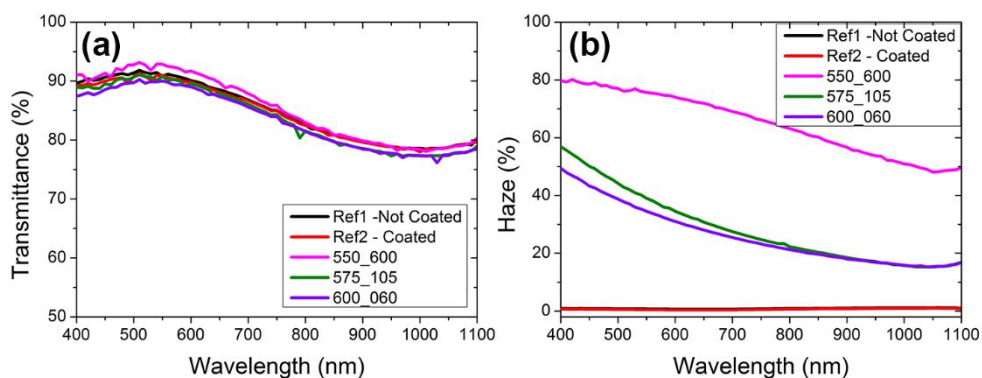
Figure 107. (a) Transmittance and (b) haze of samples annealed at different temperatures and durations with 2 reference sample.

The observations from the annealing experiments at different temperatures are presented separately above to form a picture about changes during annealing. Several commonalities exist amongst all temperatures examined. At the onset of annealing, micron-scale Al_2O_3 nodules are distributed on the surface (Figure 103, leftmost column), which, after chemical etching, manifest themselves as craters with several µm diameters (Figure 104, top row). As the annealing continues, distinct features appear on the surface, consisting (at least partially) of crystalline Si [Figure 100(a) through Figure 100(f)]. The process continues until no available metallic Al is present at the glass surface. These observations are well in accord with the AIT model presented by Huang et. al. [108].

However, the morphology of the Si-rich regions show considerable variation based on annealing temperature, and indicates a fundamental difference in the crystallization of Si. Whereas the Si crystals grow into a distinctly dendritic shape at 550 °C [Figure 102(a)], they form as a layer around the edges of Al-oxide structures at and above 575 °C [Figure 102(c) and Figure 102(d)]. In an attempt to explain this apparent discrepancy, we make two assumptions to simplify the materials system:

Glass is assumed to be composed solely of SiO_2, while the effect of other components (alkali oxides, etc.) is ignored.

We consider SiO_2 and Al_2O_3 to be chemically inert and neglect the effect of oxygen (considering the minute solubility of O in Al and Si at the temperatures of concern [160], [161]).

The problem can then be reduced to an isothermal Al-Si system where the composition of Si with respect to Al is increasing with time (as the redox reaction progresses). As such, we can refer to the Al-Si phase diagram (Figure 108) and discuss the possible crystallization mechanisms for the low temperature (550 °C) and high temperature (600 °C) processes separately.

At the beginning of annealing the system consists solely of Al. As the reaction ensues, the chemically reduced Si dissolves in Al and its composition w.r.t. Al increases rapidly, as indicated by the blue (550 °C) and green (600 °C) arrows in Figure 108. At 550 °C, as the concentration of Si exceeds the solubility limit (approximately

126

1.1%) nucleation occurs, forming Si crystallites within the solid Al. The location of the available Al is dictated by the network of Al_2O_3 particles at this stage. The process resembles the nucleation and growth mechanisms observed for Al induced crystallization, where the Al-grain boundaries and Al-oxide surface act as preferential nucleation sites for Si [162]–[168]. Originally closer to a circular shape [Figure 100(a) and Figure 100(b)], the crystallites respond to local fluctuations of Si concentration in the surrounding Al and grow into a dendritic form [169] [Figure 100(d) and Figure 100(e)]. As the Al_2O_3 growth compete with that of the Si dendrites for lateral space, the expansion of the latter is restricted within the available Al. The restriction can easily be observed by comparing Figure 109(a) and Figure 109(b), where the EDX maps presented in Figure 102(a) and Figure 102(b) are overlaid to show the composition near the Si dendrites for samples annealed at 550 °C for 120 and 300 min., respectively. At 120 min. regions rich in Al (i.e., poor in oxygen) are visible, particularly in between the "branches" of the Si-dendrites, while the background is predominantly of Al_2O_3 [Figure 109(a)]. As the growth is confined into the Al, the Si crystals become more compact in shape, while the effective radii (approximately 50 μm) does not change appreciably at 300 min. of annealing [Figure 109(b)]. Our explanation of the processes that occur at 550 °C is based on the work published by Huang et. al., which investigated the AIT process at 570 °C and observed the formation of dendritic Si [108], very similar to those shown in the present study.
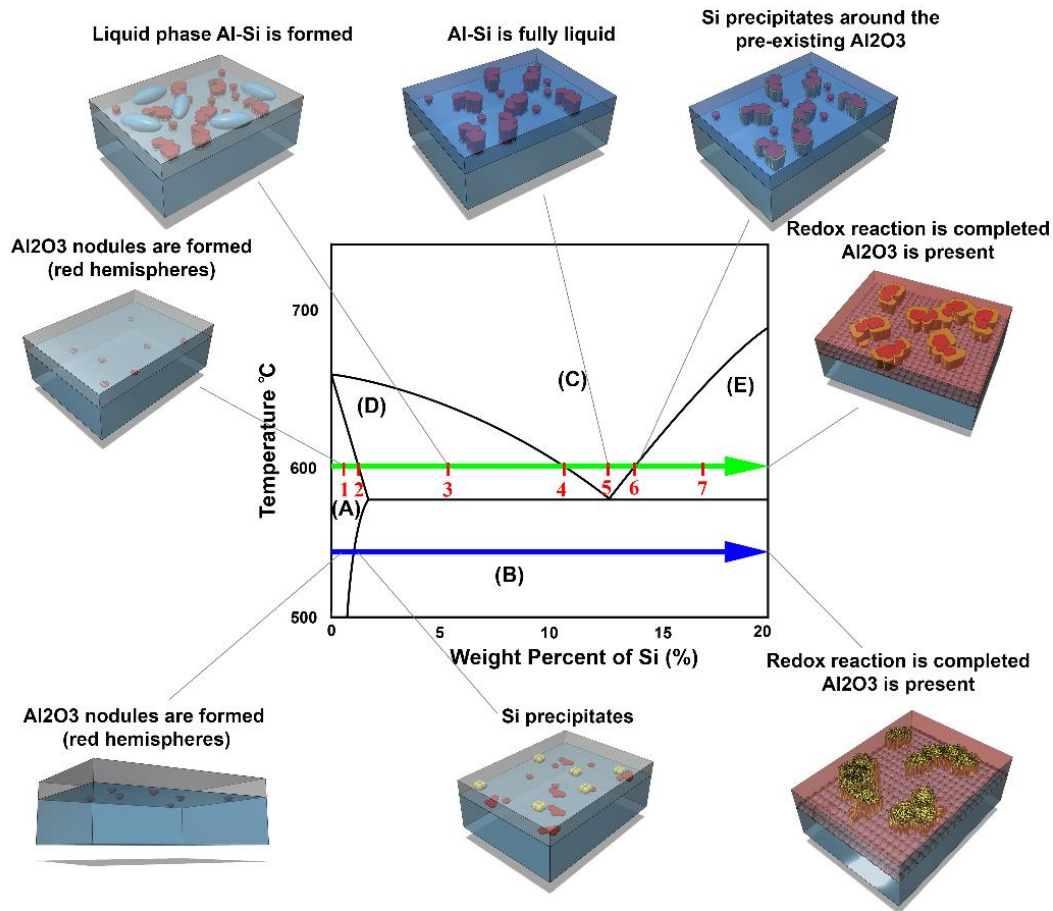
Figure 108. Al-Si phase diagram with sketches illustrating the evolution of the film and interface morphology. Phase regions are defined as (A) α-Al (<1.3% Si), (B) α-Al + Si, (C) Liquid Al (~11-14% Si), (D) α-Al (<1.3% Si) + Liquid Al (~11% Si) and (E) Liquid Al (~14% Si) + Si (~100% Si).
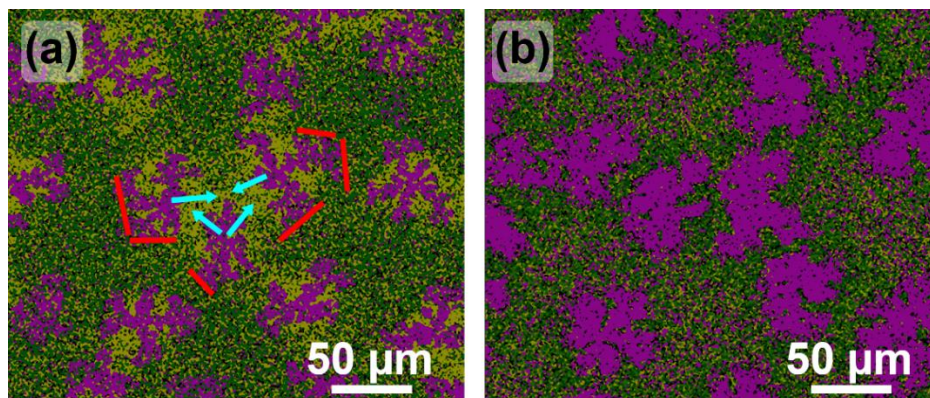
Figure 109. Overlaid Si, Al, and O EDX maps of (a) 550_120 and (b) 550_300. The turquoise arrows indicate the direction that Si dendrites are allowed to grow, while the red lines suggest where growth is restricted.

The annealing process at 600 °C commences similarly to that at 550 °C: The Si produced in the redox reaction is dissolved in Al ("#1", as labelled in Figure 108), forming a solid solution, until the concentration of Si in Al exceeds the solubility limit (#2, approximately 1.3%). Beyond this point (#3), addition of Si into the system results in the formation of a liquid Al-Si phase (with a Si concentration of approximately 11.0%) within the saturated Al solid phase (Si concentration of approximately 1.3%). The fraction of the liquid phase increases as Si is introduced (and Al is removed) until the system is fully liquid at an overall Si concentration of 11.0% (#4). The system stays as a single liquid phase (#5), until the Si concentration reaches ~14.0% (#6), after which the nucleation of Si is initiated (#7). The Si precipitates continue to grow until there is no available Al left to sustain the redox reaction at the glass surface. Using this model, we can then explain the structural formation of crystal Si as follows: At #2, Si saturated Al phase is present, wherein Al_2O_3 particles are dispersed randomly. Upon the formation of the liquid phase, the rate of redox reaction at the liquid/glass interface increases drastically due to enhanced transport mechanism. This results in a positive feedback loop where the increase in the amount of liquid phase increases the production of Si, and vice versa. This cascading reaction kinetics is apparent in OM images presented in Figure 110, where a sudden change in morphology between 11 minutes and 12 minutes of annealing can be seen. The Si concentration rapidly reaches past #6, and precipitation begins. The Al_2O_3 surface acts as a highly preferential nucleation site for Si, which wraps around the Al_2O_3 regions to form the structures seen in Figure 102(b). A similar phenomenon where Si segregation on Al_2O_3 was observed for the cooling of eutectic Al-Si mixture in a previous study [170].
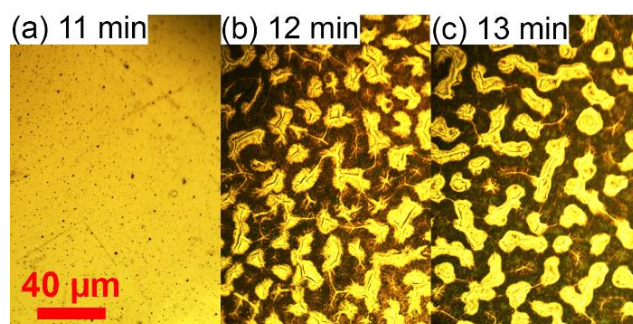
Figure 110. Optical microscope images of (a) 600_011, (b) 600_012 and (c) 600_013.

As understood from the present study as well as those carried out previously [108], the fundamental texturing mechanism of AIT formation of Al_2O_3 particles and their expansion into the glass, which manifest themselves as micro-craters on the glass surface after removing of the over-layer by chemical etching. On the other hand, the simultaneous production of elemental Si results in processes that affect the crater formation depending on the temperature at which the annealing is carried out.

As the precipitates grow, they act as a diffusion barrier between Al and glass, hindering the redox reaction. This is apparent in Figure 111(a) and Figure 111(b), where the Si-EDX map from the Al over-layer of the 550_120 sample (prior to chemical etching) is compared to the SE micrograph of the same sample after etching as well as in AFM images in Figure 105. Relatively flat regions with shapes that resemble the Si dendrites are clearly visible on the etched glass. The lateral size of the flat zones appears to be smaller compared that of the Si dendrites, possibly indicating that the growth of Si extends onto the Al_2O_3 particles during the later stages of annealing.

A more complex phenomenon is observed at 600 °C, which is well above the Al-Si eutectic temperature, which is 577 °C [171]–[175] . The increase in the Si concentration in Al promotes the formation of a liquid phase. Where the liquid phase is in contact with the glass, the rate of the redox reaction is significantly enhanced, therefore, a more rigorous etching pattern is expected. In Figure 111(c) and Figure 111(d), it is seen that the shape of peanut-like structures seen during annealing are imprinted on the glass surface as distinct regions following the chemical etching of the over-layer. These regions have a lower crater-size distribution and appear to be elevated by 500 nm compared to their surroundings [Figure 104(f), Figure 106(a) and Figure 106(b)]. The peanut-like structures were formed during the initial phase of annealing, while the Al was solid, and were subsequently enclosed by Si upon its precipitation. As such, the glass under these regions were kept from interacting with liquid Al, thus have a lighter etch pattern.

It is worthwhile to mention that the AIT experiments carried out at 575 °C and 600 °C appear very similar, indicating the formation of a liquid Al-Si phase in both cases. Considering that the eutectic temperature of the pure Al-Si system is 577 °C, texturing

130

at 575 °C would be expected to occur in solid phase only, similar to 550 °C. This is likely an indication that the additional elements introduced through the glass (Na, Mg etc.) resulted in a decrease in the eutectic temperature of the system, as suggested by previous studies that reveal such a modification of the Al-Si system [173], [175], [176].
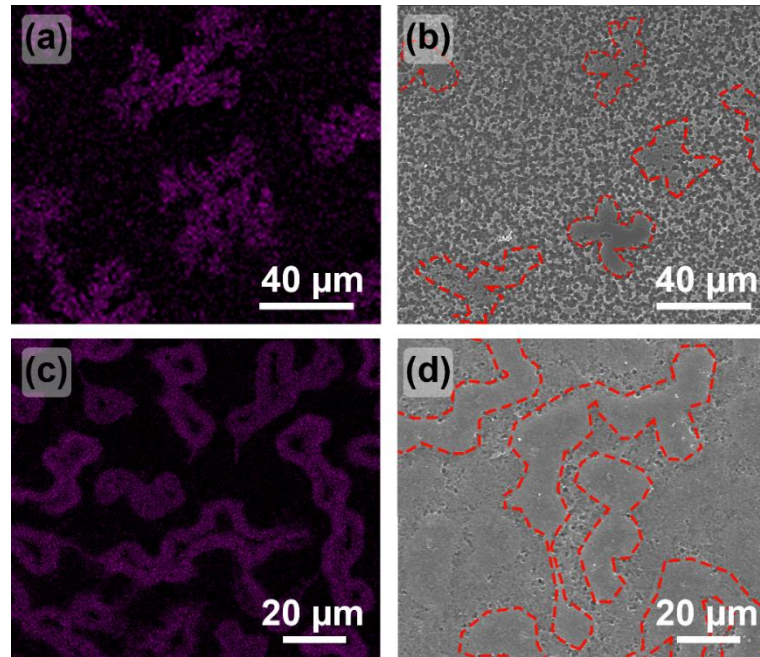
Figure 111. Comparison of EDX map of Si with textured surface. (a) EDX map of Si belongs to 550_120, (b) SEM image of 550_120 after etching. (c) EDX map of Si belongs to 600_060 and (d) SEM image of 600_060 after etching process. Plateaus are circled with red dashes.

Optical measurements given in Figure 107(a) and Figure 107(b) show that the diffused transmittance in sample annealed at 550 °C is greatly enhanced compared to its counterparts annealed at higher temperatures. The haze is approximately 20 pp higher at low wavelengths (near 400 nm) for the former, and the difference reaches up to 40 pp at higher wavelengths (near 1100 nm). This significant difference in haze can be correlated to the difference in surface texture of samples annealed only in solid phase (i.e., at 550 °C) and those experienced the formation of a liquid phase (at 575 and 600 °C). As explained in the previous section the overall surface texture is relatively uniform for samples annealed at 550 °C, whereas two distinct regions with

different texture characteristics are observed at higher annealing temperatures (depending on whether the redox reaction between Al and SiO_2 occurred at the solid/solid or the liquid/solid interface). In order to elucidate the texture periodicity of samples annealed at different temperatures, 2D Fast Fourier Transform (2D FFT) images are created using representative AFM images of samples annealed at 550 and 600 °C, as shown in Figure 112. For both cases, the highest intensity is seen at the center of the map, which corresponds to scattering events associated with lowest spatial frequencies, thus transmission is almost entirely specular. The scattering events with higher frequencies (i.e., diffused scattering) are represented with a higher k-vector, thus are further away from the center [177]. It can easily be seen that as at higher k-vectors the brightness of the sample 550_300 is significantly greater to that of the sample 600_060, suggesting a higher haze value over a wide range of frequencies.
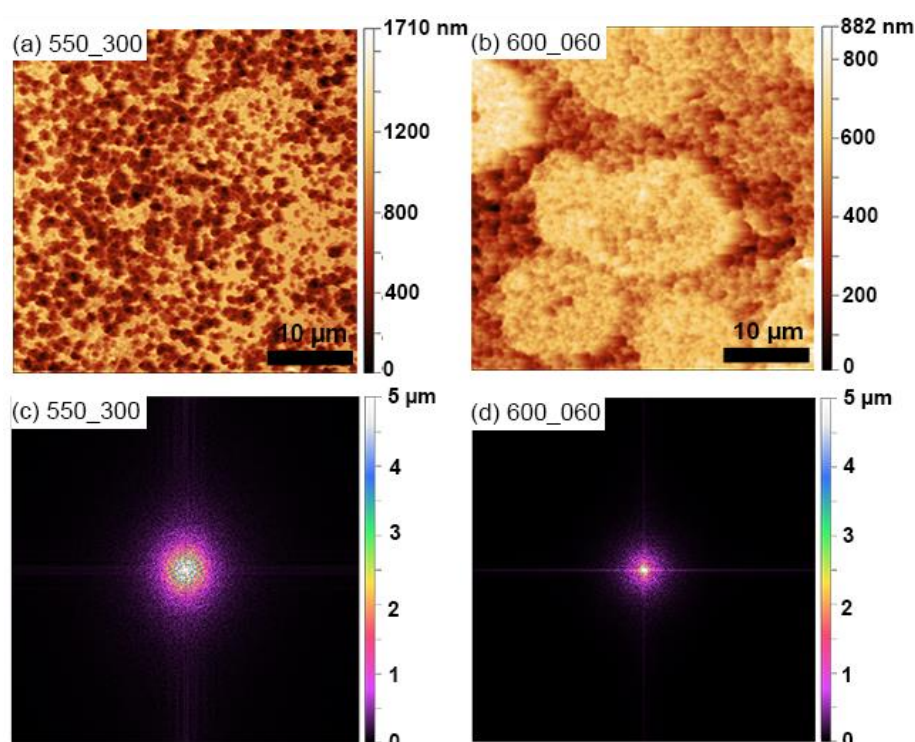
Figure 112. Comparison of surfaces by Fast Fourier Transform (FFT) of AFM images; (a) AFM image of 550_300, (b) AFM image of 600_060, (c) 2D FFT of AFM image of 550_300 and (d) 2D FFT of AFM image of 600_060.

4.5. The Effect of Glass Type

In this section, different glasses were used to investigate the influence of the glass type on AIT process. The study is conducted with conventional etchants for 150 nm Al coated samples that are annealed at 600 °C for 1 hour under N_2 flow. Soda-lime, borosilicate, alkaline-free and fused silica have processed. The characterization of these samples were made by SEM, AFM and integrated sphere spectrometer on standard configuration.

In Figure 113, SEM images of four different glasses are given. As seen from SEM images, soda-lime glass in Figure 113(a) have the largest crater size, followed by the alkaline-free glass given in Figure 113(c). On the other hand, borosilicate glass shown in Figure 113(b) have smaller crater sizes. Different picture exists in Figure 113(d) that shows the texture of the fused silica glass sample. The surface is not uniform as in the other samples and the crater formation is not observed. There might be a correlation between the resistance of the fused silica glass sample to etchants (as mentioned in the experimental section) and the observed non-uniformity. To understand the surface morphology better, AFM measurements is conducted as presented in Figure 114. In each AFM image, a 2-dimentional image of measurement is given at top right-hand corner of the 3-dimentional image with the color code and roughness in nm.
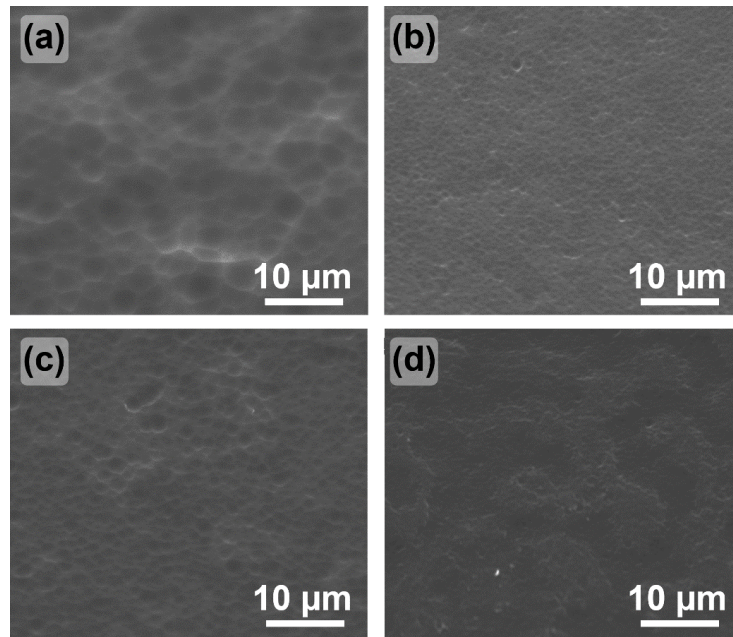
Figure 113. SEM image of (a) soda-lime glass, (b) borosilicate glass, (c) alkaline-free glass and (d) fused silica glass with 5000x magnification and 30° measurement angle
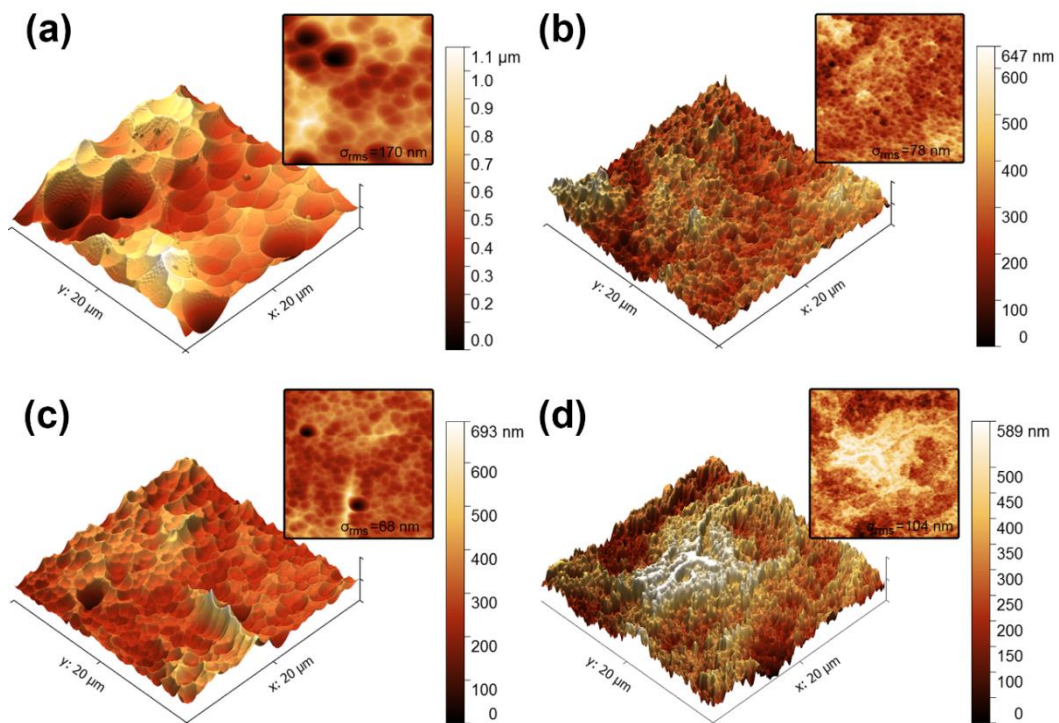
Figure 114. 20 µm x 20 µm AFM images of (a) soda-lime glass, (b) borosilicate glass, (c) alkaline-free glass and (d) fused silica glass

134

As seen in Figure 114(a), soda-lime glass have the largest craters with 170 nm roughness, confirming the SEM images. The surface is almost perfectly filled by U-shaped craters. On the other hand, in both SEM and AFM images for the alkaline-free glass [Figure 113(c) and Figure 114(c)], there are some very deep and large craters than the ones in the surrounding area, which results with 68 nm roughness. The reason might be the non-uniform composition difference or some contamination to glass before deposition. As seen in Figure 114(b), however, borosilicate glass has small craters but uniform surface with a roughness of 78 nm. Finally, in fused silica glass, surface is very random and there is no crater formation. The roughness of fused silica is 104 nm. When these four AFM images (Figure 114) considered together, it can be deducted that the presence of chemicals other than SiO_2 has a strong effect on texturing.

There is no observed relation between SiO_2 percentage and roughness but there are five other chemicals that might play a role in the texturing mechanism. The z-range of soda-lime glass is bigger than the rest and there is considerable difference between this glass and the others. The same scenario can be considered for roughness. When we look at the contents of the glass, it can be seen that CaO and MgO is present in soda-lime glass while absent in others. This might be the reason for the different morphologies. On the other hand, fused silica glass do not have any chemical compounds other than SiO_2 and as a result, z-range and crater size is small. This can be interpreted as, due to being pure SiO_2, chemical reaction starts simultaneously in most of the points on the surface that prevent formation of U-shaped craters. The forming of U-shaped craters may depend on existence of non-SiO_2 components like B_2O_3, Na_2O etc.

After AFM measurements, optical measurements are conducted, as presented in Figure 115. Optical transmittance and percentage of transmitted light which is scattered (haze) are measured.
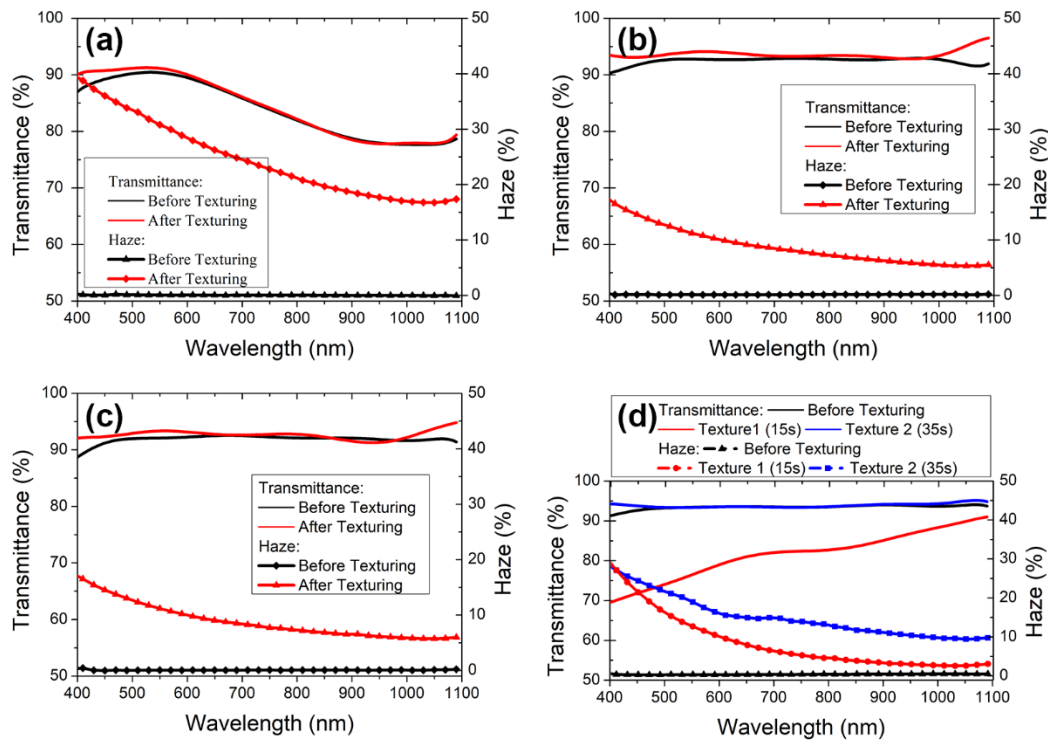
Figure 115. Total transmission and haze of (a) soda-lime glass, (b) borosilicate glass, (c) alkaline-free glass and (d) fused silica presented as before texturing and after texturing.

Among these four different glasses, soda-lime glass yielded the highest haze value subsequent to texturing, as seen in Figure 115(a). In addition, there is an enhancement in optical transmittance up to 600 nm wavelength, which can also be related to the high haze. If we focus on the interval 400-450 nm, it can be seen that there is an important increase in transmittance while haze is making a peak. The same relation between haze and increase in total transmittance can be observed in Figure 115(b) and Figure 115(c) where the optical characteristics of the borosilicate and alkaline-free glasses are given, respectively. However, the enhancement in total transmission can be observed up to 700 nm in this case. This relation may be determined by surface morphology which induce graded refractive index so that reflection from textured surface is decreased [67], [178].

It is seen in Figure 115(d), there is an enhancement in optical transmission up to 500 nm wavelength. This enhancement is probably due to the relatively small

surface structures formed upon texturing. However, the haze is larger than the ones of alkaline free glass and borosilicate glass.

The influence of the composition of the glass was investigated in this study. As a result, it was observed that different compositions lead to different surface structures. With optimized AIT process, soda-lime glass performs better than other type of glasses in terms of haze and uniformity of the surface.

4.6. Combination of Macro and Micro/Nano Texture

In this thesis, different parameters were optimized to obtain high haze values combined with high surface uniformity. This section covers the attempts to obtain more effective light trapping schemes by combination of textures obtained by AIT process with macro structures, sandy texture and inverted prism pattern. The characterization of these samples were made by FE-SEM and integrated sphere spectrometer on reverse configuration.

A float soda-lime glass is textured to obtain nano and micro textures as a control group. Results show that surface texturing of float glass was achieved successfully. FE-SEM images of AIT float glasses etched by acidic and basic solutions are given in Figure 116(a) and Figure 116(b), respectively. By applying different types of etching solutions in AIT process, variable crater size distribution was obtained. Acidic etchant provides micro scale crater formation on the surface (named as *float_acidic*), whereas basic etchant, which includes NaOH, provides smaller craters that are mainly in the range of 0.2-1.0 µm.
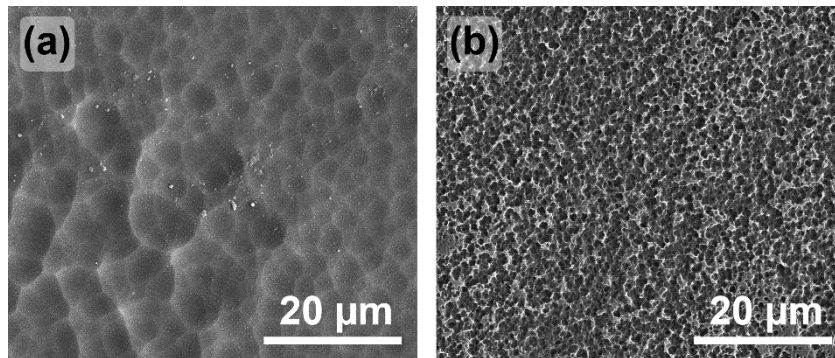
Figure 116. FE-SEM images of AIT float glasses etched by (a) acidic solution, (b) basic solution
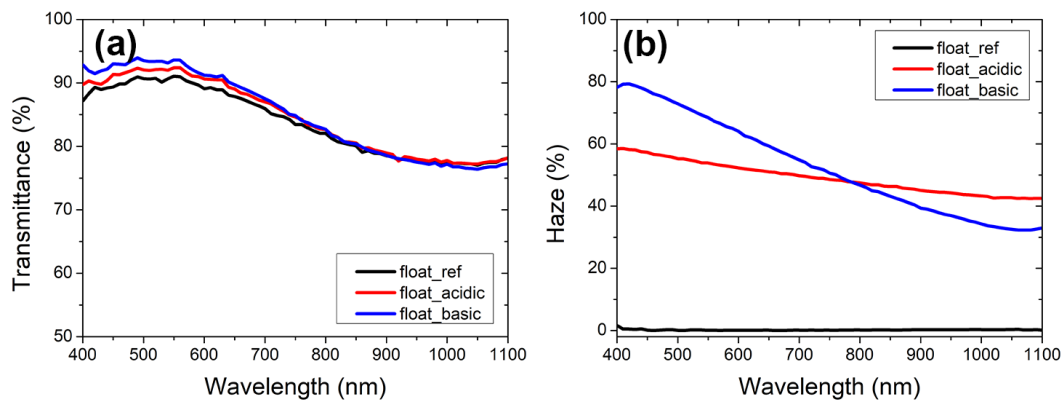
Figure 117. Optical measurement results of AIT float glasses. (a) transmittance and (b) haze

The effect of etching solution on the optical properties and crater size distribution of the glass can be seen clearly in Figure 117. Transmittance of the glass was slightly increased when surface was textured by AIT. The increase in transmittance is higher for *float_basic* samples when compared to *float_acidic*. Furthermore, in the case of haze at lower wavelengths (<700 nm), haze is higher for *float_basic*. Haze was observed to decrease from 75% (at 400 nm) to 33% (at 1100 nm). However, the haze value of *float_acidic* is 60% that lower than that of *float_basic*. In addition, the decrease in the haze with the increase of wavelength is lower than for the *float_basic*. Results of optical measurements can be correlated with crater size distribution and effects can be visualized with these graphs. In the case of

basic etchant, smaller craters efficiently scatter light for lower wavelengths which results in higher haze values. On the other hand, acidic etchant that provides bigger craters yields in more uniform haze through visible light spectrum.

Two types of macro textured glasses, prism and sandy were supplied by Şişecam. The surface profiles and SEM images of the non-processed samples are given previously in Figure 46 presented in the section, 4.6. Combination of Macro and Micro/Nano Texture. The range of the peak to peak height is 19 μm in sandy glass [Figure 46(b)] while it is 96 μm in prism glass [Figure 46(d)].

These samples were textured by AIT method with acidic and basic etching solutions. It is seen in Figure 118(a) and Figure 118(c), that the surface structure of both glass types showed a similar pattern. It presents similar features obtained in *float_acidic* samples. In addition, basic solution etched sandy glass (*sandy_basic*) appears analogous to *float_basic* in terms of surface features [Figure 118(b) and Figure 116(b)]. On the other hand, *prism_basic* has non-uniform crater distribution as seen in Figure 118(d). This non-uniformity is resulting from different etching rates on the sample due to the inverted pyramid-like geometry of prism glass.
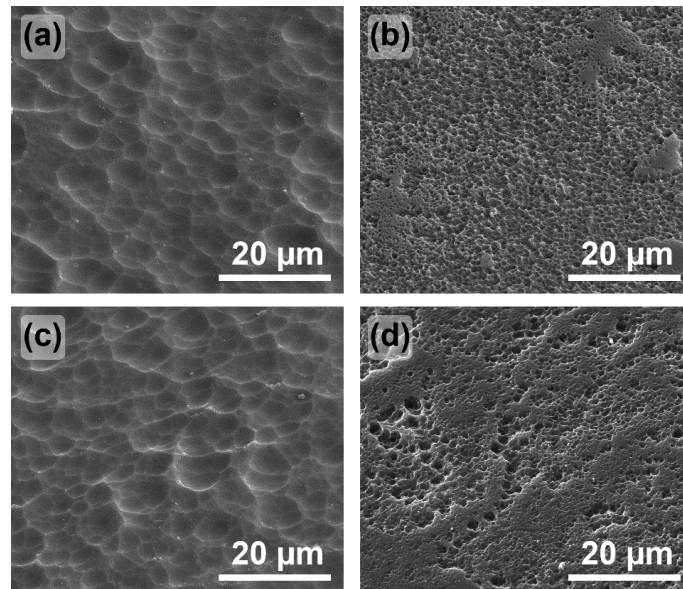
Figure 118. FE-SEM images of AIT Sandy glass etched by (a) acidic, (b) basic etchant and AIT Prism glass etched by (c) acidic, (d) basic etchant.

In order to clearly observe the crater formation by basic etchant, SEM image was magnified as seen in Figure 119. It is seen that smaller craters in the size of sub-microns were settled inside the inverted pyramid-like grooves.
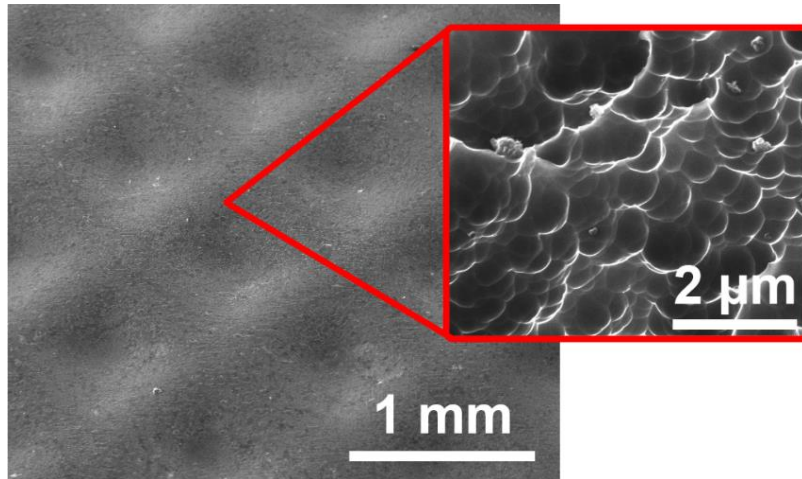
Figure 119. Magnified FE-SEM image of prism_basic

In Figure 120 and Figure 121, optical measurements of AIT sandy and prism glasses are depicted. It is obvious that AIT process has increased haze values remarkably. Moreover, transmittance values were slightly increased for all cases as seen in Figure 120(a) and Figure 121(a). In Figure 120(b), it is seen that initial haze of sandy glass (*sandy_ref*) is as low as 3%. After texturing of the glass by AIT technique, haze has reached slightly below 50% and lowering to 30% as the spectrum goes to infrared (IR) region for *sandy_acidic*. On the other hand, haze of *sandy_basic* has reached nearly 75% and reduced to 30% in IR region. The pattern in haze for *sandy_basic* is similar to *float_basic*, which means there is no significant effect of macro-textured surface structure of sandy sample on optical properties. However, in the *sandy_acidic*, haze is lower when compared to *float_acidic*. The combination of macro-nano texture in sandy patterned samples did not show a significant difference in terms of haze when compared to AIT float glass.
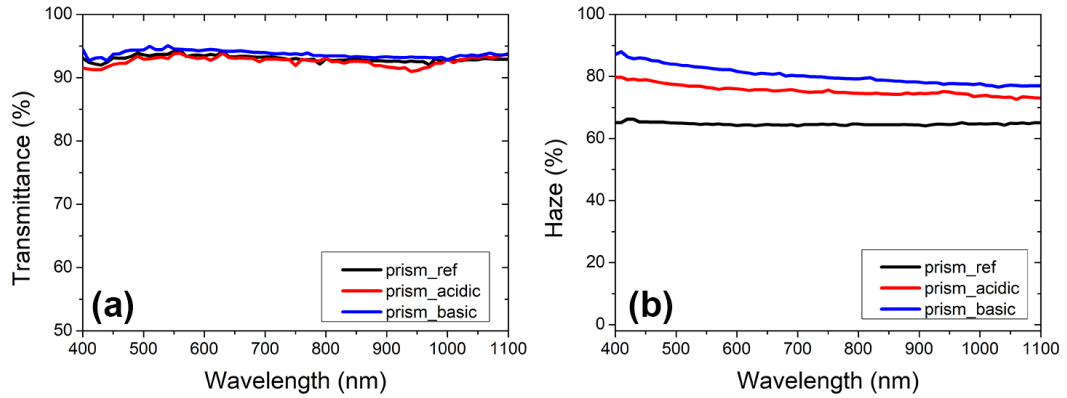
Figure 120. (a) Transmittance and (b) haze measurements of processed sandy glasses.
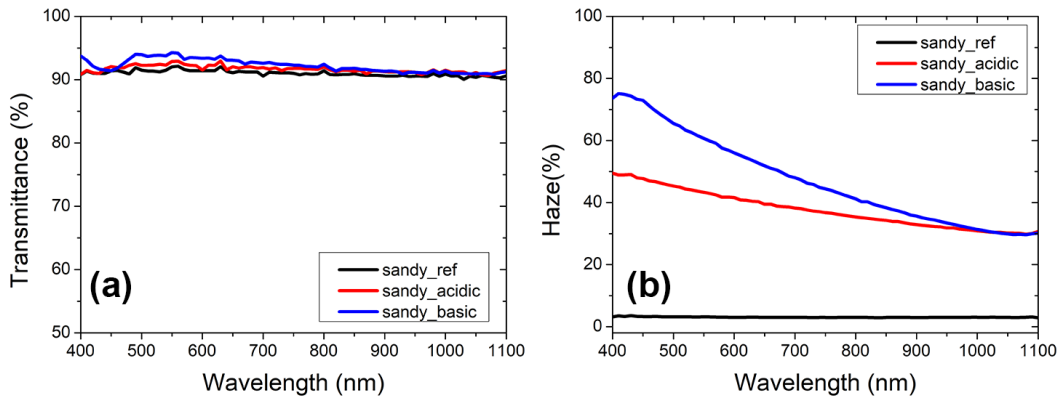
Figure 121. (a) Transmittance and (b) haze measurements of processed prism glasses.

It can be observerd from Figure 121(b) that even non-processed prism glass has a uniform haze value around 65%. Commercially available non-textured prism glasses are competitive with AIT sandy glasses. Moreover, it shows the same pattern as that of *float_acidic*. After AIT process, *prism_acidic* reached 80% and *prism_basic* gave nearly 90% haze values. In addition, haze follows a uniform pattern through solar spectrum. Thus, it can be concluded that AIT prism glass is superior in terms of haze.

With the combination of different textures, it is possible to obtain near-unity haze. In this study, inverted prism macro pattern combined with AIT employs basic solution gives higher performance than standard AIT employs basic or acidic solution

141

to remove reaction products. On the other hand, random sandy texture gives no significant enhancement in the optical properties when it compared with float glass.

4.5. Enhancement in a-Si:H Thin Films and Solar Cells

4.5.1. Thin a-Si:H Film Results

Absorption and spectral response results of 300 nm a-Si:H deposited samples are presented in Figure 122 with a comparison between coated float sample. In Figure 122(a), the wavelength range was set as 500-700 nm as it is in the vicinity of the cut-off wavelength. Between 550-650 nm, the area under the absorption curves for textured samples are greater than that for reference glass, which corresponds to an increase in the absorption by thin film deposited on textured glasses. Similar observation can be deducted from Figure 122(b) that shows normalized spectral response measurement results.
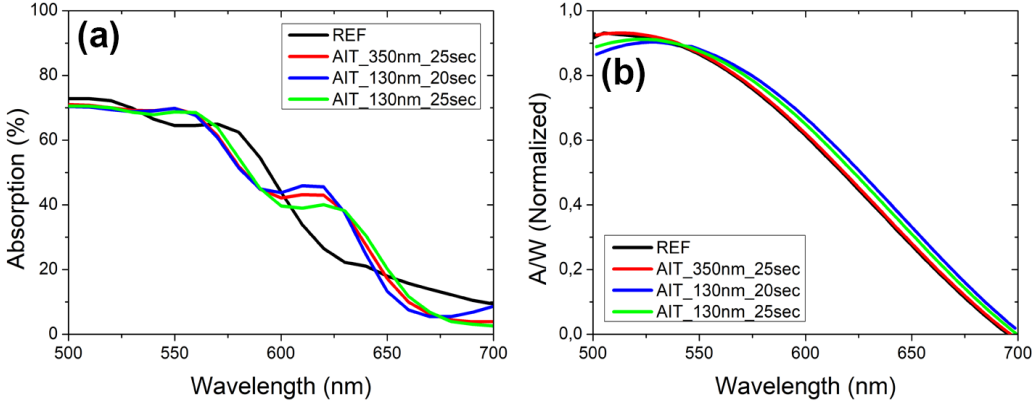
Figure 122. (a) Absorption and (b) normalized spectral response of reference glass, AIT_350nm_25sec, AIT_130nm_20sec and AIT_130nm_25sec coated with 300 nm a-Si:H.

The enhancement in spectral response of a-Si:H deposited samples can be found from Eq. 27. The enhancement in the photocurrent was observed for all samples (Figure 123). The maximum enhancement was obtained for 630 nm wavelength. AIT_130nm_20sec sample shows 5% enhancement in the photocurrent, which is maximum.

$$\%I_{ph\_Enhancement}(\lambda) = \left(I_{ph\_AIT} - I_{ph\_REF}\right)x100 \qquad \text{(Eq. 27)}$$
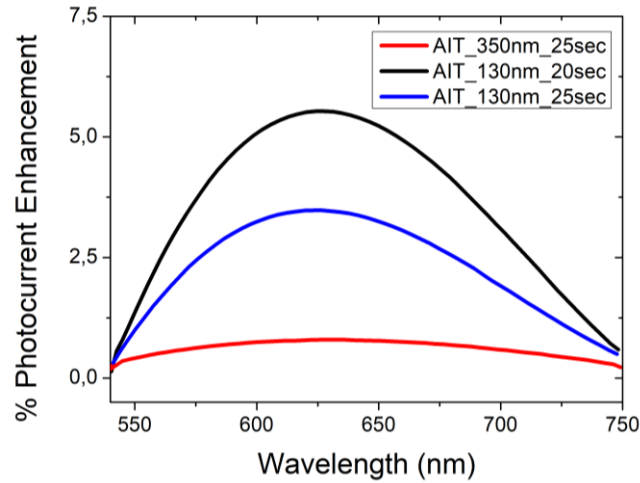
Figure 123. Spectral photocurrent enhancement of a-Si:H deposited samples

4.5.2. a-Si:H Solar Cell Results

In this study, AIT processed float, sandy and prism glasses were used. The results of I-V measurement are tabulated in Table 18. It is observed that non textured float glass has peeling off problem after a-Si:H solar cell production. That is the reason why it was not possible to make I-V measurements. However, a-Si:H solar cells on processed float samples were successfully produced. The efficiency for conventional AIT process (float_acidic) was 2.34%, while it was 2.15% for developed AIT process

(float_basic). The I-V curves of these samples are presented in Figure 124. The Jsc is significantly lower in float_basic sample.

Table 18. I-V measurement results of a-Si:H solar cells on float, sandy and prism glasses

Sample	Voc (V)	Jsc (mA/cm^2)	Fill Factor (%)	Efficiency (%)
Float_acidic	0.76	4.23	65.42	2.34
Float_basic	0.77	3.86	65.25	2.15
Sandy_ref	0.77	4.16	66.72	2.38
Sandy_acidic	0.76	4.48	66.30	2.51
Sandy_basic	0.75	4.99	65.86	2,74
Prism_ref	0.76	4.34	66.86	2.47
Prism_acidic	0.75	4.18	61.36	2.14
Prism_basic	0.75	4.94	61.79	2.55
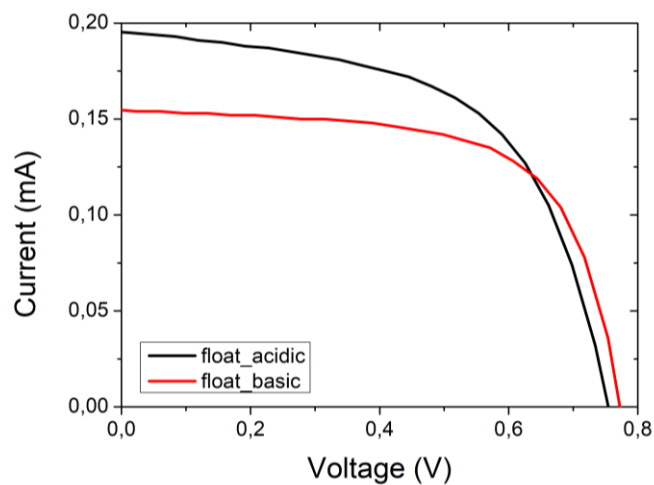
Figure 124. I-V measurement of float_acidic and float_basic glasses

For sandy and prism glasses, a-Si:H solar cell production has been successfully carried out. Results are tabulated in Table 18 and I-V curves are given in Figure 125. In sandy glasses [Figure 125(a)], reference glass has 2.38% efficiency. After AIT

process with conventional etchants, the efficiency was increased to 2.51% while J_{sc} was increased from 4.16 mA/cm^2 to 4.48 mA/cm^2. On the other hand, for developed solution, efficiency was increased further to 2.74%., while J_{sc} was increased to 4.99 mA/cm^2. For sandy glass, developed solution offers higher enhancement.

In processed prism glasses [Figure 125(b)], conventional AIT process was resulted with lower efficiency than reference prism glass (2.14% and 2.47% correspondingly). On the other hand, developed process offers an enhancement in terms of efficiency and short circuit current. The efficiency was increased to 2.55% while J_{sc} was risen from 4.34 mA/cm^2 to 4.94 mA/cm^2.
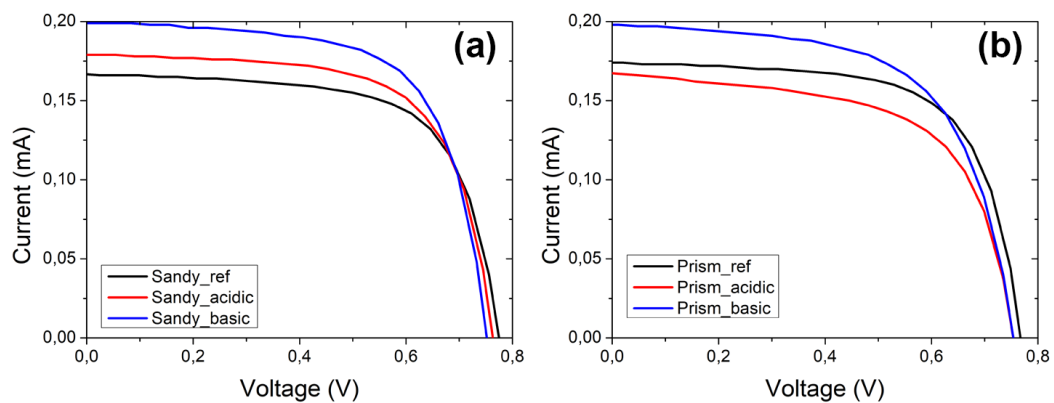
Figure 125. I-V measurement results of AIT process (a) sandy and (b) prism glasses with reference samples

It is observed that AIT process eliminated peeling-off problem of a-Si:H solar cells. Additionally, it was measured as AIT texturing method offers enhancement in the efficiency. For sandy glass, the enhancement in the efficiency was higher than the prism glass. The maximum efficiency value was obtained for sandy_basic as 2.74% while the lowest efficiency value was 2.14% for prism_acidic.

CHAPTER V

CONCLUSION

In this thesis, aluminum induced glass texturing, which is one of the light trapping schemes that can be applied to thin film solar cells, is optimized alongside with improvements in the process. Optimization studies of aluminum thickness and etching by conventional etchants were conducted. In each sample, U-shaped craters on the surface with different topographies were obtained. It was seen that 50% haze at 400 nm wavelength in the transmittance could be achieved with conventional AIT process. The crater size differs from 2 µm to 5 µm. On the other hand, AIT process, in which developed solution was used, offers 80% haze at 400 nm wavelength with craters sizes ranging from 0.2 µm to 1 µm.

During the optimization of the annealing, it was observed that above the eutectic temperature, reaction proceeds with phase transformations. After certain concentration of elemental Si, liquid Al-Si phase forms and the reaction rate increases dramatically during the annealing process. Moreover, due to agglomeration of c-Si and phase transformations, the surface is not uniform. On the other hand, below the eutectic temperature, the reaction proceeds in solid phase and elemental Si crystallize throughout aluminum induced crystallization mechanism. In both cases, c-Si forms with (111) orientation.

It is also observed that the surface texture strongly depends on the composition of the glass. Soda-lime glass offers highest haze values with high uniformity on the surface. On the other hand, no crater formation was observed on fused silica glass that formed by 100% SiO_2. An attempt to increase the haze value has been conducted with

the combination of macro texture with AIT textures. With the combination of AIT texture with macro textures, it is possible to obtain 90% haze with high unity throughout the solar spectrum.

When AIT samples were coated with a-Si:H thin film, 5% enhancement in photocurrent near the cut-off wavelength was achieved. A peeling-off problem in float glasses was present. In AIT glasses, there were no observable peeling-off after a-Si:H solar cell production. Even though prism glass offers 90% haze, the efficiency measurements showed an increase from 2.47% to 2.55%. However, the efficiency of a-Si:H solar cell in sandy glass that was textured by developed process was 2.74% while it was 2.38% for reference sandy glass. The enhancement in thin film solar cells with the aluminum induced texturing method on glass substrates was proved to be possible by thin film and solar cell measurements.

REFERENCES

[1]   O. Schafer and M. Schmela, "Global PV Market Outlook 2016-2020," 2016.

[2]   C. Ryan, "Mercom forecasts 76GW in global PV installations in 2016," *PVTech*, 2016.

[3]   T. Desrues *et al.*, "Evaluating the contact properties of transparent conductive oxides on crystalline silicon homojunction solar cells," pp. 1976–1979, 2016.

[4]   "Photovoltaics Report," 2016.

[5]   H. Sai, T. Matsui, and K. Matsubara, "Stabilized 14.0%-efficient triple-junction thin-film silicon solar cell," *Appl. Phys. Lett.*, vol. 109, no. 18, pp. 1–6, 2016.

[6]   R. Schmalensee and V. Bulovic, "The Future of Solar Energy," 2015.

[7]   P. Rappaport, "The photovoltaic effect and its utilization," *Sol. Energy*, vol. 3, no. 4, pp. 8–18, 1959.

[8]   A. Einstein, "Concerning an Heuristic Point of View Toward the Emission and Transformation of Light," *Ann. Phys.*, vol. 17, pp. 132–148, 1905.

[9]   R. Uecker and A. Pajaczkowska, "Jan Czochralski and historical development of the Czochralski method - part2," in *17th International Conference on Crystal Growth and Epitaxy*, 2013.

[10]   M. A. Green, "Photovoltaic principles," *Phys. E Low-Dimensional Syst. Nanostructures*, vol. 14, no. 1–2, pp. 11–17, 2002.

[11]   M. A. Green, "Silicon photovoltaic modules: A brief history of the first 50 years," *Prog. Photovoltaics Res. Appl.*, vol. 13, no. 5, pp. 447–455, 2005.

[12]   M. A. Green, "High Efficiency Silicon Solar Cells," in *Seventh E.C. Photovoltaic Solar Energy Conference: Proceedings of the International Conference, held at Sevilla, Spain, 27--31 October 1986*, A. Goetzberger, W. Palz, and G. Willeke, Eds. Dordrecht: Springer Netherlands, 1987, pp. 681–687.

[13]   I. Tsagas, "Turkey adds 571 MW of solar PV in 2016," *pv magazine*, 2017.

[14]   "Türkiye'de Lisanssız Güneş Enerjisinin Gelişimi," *Energy Institute*. [Online]. Available: http://enerjienstitusu.com/turkiye-kurulu-elektrik-enerji-gucu-mw/. [Accessed: 03-Apr-2017].

[15]   J. L. Sawin, K. Seyboth, and F. Sverrisson, *Renewables 2016: Global Status Report*. 2016.

[16] "Sunlight," *Wikipedia*, 2017. [Online]. Available: https://en.wikipedia.org/wiki/Sunlight. [Accessed: 04-Apr-2017].

[17] C. Riordan and R. Hulstron, "What is an air mass 1.5 spectrum?," *IEEE Conf. Photovolt. Spec.*, pp. 1085–1088, 1990.

[18] Florida Solar Energy Center, "Test Method for Photovoltaic Module Power Rating FSEC Standard 202-10," no. January, 2010.

[19] N. Mahato, M. O. Ansari, and M. H. Cho, "Production of Utilizable Energy from Renewable Resources: Mechanism, Machinery and Effect on Environment," *Adv. Mater. Res.*, vol. 1116, pp. 1–32, 2015.

[20] W. Shockley, "The Theory of p-n Junctions in Semiconductors and p-n Junction Transistors," *Bell Syst. Tech. J.*, vol. 48, no. 3, pp. 435–489, 1949.

[21] "p-n junction," *Wikiwand*. [Online]. Available: http://www.wikiwand.com/en/P–n_junction. [Accessed: 06-Apr-2017].

[22] D. R. Hodges, "Development of CdTe Thin Film Solar Cells on Flexible Foil Substrates," University of South Florida, 2008.

[23] F. Meillaud, A. Shah, C. Droz, E. Vallat-Sauvain, and C. Miazza, "Efficiency limits for single-junction and tandem solar cells," *Sol. Energy Mater. Sol. Cells*, vol. 90, no. 18–19, pp. 2952–2959, 2006.

[24] "Fitting The I-V Curve," *PhysX202*, 2016. [Online]. Available: https://sharepoint.uvm.edu/sites/physx202/Wiki Pages/I-V curves and how to make the fitting work.aspx. [Accessed: 06-Apr-2017].

[25] O. Isabella, *Light management in thin-film silicon solar cells*. 2013.

[26] E. H. Çiftpınar, "Selective Emitter Formation via Single Step Doping Through Laser Patterned Mask Oxide Layer for Monocrystalline Silicon Solar Cells," Middle East Technical University, 2014.

[27] K. Bouzidi, M. Chegaar, and A. Bouhemadou, "Solar cells parameters evaluation considering the series and shunt resistance," *Sol. Energy Mater. Sol. Cells*, vol. 91, no. 18, pp. 1647–1651, 2007.

[28] M. A. Green, *Solar Cells: Operating Principles, Technology, and System Applications*. Englewood Cliffs: Prentice-Hall, 1982.

[29] M. Fischer, "The 7 th edition of the International Technology Roadmap for Photovoltaics (ITRPV) - Current trends and future challenges in c- Si PV," 2016.

[30] T. Sinno, E. Dornberger, W. von Ammon, R. . Brown, and F. Dupret, "Defect engineering of Czochralski single-crystal silicon," *Mater. Sci. Eng. R Reports*, vol. 28, no. 5, pp. 149–198, 2000.

[31] T. F. Li, K. M. Yeh, W. C. Hsu, and C. W. Lan, "High-quality multi-crystalline silicon (mc-Si) grown by directional solidification using notched crucibles," *J. Cryst. Growth*, vol. 318, no. 1, pp. 219–223, 2011.

[32] W. Kaiser and P. H. Keck, "Oxygen content of silicon single crystals," *J. Appl. Phys.*, vol. 28, no. 8, pp. 882–887, 1957.

[33] "Commercial Solar Cells," *Silicon Solar*, 2015. [Online]. Available: http://www.siliconsolar.com/commercial-solar-cells.html. [Accessed: 07-Apr-2017].

[34] S. Narasimha, a. Rohatgi, and a. W. Weeber, "An optimized rapid aluminum back surface field technique for\nsilicon solar cells," *IEEE Trans. Electron Devices*, vol. 46, no. 7, pp. 1363–1370, 1999.

[35] S. Gatz *et al.*, "19.4%-efficient large-area fully screen-printed silicon solar cells," *Phys. status solidi - Rapid Res. Lett.*, vol. 5, no. 4, pp. 147–149, Apr. 2011.

[36] "NREL Best Research-Cell Efficiencies," *National Renewable Energy Laboratory*, 2017. [Online]. Available: https://www.nrel.gov/pv/assets/images/efficiency-chart.png. [Accessed: 02-Apr-2017].

[37] M. D. Lammert and R. J. Schwartz, "The interdigitated back contact solar cell: a silicon solar cell for use in concentrated sunlight," *IEEE Trans. Electron Devices*, vol. ED-24, no. 4, pp. 337–342, 1977.

[38] J. M. Gee, W. K. Schubert, and P. A. Basore, "Emitter wrap-through solar cell," pp. 265–270, 1993.

[39] F. Clement *et al.*, "High throughput via-metallization technique for multi-crystalline metal wrap through (MWT) silicon solar cells exceeding 16% efficiency," *Sol. Energy Mater. Sol. Cells*, vol. 94, no. 1, pp. 51–56, 2010.

[40] "Solarflex Solar Panel 5W," *Alternargy*, 2017. [Online]. Available: https://www.alternagy.co.za/shop/solarflex-solar-panel-5w/. [Accessed: 10-Apr-2017].

[41] J. Poortmans and V. Arkhipow, Eds., *Thin Film Solar Cells: Fabrication, Characterization and Applications*. West Sussex: John Wiley & Sons, 2006.

[42] D. E. Carlson and C. R. Wronski, "Amorphous silicon solar cell," *Appl. Phys. Lett.*, vol. 28, no. 11, pp. 671–673, 1976.

[43] Roland Scheer and H.-W. Schock, "Chapter 1: Introductiın," in *Chalcogenide Photovoltaics: Physics, Technologies, and Thin Film Devices*, Weinheim: WILEY-VCH Verlag, 2011, pp. 1–8.

[44] J. Britt and C. Ferekides, "Thin-film CdS/CdTe solar cell with 15.8% efficiency," *Appl. Phys. Lett.*, vol. 62, no. 22, pp. 2851–2852, 1993.

[45] K. P. Bhandari, J. M. Collier, R. J. Ellingson, and D. S. Apul, "Energy payback time (EPBT) and energy return on energy invested (EROI) of solar photovoltaic systems: A systematic review and meta-analysis," *Renew. Sustain. Energy Rev.*, vol. 47, pp. 133–141, 2015.

[46]   M. Gloeckler and J. R. Sites, "Band-gap grading in Cu(In,Ga)Se2 solar cells," *J. Phys. Chem. Solids*, vol. 66, no. 11, pp. 1891–1894, 2005.

[47]   H. TRIBUTSCH, "Reaction of Excited Chlorophyll Molecules At Electrodes and in Photosynthesis," *Photochem. Photobiol.*, vol. 16, no. 4, pp. 261–269, 1972.

[48]   B. O'Regan and M. Grätzel, "A low-cost, high-efficiency solar cell based on dye-sensitized colloidal TiO2 films," *Lett. to Nat.*, vol. 353, no. 6346, pp. 737–740, 1991.

[49]   K. E. Jasim, "Dye sensitised solar cells-working principles, challenges and opportunities," in *Solar Cells – Dye-Sensitized Devices*, 2007, pp. 171–204.

[50]   M. R. Jones, "Dye-sensitized solar cell," 2009. [Online]. Available: https://en.wikipedia.org/wiki/Dye-sensitized_solar_cell#/media/File:Dye_Sensitized_Solar_Cell_Scheme.png. [Accessed: 11-Apr-2017].

[51]   H. Spanggaard and F. C. Krebs, "A brief history of the development of organic and polymeric photovoltaics," *Sol. Energy Mater. Sol. Cells*, vol. 83, no. 2–3, pp. 125–146, 2004.

[52]   M. M. Lee, J. Teuscher, T. Miyasaka, T. N. Murakami, and H. J. Snaith, "Efficient Hybrid Solar Cells Based on Meso-Superstructured Organometal Halide Perovskites," *Science (80-.).*, vol. 338, pp. 643–647, 2012.

[53]   M. A. Green and M. J. Keevers, "Optical properties of intrinsic silicon at 300 K," *Prog. Photovoltaics Res. Appl.*, vol. 3, no. 3, pp. 189–192, 1995.

[54]   "Absorption Coefficient," *PVEducation.org*. [Online]. Available: http://www.pveducation.org/pvcdrom/absorption-coefficient. [Accessed: 17-Apr-2017].

[55]   E. Yablonovitch and G. D. Cody, "Intensity Enhancement in Textured Optical Sheets for Solar-Cells," *IEEE Trans. Electron Devices*, vol. 29, no. 2, pp. 300–305, 1982.

[56]   M. Lipiñski, P. Ziêba, S. Jonas, S. Kluska, and M. S. Owski, "Optimisation of SiNx:H layer for multicrystalline silicon solar cells," *Opto-electronics Rev.*, vol. 12, no. 1, pp. 41–44, 2004.

[57]   "Anti-Reflection Coatings," *PVEducation.org*. [Online]. Available: http://www.pveducation.org/pvcdrom/anti-reflection-coatings. [Accessed: 30-Apr-2017].

[58]   H. K. Raut, V. A. Ganesh, A. S. Nair, and S. Ramakrishna, "Anti-reflective coatings: A critical, in-depth review," *Energy Environ. Sci.*, vol. 4, no. 10, p. 3779, 2011.

[59]   J. A. Dobrowolski, D. Poitras, P. Ma, H. Vakil, and M. Acree, "Toward perfect antireflection coatings: numerical investigation.," *Appl. Opt.*, vol. 41, no. 16, pp. 3075–3083, 2002.

[60] D. N. Wright, E. S. Marstein, and a. Holt, "Double layer anti-reflective coatings for silicon solar cells," *Conf. Rec. Thirty-first IEEE Photovolt. Spec. Conf. 2005.*, no. 2027, pp. 1237–1240, 2005.

[61] J. Xiong, S. N. Das, J. P. Kar, J.-H. Choi, and J.-M. Myoung, "A multifunctional nanoporous layer created on glass through a simple alkali corrosion process," *J. Mater. Chem.*, vol. 20, no. 45, p. 10246, 2010.

[62] S. Das, A. Kundu, C. Banerjee, P. Dey, S. K. Datta, and H. Saha, "Front Surface Glass Texturization for Improved Performance of Amorphous Silicon Solar Cell," *Phys. Semicond. Devices*, vol. 16, no. 1, pp. 375–378, 2014.

[63] "Low Cost Industrial Manufacturing of a Single Layer Antireflective Surface on Glass Sheets," Ronnede.

[64] T. Schuler and M. . Aegerter, "Optical, electrical and structural properties of sol gel ZnO:Al coatings," *Thin Solid Films*, vol. 351, no. 1, pp. 125–131, 1999.

[65] W. Primak, "Refractive index of silicon.," *Appl. Opt.*, vol. 10, no. 4, pp. 759–63, 1971.

[66] A. M. K. Dagamseh, B. Vet, F. D. Tichelaar, P. Sutta, and M. Zeman, "ZnO:Al films prepared by rf magnetron sputtering applied as back reflectors in thin-film silicon solar cells," *Thin Solid Films*, vol. 516, no. 21, pp. 7844–7850, 2008.

[67] J. Müller, B. Rech, J. Springer, and M. Vanecek, "TCO and light trapping in silicon thin film solar cells," *Sol. Energy*, vol. 77, no. 6, pp. 917–930, Dec. 2004.

[68] O. Berger, D. Inns, and A. G. Aberle, "Commercial white paint as back surface reflector for thin-film solar cells," *Sol. Energy Mater. Sol. Cells*, vol. 91, no. 13, pp. 1215–1221, 2007.

[69] S. A. Maier, *Plasmonics: Fundamentals and Applications*. Springer Science & Business Media, 2007.

[70] A. Trügler, *Optical Properties of Metallic Nanoparticles: Basic Principles and Simulation*. Springer, 2016, 2016.

[71] K. A. Willets and R. P. Van Duyne, "Localized surface plasmon resonance spectroscopy and sensing.," *Annu. Rev. Phys. Chem.*, vol. 58, pp. 267–97, 2007.

[72] H. Nasser, Z. M. Saleh, E. Özkol, A. Bek, and R. Turan, "Advanced light trapping interface for a-Si:H thin film," *Phys. Status Solidi*, vol. 12, no. 9–11, pp. 1206–1210, 2015.

[73] H. Tan, R. Santbergen, A. H. Smets, and M. Zeman, "Plasmonic light trapping in thin-film silicon solar cells with improved self-assembled silver nanoparticles," *Nano Lett.*, vol. 12, no. 8, pp. 4070–4076, 2012.

[74] R. S. Quimby, *Photonics and Lasers: An Introduction*. New Jersey: John Wiley & Sons, Inc., 2006.

[75] S. Venkataraj, J. Wang, P. Vayalakkara, and A. G. Aberle, "Light scattering enhancement by double scattering technique for multijunction thin-film silicon

solar cells," *IEEE J. Photovoltaics*, vol. 3, no. 2, pp. 605–612, 2013.

[76] A. Mavrokefalos, S. E. Han, S. Yerci, M. S. Branham, and G. Chen, "Efficient Light Trapping in Inverted Nanopyramid Thin Crystalline Silicon Membranes for Solar Cell Applications," *Nano Lett.*, vol. 12, no. 6, pp. 2792–6, 2012.

[77] L. Tsakalakos, J. Balch, J. Fronheiser, B. A. Korevaar, O. Sulima, and J. Rand, "Silicon nanowire solar cells," *Appl. Phys. Lett.*, vol. 91, no. 23, pp. 3–6, 2007.

[78] C. Chartier, S. Bastide, and C. Lévy-Clément, "Metal-assisted chemical etching of silicon in HF–H2O2," *Electrochim. Acta*, vol. 53, no. 17, pp. 5509–5516, 2008.

[79] C. Xie *et al.*, "High-efficiency, Air Stable Graphene/Si Micro-hole Array Schottky Junction Solar Cells," *J. Mater. Chem. A*, no. 207890, p. , 2013.

[80] D. H. Macdonald *et al.*, "Texturing industrial multicrystalline silicon solar cells," *Sol. Energy*, vol. 76, no. 1, pp. 277–283, 2004.

[81] H. Park, S. Kwon, J. S. Lee, H. J. Lim, S. Yoon, and D. Kim, "Improvement on surface texturing of single crystalline silicon for solar cells by saw-damage etching using an acidic solution," *Sol. Energy Mater. Sol. Cells*, vol. 93, no. 10, pp. 1773–1778, 2009.

[82] Z. Xu, H.-Y. Wu, S. U. Ali, J. Jiang, B. T. Cunningham, and G. L. Liu, "Nanoreplicated positive and inverted submicrometer polymer pyramid array for surface-enhanced Raman spectroscopy," *J. Nanophotonics*, vol. 5, no. 1, p. 53526, 2011.

[83] K. Peng, Y. Xu, Y. Wu, Y. Yan, S. T. Lee, and J. Zhu, "Aligned single-crystalline Si nanowire arrays for photovoltaic applications," *Small*, vol. 1, no. 11, pp. 1062–1067, 2005.

[84] S. H. Altinoluk *et al.*, "Light Trapping by Micro and Nano-hole Texturing of Single-crystalline Silicon Solar Cells," *Energy Procedia*, vol. 92, pp. 291–296, Aug. 2016.

[85] H. Sai *et al.*, "Triple-junction thin-film silicon solar cell fabricated on periodically textured substrate with a stabilized efficiency of 13.6%," *Appl. Phys. Lett.*, vol. 106, no. 21, pp. 30–34, 2015.

[86] M. Berginski *et al.*, "The effect of front ZnO:Al surface texture and optical transparency on efficient light trapping in silicon thin-film solar cells," *J. Appl. Phys.*, vol. 101, no. 7, p. 74903, 2007.

[87] O. Kluth *et al.*, "Texture etched ZnO:Al coated glass substrates for silicon based thin film solar cells," *Thin Solid Films*, vol. 351, no. 1, pp. 247–253, 1999.

[88] J. A. Anna Selvan, A. E. Delahoy, S. Guo, and Y. M. Li, "A new light trapping TCO for nc-Si:H solar cells," *Sol. Energy Mater. Sol. Cells*, vol. 90, no. 18–19, pp. 3371–3376, 2006.

[89] N. A. S. Ahraei *et al.*, "Thin-film a-Si : H solar cells processed on aluminum-

induced texture (AIT) glass superstrates : prediction of light absorption enhancement," *Appl. Opt.*, vol. 54, no. 14, pp. 4366–4373, 2015.

[90]   P. Vayalakkara *et al.*, "Aluminum induced glass texturing process on borosilicate and soda-lime glass superstrates for thin-film solar cells," *Conf. Rec. IEEE Photovolt. Spec. Conf.*, pp. 003080–003083, 2011.

[91]   J. Wang, S. Venkataraj, C. Battaglia, P. Vayalakkara, and A. G. Aberle, "Analysis of optical and morphological properties of aluminium induced texture glass superstrates," *Jpn. J. Appl. Phys.*, vol. 51, no. 10 PART 2, pp. 8–11, 2012.

[92]   M. Lluscà, F. Urbain, V. Smirnov, A. Antony, J. Andreu, and J. Bertomeu, "Aluminium induced texturing of glass substrates with improved light management for thin film solar cells," *Sol. Energy Mater. Sol. Cells*, vol. 147, pp. 276–280, 2016.

[93]   N. Chuansuwanich, P. Campbell, P. I. Widenborg, a. Straub, and a. G. Aberle, "Light trapping properties of evaporated poly-silicon films on AIT-textured glass substrates," *Conf. Rec. Thirty-first IEEE Photovolt. Spec. Conf. 2005.*, pp. 1161–1164, 2005.

[94]   H. Cui, P. R. Campbell, and M. a. Green, "Compatibility of glass textures with E-beam evaporated polycrystalline silicon thin-film solar cells," *Appl. Phys. A Mater. Sci. Process.*, vol. 111, no. 3, pp. 935–942, 2013.

[95]   G. Yang *et al.*, "Modulated surface textured glass as substrate for high efficiency microcrystalline silicon solar cells," *Sol. Energy Mater. Sol. Cells*, vol. 133, no. 14, pp. 156–162, 2015.

[96]   W. Zhang *et al.*, "Alternative Substrate for Thin Film Solar Cells - Textured Glass," *Phys. Status Solidi*, vol. 7, no. 1120–1123, pp. 1120–1123, 2009.

[97]   H. Taniguchi *et al.*, "Amorphous silicon solar cell on textured tempered glass substrate prepared by sandblast process," *Sol. Energy Mater. Sol. Cells*, vol. 49, no. 1–4, pp. 101–106, Dec. 1997.

[98]   W. Zhang *et al.*, "Rough glass by 3d texture transfer for silicon thin film solar cells," *Phys. Status Solidi Curr. Top. Solid State Phys.*, vol. 7, no. 3–4, pp. 1120–1123, 2010.

[99]   T. Ichiki, Y. Sugiyama, T. Ujiie, and Y. Horiike, "Deep dry etching of borosilicate glass using fluorine-based high-density plasmas for microelectromechanical system fabrication," *J. Vac. Sci. Technol. B Microelectron. Nanom. Struct.*, vol. 21, no. 2003, p. 2188, 2003.

[100]   J. H. Park, N.-E. Lee, J. Lee, J. S. Park, and H. D. Park, "Deep dry etching of borosilicate glass using SF6 and SF6/Ar inductively coupled plasmas," *Microelectron. Eng.*, vol. 82, no. 2, pp. 119–128, Oct. 2005.

[101]   H. Park *et al.*, "Fabrication of honeycomb textured glass substrate and nanotexturing of zinc oxide front electrode for its application in high efficiency thin film amorphous silicon solar cell," *J. Photonics Energy*, vol. 7, no. 2, p.

25502, 2017.

[102] U. Blieske, T. Doege, P. Gayou, M. Neander, D. Neumann, and A. Prat, "LIght-trapping in Solar Modules using Extra-White Textured Glass," *3rd World Conf. Photovolt. Energy Conversion, 2003*, pp. 188–191, 2003.

[103] U. W. Paetzold *et al.*, "Thin-film silicon solar cell development on imprint-textured glass substrates," *Mater. Sci. Eng. B*, vol. 178, no. 9, pp. 617–622, 2013.

[104] J. Escarré *et al.*, "Geometric light trapping for high efficiency thin film silicon solar cells," *Sol. Energy Mater. Sol. Cells*, vol. 98, pp. 185–190, 2012.

[105] A. G. Aberle, P. I. P. I. Widenborg, N. Chuansuwanich, and N. Chuangsuwanich, "Glass Texturing," WO 2004/089841 A1, 2004.

[106] Y. Yin *et al.*, "Light Scattering and Current Enhancement for Microcrystalline Silicon Thin-Film Solar Cells on Aluminium-Induced Texture Glass Superstrates with Double Texture," vol. 2015, 2015.

[107] N. Sahraei, S. Venkataraj, A. G. Aberle, and M. Peters, "Optimum feature size of randomly textured glass substrates for maximum scattering inside thin-film silicon solar cells," *SPIE Photonics West 2014-OPTO Optoelectron. Devices Mater.*, vol. 8981, p. 89811D, 2014.

[108] Y. Huang, F. Law, P. I. Widenborg, and A. G. Aberle, "Crystalline silicon growth in the aluminium-induced glass texturing process," *J. Cryst. Growth*, vol. 361, no. 1, pp. 121–128, 2012.

[109] G. Jin, P. I. Widenborg, P. Campbell, and S. Varlamov, "Lambertian matched absorption enhancement in PECVD poly-Si thin film on aluminum induced textured glass superstrates for solar cell applications," *Prog. Photovoltaics Res. Appl.*, vol. 18, no. 8, pp. 582–589, 2010.

[110] H. Cui, G. P.J., P. R. Campbell, and M. A. Green, "Developments in the aluminum induced texturing (AIT) glass process," *Glas. Technol. - Eur. J. Glas. Sci. Technol. Part A*, vol. 53, no. 4, pp. 158–165, 2012.

[111] M. Lluscà *et al.*, "Textured Glass Substrates for Thin Film Silicon Solar Cells," in *28th European Photovoltaic Solar Energy Conference and Exhibition*, 2012, pp. 2170–2174.

[112] P. I. Widenborg and A. G. Aberle, "Polycrystalline silicon thin-film solar cells on AIT-textured glass superstrates," *Adv. Optoelectron.*, vol. 2007, 2007.

[113] O. Isabella, J. Krc, and M. Zeman, "Modulated surface textures for enhanced light trapping in thin-film silicon solar cells," *Appl. Phys. Lett.*, vol. 97, no. 10, 2010.

[114] P. I. Widenborg, S. V. Chan, T. Walsh, and a. G. Aberle, "Thin-film poly-SI solar cells on AIT-textured glass - Importance of the rear reflector," *Conf. Rec. IEEE Photovolt. Spec. Conf.*, no. i, pp. 7–9, 2008.

[115] N. Sahraei, S. Venkataraj, P. Vayalakkara, and A. G. Aberle, "Optical absorption enhancement in amorphous silicon films and solar cell precursors using the aluminum-induced glass texturing method," *Int. J. Photoenergy*, vol. 2014, 2014.

[116] S. J. Hwang, J. H. Lee, C. O. Jeong, and Y. C. Joo, "Effect of film thickness and annealing temperature on hillock distributions in pure Al films," *Scr. Mater.*, vol. 56, no. 1, pp. 17–20, 2007.

[117] K. Prabriputaloong and M. R. Piggott, "The Reaction Between Silica and Aluminum," *J. Electrochem. Soc. Solid-State Sci. Technol.*, vol. 603, no. 3, pp. 430–434, 1974.

[118] F. Dadabhai, F. Gaspari, S. Zukotynski, and C. Bland, "Reduction of silicon dioxide by aluminum in metal–oxide–semiconductor structures," *J. Appl. Phys.*, vol. 80, no. 11, pp. 6505–6509, 1996.

[119] H. Cui and P. R. Campbell, "A glass thinning and texturing method for light incoupling in thin-film polycrystalline silicon solar cells application," *Phys. status solidi - Rapid Res. Lett.*, vol. 6, no. 8, pp. 334–336, 2012.

[120] TRAKYA Cam Sanayii A.Ş., "FLOAT GLASS (CLEAR, 4 mm.) DATA SHEET," İstanbul, 2014.

[121] SCHOTT Technical Glass Solutions GmbH, "Schoott Borofloat 33," Jena.

[122] Schott, "Technical Glasses," 2014.

[123] "Fused Silica Wafers," *University Wafer*. [Online]. Available: http://www.universitywafer.com/Wafers_Services/Fused_Silica/fused_silica.h tml. [Accessed: 12-Sep-2015].

[124] "Spectral Response," *PVEducation.org*. [Online]. Available: http://www.pveducation.org/pvcdrom/solar-cell-operation/spectral-response.

[125] E. Iwamura, T. Ohnishi, and K. Yashikawa, "A study of hillock formation on Al-Ta alloy films for interconnections of TFT-LCDs," *Thin Solid Films*, vol. 270, pp. 450–455, 1995.

[126] B. Vermang *et al.*, "A study of blister formation in ALD Al2O3 grown on silicon," in *Photovoltaic Specialists Conference (PVSC), 2012 38th IEEE*, 2012, p. 13045908.

[127] F. C. Nix and D. MacNair, "The thermal expansion of pure metals: Copper, gold, aluminum, nickel, and iron," *Phys. Rev.*, vol. 60, no. 8, pp. 597–605, 1941.

[128] W. Mi-Tang and C. Jin-Shu, "Viscosity and thermal expansion of rare earth containing soda-lime-silicate glass," *J. Alloys Compd.*, vol. 504, no. 1, pp. 273–276, 2010.

[129] F. Lofaj, R. Satet, M. J. Hoffmann, and A. R. de Arellano López, "Thermal expansion and glass transition temperature of the rare-earth doped oxynitride glasses," *J. Eur. Ceram. Soc.*, vol. 24, no. 12, pp. 3377–3385, 2004.

[130] A. E. B. Presland, G. L. Price, and D. L. Trimm, "Hillock formation by surface diffusion on thin silver films," *Surf. Sci.*, vol. 29, no. 2, pp. 424–434, 1972.

[131] E. O. Filatova and A. S. Konashuk, "Interpretation of the Changing the Band Gap of Al2O3 Depending on Its Crystalline Form: Connection with Different Local Symmetries," *J. Phys. Chem. C*, vol. 119, no. 35, pp. 20755–20761, Sep. 2015.

[132] V. Rose and R. Franchy, "The band gap of ultrathin amorphous and well-ordered Al2 O3 films on CoAl(100) measured by scanning tunneling spectroscopy," *J. Appl. Phys.*, vol. 105, no. 7, pp. 1–4, 2009.

[133] M. Chen *et al.*, "X-ray photoelectron spectroscopy and auger electron spectroscopy studies of Al-doped ZnO films," *Appl. Surf. Sci.*, vol. 158, no. 1, pp. 134–140, 2000.

[134] J. F. Moulder, W. F. Stickle, P. E. Sobol, and K. D. Bomben, "Handbook of X-ray Photoelectron Spectroscopy," p. 261, 1992.

[135] M. Bou, J. M. Martin, T. Le Mogne, and L. Vovelle, "Chemistry of the interface between aluminium and polyethyleneterephthalate by XPS," *Appl. Surf. Sci.*, vol. 47, no. 2, pp. 149–161, 1991.

[136] S. A. Flodstrom, R. Z. Bachrach, R. S. Bauer, J. C. McMenamin, and S. B. M. Hagström, "Investigation of plasmon sidebands by synchrotron radiation tuning of electron escape depths," *J. Vac. Sci. Technol.*, vol. 14, no. 1, pp. 303–306, 1977.

[137] L. Ley, F. McFeely, S. Kowalczyk, J. Jenkin, and D. Shirley, "Many-body effects in x-ray photoemission from magnesium," *Phys. Rev. B*, vol. 11, no. 2, p. 600, 1975.

[138] K. Domen and T. J. Chuang, "Laser induced photodissociation and desorption. I. CH2I2 adsorbed on Al2O3," *J. Chem. Phys.*, vol. 90, no. 6, pp. 3318–3331, 1989.

[139] A. F. Carley and M. W. Roberts, "An X-ray Photoelectron Spectroscopic Study of the Interaction of Oxygen and Nitric Oxide with Aluminum," *Proc. R. Soc. A*, vol. 363, pp. 403–424, 1978.

[140] P. M. Th., M. Van Attekum, and J. M. Trooster, "Bulk- and surface-plasmon-loss intensities in photoelectron, Auger, and electron-energy-loss spectra of Al metal," *Phys. Rev. B*, vol. 18, no. 8, pp. 3872–3883, 1978.

[141] R. Koirala, K. R. Gunugunuri, S. E. Pratsinis, and P. G. Smirniotis, "Effect of zirconia doping on the structure and stability of CaO-based sorbents for CO2 capture during extended operating cycles," *J. Phys. Chem. C*, vol. 115, no. 50, pp. 24804–24812, 2011.

[142] H. Van Doveren and J. A. T. H. Verhoeven, "XPS spectra of Ca, Sr, Ba and their oxides," *J. Electron Spectros. Relat. Phenomena*, vol. 21, no. 3, pp. 265–273, 1980.

[143] P. H. Bolt and E. Grotenhuis, "The interaction of thin NiOjayers with single crystalline a-Al , O ,(1120) substrates," vol. 329, pp. 227–240, 1995.

[144] F. Rueda *et al.*, "Characterization of Venezuelan laterites by X-ray photoelectron spectroscopy," *J. Electron Spectros. Relat. Phenomena*, vol. 82, no. 3, pp. 135–143, 1996.

[145] B. J. Tan, K. J. Klabunde, and P. M. a Sherwood, "XPS studies of solvated metal atom dispersed catalysts. Evidence for layered cobalt-manganese particles on alumina and silica," *J. Am. Chem. Soc.*, vol. 113, no. 3, pp. 855–861, 1991.

[146] B. Ealet, M. H. Elyakhloufi, E. Gillet, and M. Ricci, "Electronic and crystallographic structure of γ-alumina thin films," *Thin Solid Films*, vol. 250, no. 1–2, pp. 92–100, 1994.

[147] D. F. Mitchell, K. B. Clark, J. A. Bardwell, W. N. Lennard, G. R. Massoumi, and I. V Mitchell, "Film Thickness Measurements of SiO2 by XPS," *Surf. Interface Anal.*, vol. 21, no. August 1993, pp. 44–50, 1994.

[148] A. A. Galuska, J. C. Uht, and N. Marquez, "Reactive and nonreactive ion mixing of Ti films on carbon substrates," *J. Vac. Sci. Technol. A Vacuum, Surfaces, Film.*, vol. 6, no. 1, p. 110, 1988.

[149] T. Gross, M. Ramm, H. Sonntag, W. Unger, H. M. Weijers, and E. H. Adem, "An XPS analysis of different SiO2 modifications employing a C 1s as well as an Au 4f7/2 static charge reference," *Surf. Interface Anal.*, vol. 18, no. 1, pp. 59–64, 1992.

[150] T. A. Clarke and E. N. Rizkalla, "X-ray photoelectron spectroscopy of some silicates," *Chem. Phys. Lett.*, vol. 37, no. 3, pp. 523–526, 1976.

[151] H. Seyama and M. Soma, "X-ray photoelectron spectroscopic study of montmorillonite containing exchangeable divalent cations," *J. Chem. Soc. Faraday Trans. 1*, vol. 80, no. 1, p. 237, 1984.

[152] S. Bahadur, D. Gong, and J. Anderegg, "Investigation of the influence of CaS, CaO and CaF2 fillers on the transfer and wear of nylon by microscopy and XPS analysis," *Wear*, vol. 197, pp. 271–279, 1996.

[153] Y. Inoue and I. Yasumori, "Catalysis by alkaline earth metal oxides. III. X-ray photoelectron spectroscopic study of catalytically active MgO, CaO, and BaO surfaces.," *Bulletin of the Chemical Society of Japan*, vol. 54. pp. 1505–1510, 1981.

[154] A. Barrie and F. J. Street, "An Auger and X-ray photoelectron spectroscopic study of sodium metal and sodium oxide," *J. Electron Spectros. Relat. Phenomena*, vol. 7, no. 1, pp. 1–31, 1975.

[155] B. R. Strohmeier and D. M. Hercules, "Surface spectroscopic characterization of manganese/aluminum oxide catalysts," *J. Phys. Chem.*, vol. 88, no. 21, pp. 4922–4929, 1984.

[156] L. E. Basini, A. Guarinoni, and L. C. Carluccio, "Catalytic system for catalytic

partial oxidation processes with a short contact time," WO2011151082, 08-Dec-2011.

[157] A. Souto, F. Guitian, and S. Aza, "Purification of Mullite by Reduction and Volatilization of Impurities," *J. Am. Ceram. Soc.*, vol. 82, no. 10, pp. 2660–2664, Dec. 2004.

[158] T. B. Reed, *Free Energy of Formation of Binary Compounds: An Atlas of Charts for High-temperature Chemical Calculations*. Biomass Energy Foundation Press, 2000.

[159] M. C. Morris, H. F. McMurdie, Ew. H. Evans, B. Paretzkin, H. S. Parker, and N. C. Panagiotopoulos, *Standard X-ray diffraction powder patterns*. 1981.

[160] H. A. Wriedt, "The AI-O (Aluminum-Oxygen) System," *Bull. Alloy Phase Diagrams*, vol. 6, no. 6, pp. 548–553, 1985.

[161] H. Hirata and K. Hoshikawa, "Oxygen solubility and its temperature dependence in a silicon melt in equilibrium with solid silica," *J. Cryst. Growth*, vol. 106, no. 4, pp. 657–664, Dec. 1990.

[162] M. Stöger-Pollach, T. Walter, M. Muske, S. Gall, and P. Schattschneider, "Phase transformations of an alumina membrane and its influence on silicon nucleation during the aluminium induced layer exchange," *Thin Solid Films*, vol. 515, no. 7–8, pp. 3740–3744, 2007.

[163] J. Schneider *et al.*, "A simple model explaining the preferential (1 0 0) orientation of silicon thin films made by aluminum-induced layer exchange," vol. 287, pp. 423–427, 2006.

[164] J. Schneider *et al.*, "Aluminum-induced crystallization: Nucleation and growth process," *J. Non. Cryst. Solids*, vol. 352, no. 9–20 SPEC. ISS., pp. 972–975, 2006.

[165] J. Klein, J. Schneider, M. Muske, S. Gall, and W. Fuhs, "Aluminium-induced crystallisation of amorphous silicon : influence of the aluminium layer on the process," vol. 452, pp. 481–484, 2004.

[166] J. Schneider, J. Klein, M. Muske, S. Gall, and W. Fuhs, "Aluminum-induced crystallization of amorphous silicon : preparation effect on growth kinetics," vol. 340, pp. 127–130, 2004.

[167] O. Nast, S. Brehme, S. Pritchard, A. G. Aberle, and S. R. Wenham, "Aluminium-induced crystallisation of silicon on glass for thin-film solar cells," vol. 65, pp. 385–392, 2001.

[168] S. Gall, M. Muske, I. Sieber, O. Nast, and W. Fuhs, "Aluminum-induced crystallization of amorphous silicon," vol. 302, pp. 741–745, 2002.

[169] A. Mohiddon and G. Krishna, "Metal Induced Crystallization," in *Crystallization - Science and Technology*, Marcello Rubens Barsi Andreeta, Ed. 2012, pp. 461–480.

[170] W. Cui, C. Wang, J. Yan, Z. Wang, and D. Wei, "Ultrasonics Sonochemistry Wetting and reaction promoted by ultrasound between sapphire and liquid Al – 12Si alloy," *Ultrason. - Sonochemistry*, vol. 20, no. 1, pp. 196–201, 2013.

[171] T. Huang *et al.*, "Aluminum induced crystallization of strongly (111) oriented polycrystalline silicon thin film and nucleation analysis," *Sci. China Technol. Sci.*, vol. 53, no. 11, pp. 3002–3005, 2010.

[172] J. L. Murray and A. J. McAlister, "The AI-Si (Aluminum-Silicon) System," *Bull. Alloy Phase Diagrams*, vol. 5, no. 1, pp. 74–84, 1984.

[173] S. C. Flood and J. D. Hunt, "Modification of Al-Si eutectic alloys with Na," *Met. Sci.*, vol. 15, no. 7, pp. 287–294, 1981.

[174] S. Shankar, Y. W. Riddle, and M. M. Makhlouf, "Nucleation mechanism of the eutectic phases in aluminum-silicon hypoeutectic alloys," *Acta Mater.*, vol. 52, no. 15, pp. 4447–4460, 2004.

[175] S. Hegde and K. N. Prabhu, "Modification of eutectic silicon in Al-Si alloys," *J. Mater. Sci.*, vol. 43, no. 9, pp. 3009–3027, 2008.

[176] A. K. Dahle, K. Nogita, S. D. McDonald, C. Dinnis, and L. Lu, "Eutectic modification and microstructure development in Al-Si Alloys," *Mater. Sci. Eng. A*, vol. 413–414, pp. 243–248, 2005.

[177] W. Burger and M. J. Burge, "The Discrete Fourier Transform in 2D," in *Digital Image Processing: An Algorithmic Introduction using Java*, 1st ed., London: Springer London, 2008, pp. 343–366.

[178] C. Beneking *et al.*, "Recent developments of silicon thin film solar cells on glass substrates," *Thin Solid Films*, vol. 351, no. 1–2, pp. 241–246, 1999.

APPENDIX A

PUBLICATIONS OF THE AUTHOR

Patent

TP15-284 – Cam Yüzeyi Desenlemesi için Bir Solüsyon ve Uygulaması (A Solution for Glass Texturing and Its Application), **2016**

Peer-Reviewed Publications

1. **Ünal M.**, Tankut A., Turan R. "A New Solution to Use in Aluminum Induced Texturing Process for High Performance Scattering Interfaces". In writing. *Manuscript in preparation*.
2. **Ünal M.**, Tankut A., Canlı S., and Turan R. (2017). "Near-unity Haze by Aluminum Induced Glass Texturing: Structural Evolution of Al/Glass Interface and Its Impact on Texturing" Optical Materials Express. 7(4). **Accepted,** *In press*.
3. **Ünal M.**, Tankut A., Yıldız İ., Sökmen İ., and Turan R. (2017). "An XPS Study on the Surface Chemistry of Al/glass Interface during Aluminum Induced Texturing Process". Thin Solid Films. **Accepted**, *In press*.

4. **Ünal M.**, Demircioğlu Z., Dönerçark E., Özkol E., and Turan R. (2017). "Aluminum Induced Texturing of Sandy and Prism Glasses: Combination of Micro/Nano Texture with Macro Texture". Physica Status Solidi A: Applications and Materials Science, 1600856. *DOI: 10.1002/pssa.201600856*

5. **Ünal M.**, Tankut A., Sökmen İ., Çolakoğlu T., and Turan R. (2016). "Evolution of Al/Al2O3 Layer on Glass Substrates during N2 Anneal". Energy Procedia, 102C. pp. 3-10. *DOI: 10.1016/j.egypro.2016.11.311*

6. **Ünal M.**, Nasser H., Günöven M., Sökmen İ., Tankut A., and Turan R. (2015). "Effect of Aluminum Thickness and Etching Time of Aluminum Induced Texturing Process on Soda Lime Glass Substrates for Thin Solar Cell Applications". *Pysica Status Solidi C,* 12 (9-11). pp. 1201-1205. *DOI: 10.1002/pssc.201510125*

Conference Proceeding

1. **Ünal M.**, Nasser H., Günöven M., Tankut A., Sökmen İ., and Turan R. (2015). "Aluminum Induced Glass Texturing (AIT) on Soda-Lime, Borosilicate, Alkali-Free and Silica Glass for Thin Film Solar Cell Applications". *31st European Photovoltaic Solar Energy Conference and Exhibition.* pp. 230-234. *DOI: 10.4229/EUPVSEC20152015-1BV.7.33*

2. **Ünal M.**, Nasser H., Sökmen İ., and Turan R. (2015). "Soda-Kireç Cam Altlıkların İnce Film Güneş Gözeleri için Alüminyum ile Desenlendirilmesi". Teknik Bülten 29th Şişecam Glass Symposium Special Issue. 44(1). pp. 39-43.